Effective Potentials for Numerical Investigations of Complex Intermetallic Phases

Effektive Potenziale zur numerischen Untersuchung komplexer intermetallischer Phasen

Von der Fakultät für Mathematik und Physik der Universität Stuttgart zur Erlangung der Würde eines Doktors der Naturwissenschaften (Dr. rer. nat.) genehmigte Abhandlung

Vorgelegt von

Daniel Schopf

aus Stuttgart

Hauptberichter: Prof. Dr. Hans-Rainer Trebin
Mitberichter: Prof. Dr. Christian Holm

Tag der mündlichen Prüfung: 27. März 2013

Institut für Theoretische und Angewandte Physik
Universität Stuttgart

2013

Meinen Eltern

Contents

List of Abbreviations

ADP	Angular-Dependent Potential, page 86
CMA	Complex Metallic Alloy, page 30
DE	Differential Evolution, page 103
EAM	Embedded Atom Method, page 85
GGA	Generalized-Gradient Approximation, page 62
HCACF	Heat Current Autocorrelation Function, page 142
LBPP	Large Bicapped Pentagonal Prism, page 156
LDA	Local Density Approximation, page 62
MD	Molecular Dynamics, page 73
NC-PP	Norm-Conserving Pseudopotentials, page 66
NEMD	Non-Equilibrium Molecular Dynamics, page 134
PAW	Projector Augmented Waves, page 67
PBC	Periodic Boundary Conditions, page 82
PBE	Perdew, Burke and Ernzerhof functional, page 63
PDOS	Phonon Density Of States, page 129
PGEC	Phonon Glass – Electron Crystal, page 43
PMI	Pseudo-Mackay Icosahedron, page 155
QMD	Quantum Molecular Dynamics, page 71
US-PP	Ultrasoft Pseudopotentials, page 67
VACF	Velocity Autocorrelation Function, page 130

List of Figures

List of Tables

Abstract

The class of Complex Metallic Alloys (CMAs) is interesting for its wide range of physical properties. There are materials that exhibit high hardness at low density or good corrosion resistance, which is important for technological applications. Other compounds are superconductors, have strong anisotropic transport coefficients or exhibit a novel magnetic memory effect. The theoretical investigation of CMAs is often very challenging because of their inherent complexity and large unit cells with up to several thousand atoms. Molecular dynamics simulations with classical interaction potentials are well suited for this task – they can handle hundreds of thousands of atoms in reasonable time. Such simulations can provide insight into static and dynamic processes at finite temperatures on an atomistic level.

The accuracy of these simulations depends strongly on the quality of the employed interaction potentials. To generate physically relevant potentials the force-matching method can be applied. A computer code called *potfit* has been developed at the Institute for Theoretical and Applied Physics (ITAP) especially for this task. It uses a large database of quantum-mechanically calculated reference data, forces on individual atoms and cohesive energies, to generate effective potentials. The parameters of the potential are optimized in such a way that the reference data are reproduced as accurately as possible.

The *potfit* program has been greatly enhanced as part of this thesis. The optimization of analytic potentials, new potential models as well as a new optimization algorithm were implemented. Potentials for two different complex metallic alloy systems have been generated and used to study their properties with molecular dynamics simulations.

The first system is an approximant to the decagonal Al-Pd-Mn quasicrystal. A potential which can reproduce the cohesive energy with high accuracy was generated. With the help of this potential a refinement of the experimentally poorly determined structure model could be performed.

The second class of potentials was fitted for intermetallic clathrate systems. They have interesting thermoelectric properties which originate from their special structure. Silicon- and germanium-based clathrate potentials were derived and the influence of the complex structure on the thermal conductivity has been studied.

Effektive Potenziale zur numerischen Untersuchung komplexer intermetallischer Phasen

Zusammenfassung in deutscher Sprache

Einleitung

Mit der Entwicklung der Mikrochips in den 1950er Jahren und der Einführung von Hochleistungsrechnern wurde die Simulation als weitere tragende Säule in der physikalischen Forschung etabliert. Obwohl dieses Feld deutlich jünger ist als die bereits bestehenden, Experimental- und theoretische Physik, wurden hier in den letzten Jahrzehnten wertvolle Beiträge geleistet. Viele Entdeckungen in den verschiedenen Teilgebieten waren nur mit der Hilfe von Computersimulationen möglich. Vor allem in der statistischen Physik und der Quantenmechanik kann die Simulation als Verbindung zwischen Theorie und Experiment angesehen werden. Die äußerst komplexen theoretischen Modelle können häufig nur durch numerische Verfahren berechnet werden. Dies ermöglicht anschließend einen Vergleich mit experimentell verfügbaren Daten. Simulationen können dabei neue Modelle testen oder bei der Interpretation neuer experimenteller Daten helfen.

Die Anwendungsgebiete von Computersimulationen sind dabei praktisch unbegrenzt. Die Skala reicht von Simulationen auf (sub)atomarer Ebene, über makroskopische Systeme bis hin zum gesamten Universum. Obwohl diese Systeme erhebliche Unterschiede aufweisen, ist die numerische Herangehensweise doch

recht ähnlich. Das zugrundeliegende physikalische Modell muss jeweils an die deterministische Natur des Computers angepasst werden. Dazu werden üblicherweise die physikalischen Dimensionen wie Raum und Zeit diskretisiert. Anschließend werden die physikalisch relevanten Gleichungen durch numerische Verfahren gelöst.

Das Thema dieser Arbeit sind atomistische Computersimulationen. Sie finden in verschiedenen Forschungsrichtungen Anwendung, z.B. in den Materialwissenschaften, der Chemie und auch der Physik.

Hauptsächlich werden drei verschiedene Arten von Simulationen verwendet. Die präziseste Methode basiert auf der Dichtefunktionaltheorie und berücksichtigt sowohl die Elektronen als auch die Atomkerne auf quantenmechanischer Ebene. Diese sehr aufwändigen Rechnungen können allerdings nur für kleine Systeme und kurze Simulationszeiten durchgeführt werden.

Eine Näherung wird verwendet, um die Simulationen auch für größere Systeme durchführen zu können. Die *Tight-Binding*-Methode benutzt Einteilchen-Wellenfunktionen freier Atome, ähnlich der LCAO Methode. Dadurch wird sowohl der Rechenaufwand, aber auch die Genauigkeit der Simulation deutlich reduziert.

Die älteste Simulationsmethode ist die Molekulardynamik (MD). Dabei werden die Atome als Punktmassen idealisiert, die durch ein effektives Potenzial miteinander wechselwirken. Mit dieser Vereinfachung können deutlich mehr Atome als mit den vorhergehenden Methoden simuliert werden. Auf handelsüblichen Computern sind so Simulationen mit mehreren Millionen Atomen in vertretbarer Zeit möglich. Die Genauigkeit der Ergebnisse hängt dabei stark von den verwendeten Potenzialen ab.

Mit MD Simulationen ist es möglich, neue Materialien zu untersuchen, die aufgrund ihrer Komplexität für quantenmechanische Rechnungen nicht zugänglich sind. Ein Beispiel dafür sind Quasikristalle, deren Kristallgitter aperiodisch ist, was zu einer unendlich großen Einheitszelle führt. Aber auch einige periodische Strukturen können einen hohen Grad an Komplexität aufweisen. In der Klasse der *komplexen metallischen Phasen* gibt es Strukturen mit mehreren tausend Atomen in einer Einheitszelle. Um diese oftmals stark ungeordneten Phasen zu untersuchen können MD Simulationen eingesetzt werden.

Für physikalisch korrekte MD Simulationen werden präzise Potenziale benötigt. Diese werden üblicherweise an einige experimentelle oder quantenmechanische Daten angepasst. Für komplexe Systeme ist dies aber oft nicht möglich, da keine Daten vorliegen und auch nicht ohne Weiteres berechnet werden können.

In einem Teil dieser Arbeit geht es um die Erzeugung physikalisch fundierter

Potenziale für komplexe metallische Verbindungen. Dazu wird die Force-Matching-Methode verwendet. Diese setzt nicht auf spezielle, experimentell oder quantenmechanisch bestimmte Größen. Statt dessen wird eine Vielzahl von quantenmechanisch berechneten Kräften auf einzelne Atome benutzt, um ein effektives Potenzial anzupassen. Durch die geeignete Wahl dieser Referenzdaten können effektive Potenziale für komplexe Verbindungen mit mehreren Elementen entwickelt werden.

Das bereits vorhandene Programm *potfit* wurde dazu deutlich erweitert. Es wurden eine neue Potenzialform, ein neues Potenzialmodell sowie ein neues Optimierungsverfahren implementiert. In dieser Arbeit werden die Vorgehensweise zur Erstellung eines Potenzials erläutert und auch einige Anwendungen vorgestellt.

Die in englisch verfasste Arbeit ist in drei Teile gegliedert. Im ersten Teil geht es um die theoretischen Grundlagen. Dabei werden die Strukturen der komplexen Verbindungen als auch deren Eigenschaften, wie z.B. die Thermoelektrizität, erläutert. Der zweite Teil beschäftigt sich mit den verwendeten numerischen Methoden. Es werden die Grundlagen der quantenmechanischen Simulationen dargelegt, die Molekulardynamik mit effektiven Potenzialen vorgestellt sowie die Force-Matching-Methode und deren Implementierung geschildert. Im letzten Teil werden die Ergebnisse, die mit den Potenzialen berechnet wurden, vorgestellt.

Theoretische Grundlagen

Komplexe metallische Phasen

Die Klasse der komplexen metallischen Phasen ist bereits seit Beginn des 20. Jahrhunderts bekannt. Trotzdem sind für viele physikalische Eigenschaften dieser Verbindungen nur wenige Daten veröffentlicht. Das liegt zum einen an der Schwierigkeit, Einkristalle in ausreichender Größe zu züchten. Zum anderen aber waren auch die theoretischen Modelle und Methoden nicht ohne Weiteres für diese Systeme anwendbar.

Komplexe metallische Phasen zeichnen sich durch drei charakteristische Eigenschaften aus. Sie haben eine große Einheitszelle mit hunderten oder tausenden von Atomen; diese hat eine clusterbasierte Unterstruktur und enthält einen gewissen Grad an Unordnung. Vor allem durch die Clusterstruktur und die Unordnung ergeben sich neue physikalische Phänomene etwa zur Plastizität (Metaversetzungen) oder Ordnung-Unordnungs-Phasenübergänge.

Eine spezielle Form der komplexen Phasen bilden die Quasikristalle. Deren Kris-

tallstruktur ist aperiodisch, was zu einer unendlich großen Einheitszelle führt. Viele CMA Strukturen können als rationale Approximanten eines Quasikristalls angesehen werden. Sie besitzen lokal eine ähnliche atomare Struktur, die sich jedoch periodisch wiederholt. Für Approximanten können die etablierten Simulationsmethoden ohne große Anpassungen angewandt werden.

Für technologische Anwendungen sind Klathrate momentan von besonderem Interesse. Dabei geht es vor allem um die Verwendung als Thermoelektrika, welche aus Abwärme elektrische Energie gewinnen können. Die Klathratstruktur wurde dabei zuerst bei Wassermolekülen unter hohem Druck gesehen, inzwischen jedoch auch bei den Halbleiterelementen Silizium, Germanium und Zinn. Es gibt verschiedene Varianten dieser Struktur, die jedoch alle nach dem gleichen Prinzip aufgebaut sind. Die Halbleiterelemente bilden zwei oder drei Arten von Käfigen, z.B. Dodekaeder und Tetrakaidekaeder für eine Typ I Struktur. Diese Käfige werden dann raumfüllend angeordnet und bilden das Gerüst der Klathrate. Außerdem besteht die Möglichkeit, ein weiteres Atom im Inneren eines jeden Käfigs zu platzieren oder einzelne Gerüstatome durch Fremdatome zu ersetzen. Dadurch ergeben sich vielfältige Möglichkeiten, die physikalischen Eigenschaften von Klathraten gezielt zu verändern.

Thermoelektrika

Sowohl in der Industrie als auch in privaten Haushalten entsteht bei vielen Prozessen Abwärme, die nicht genutzt wird. Oft liegt die Effizienz von Maschinen und Anlagen deutlich unter $50\,\%$. Durch Rückgewinnung von Energie aus Abwärme könnte der Nettoenergieverbrauch in vielen Bereichen deutlich reduziert werden. Mit Thermoelektrika ist es möglich, thermische Energie in elektrische Energie umzuwandeln. Momentan liegt der Wirkungsgrad dieser Materialien bei etwa $10\,\%$, eine Verbesserung ist Gegenstand vieler aktueller Forschungen.

Die historische Entwicklung ist in drei unterschiedlichen Zeitabschnitten erfolgt. Zwischen 1820 und 1850 wurden die grundlegenden Effekte entdeckt und makroskopisch erklärt. Nach der Entwicklung der Thermodynamik und statistischen Physik wurden in der Zeit von 1955 bis 1970 die meisten der bis heute verwendeten Materialien identifiziert. Bis zum Jahre 1995 gab es keine nennenswerte Fortschritte, erst mit dem Konzept des Phononenglas-Elektronenkristalls wurde die Forschung wieder intensiviert.

Die Effizienz eines Materials wird über die Figure of Merit definiert. Sie ist proportional zur elektrischen Leitfähigkeit und antiproportional zur thermischen Leitfähigkeit. Je größer diese Zahl ist, desto mehr Energie kann umgewandelt

werden. Für eine möglichst große Figure of Merit sollte ein Material also eine hohe elektrische und eine niedrige thermische Leitfähigkeit aufweisen. Das wird durch das Konzept des Phononenglas-Elektronenkristalls beschrieben. Für Phononen, die Träger des Wärmestroms, sollte das Material sich wie ein Glas verhalten, für die Elektronen jedoch wie ein herkömmlicher Kristall.

Algorithmen und numerische Methoden

Computersimulationen haben in der Forschung und auch in der Industrie in den letzten Jahrzehnten eine bedeutende Rolle eingenommen. Durch die immer weiter wachsende Leistungsfähigkeit moderner Supercomputer können viele Messungen und Experimente schon vorab simuliert werden, was Kosten sparen und mögliche Fehlerquellen bereits frühzeitig aufdecken kann. Ein wesentlicher Teil dieser Arbeit basiert auf atomistischen Simulationen von Festkörpern. Dabei werden zwei verschiedene Methoden eingesetzt, die quantenmechanische *Ab-initio*-Simulation und die klassische Molekulardynamik.

Ab-initio-Simulationen

Die grundlegende Idee der *Ab-initio*-Simulationen ist es, das quantenmechanische Vielteilchenproblem numerisch zu lösen. Aufgrund der unglaublichen Komplexität ist dies aber nur im Rahmen gewisser Näherungen möglich. Die dabei wichtigste ist die Dichtefunktionaltheorie; sie erlaubt es, das Problem auf die Berechnung einer Elektronendichte umzuformulieren. Mit dem Hohenberg-Kohn Theorem ist es anschließend möglich, alle physikalischen Eigenschaften eines Systems zu bestimmen.

In der Praxis werden die Kohn-Sham Gleichungen selbstkonsistent gelöst, wobei insbesondere das Austausch-Korrelationsfunktional Probleme bereitet. Mit Hilfe verschiedener Näherungen sowie der Verwendung von Pseudopotenzialen kann aber auch hier der benötigte Rechenaufwand reduziert werden.

Mit *Ab-initio*-Methoden lassen sich heutzutage Simulationen von periodischen Systemen mit wenigen hundert Atomen durchführen. Auch dynamische Phänomene können auf kleinen Zeitskalen untersucht werden.

Molekulardynamik

Eine weitere Methode für Partikelsimulationen ist die Molekulardynamik. Um Rechenzeit zu sparen, wird hier eine sehr drastische Näherung verwendet. Die Elektronen werden nicht berücksichtigt und die Atome als Punktmassen angenommen, die durch ein effektives Potenzial miteinander wechselwirken. Dadurch wird die Präzision dieser Simulationen reduziert, die Anzahl der zu simulierenden Atome jedoch erheblich vergrößert. Auf einem Desktopcomputer können dadurch Systeme mit mehreren Millionen Teilchen simuliert werden.

Die entscheidende Komponente für die Genauigkeit molekulardynamischer Simulationen sind die effektiven Potenziale. Können diese die Wechselwirkungen zwischen den Atomen mit hinreichender Genauigkeit wiedergeben, sind die Resultate oft nur wenig schlechter als *Ab-initio*-Simulationen. Während früher, aufgrund mangelnder Rechenleistung, oft modellhafte Potenziale verwendet wurden, werden heutzutage die Potenziale an experimentelle oder quantenmechanisch berechnete Referenzdaten angepasst. Dabei werden sowohl Mehrkörperterme als auch richtungsabhängige Wechselwirkungen erzeugt, die für die korrekte Beschreibung vieler Festkörper benötigt werden.

Force-matching mit *potfit*

Um physikalisch möglichst präzise effektive Potenziale zu erzeugen, kann die Force-Matching-Methode angewandt werden. Dabei werden die Parameter eines Potenzials so optimiert, dass quantenmechanisch berechnete Referenzdaten möglichst genau reproduziert werden können. In der Regel werden dazu die Kräfte auf einzelne Atome, die kohäsive Energie sowie der Spannungstensor einer Struktur benutzt, es können jedoch noch weitere physikalische Größen hinzugefügt werden. Die Implementierung im Computerprogramm *potfit* umfasst drei verschiedene Optimierungsalgorithmen, die sowohl tabellierte als auch analytische Potenziale anpassen können.

Mit der Force-Matching-Methode können Potenziale für verschiedene Einsatzzwecke erzeugt werden. Sowohl durch die Wahl der verwendeten Referenzdaten als auch durch die Gewichtung der einzelnen Daten ist es möglich, die Potenziale zu spezialisieren. Dabei sollte auf jeden Fall darauf geachtet werden, dass die resultierenden Potenziale nur begrenzt transferierbar sind.

Für diese Arbeit wurden ausschließlich analytische Potenziale erzeugt. Die dazu nötigen funktionalen Formen, als auch die Anpassungen im Programm *potfit* werden ausführlich geschildert. Ein für die Erzeugung von Potenzialen äußerst

wichtiger Punkt, die Validierung, wird detailliert erläutert.

Weitere Methoden & Programme

Zur Berechnung einiger physikalischer Eigenschaften ist der Einsatz von Zusatzsoftware erforderlich. Dies ist insbesondere der Fall, wenn die Berechnung entweder Informationen von verschiedenen Zeitschritten oder von mehreren Simulationen benötigt. In dieser Arbeit ist das die Berechnung der thermischen Leitfähigkeit sowie der phononischen Zustandsdichte und der Dispersionskurven.

Außerdem werden die grundlegend verschiedenen Methoden zur Bestimmung der thermischen Leitfähigkeit diskutiert und verglichen.

Simulationen und Ergebnisse

Al-Pd-Mn

Das ternäre Al-Pd-Mn System bildet viele komplexe Strukturen, wovon einige eine neue Art der Plastizität zeigen. In den Approximanten eines dekagonalen Quasikristalls, den ε-Phasen, wurde eine Metaversetzung beobachtet, deren innere Struktur experimentell jedoch nur sehr ungenau bestimmt werden konnte. Zur numerischen Beschreibung dieser Versetzung können aufgrund der Systemgröße keine quantenmechanischen Rechnungen verwendet werden. Mit Molekulardynamik hingegen können sowohl die Struktur optimiert werden als auch deren Dynamik untersucht werden.

Für die Referenzdaten zur Erzeugung eines effektiven Potenzials wurden verwandte binäre Strukturen als auch theoretische Modellstrukturen verwendet. Um die Tauglichkeit verschiedener analytischer Potenzialmodelle zu testen wurden drei Potenziale angepasst, jeweils mit unterschiedlichen Funktionen. Dabei stellte sich heraus, dass für EAM-Potenziale Oszillationen sowohl in der Paar- als auch der Transferfunktion zu den besten Ergebnissen führen.

Die drei Potenzialmodelle wurden sowohl auf statische als auch dynamische Eigenschaften hin untersucht. Die Abweichungen der Energie lagen dabei jeweils im Bereich weniger meV/Atom, der für die thermodynamische Stabilität ausschlaggebende Abstand zur konvexen Hülle konnte jedoch nur von Modell III korrekt wiedergegeben werden. Auch in den dynamischen Simulationen, der Bestimmung der Schmelztemperatur sowie der elastischen Konstanten waren die Ergebnisse mit diesem Potenzial am genauesten.

Klathrate

Die Anwendung von Klathraten als Thermoelektrika ist seit Ende des 20. Jahrhunderts bekannt. Durch die niedrige thermische Leitfähigkeit ergibt sich eine hohe Effizienz bei der Umwandlung von Wärme in eine Spannungsdifferenz. Die dazu am besten geeigneten Materialien sind oft binäre oder ternäre Verbindungen mit einem hohen Grad an Komplexität. Zur Untersuchung der thermischen Leitfähigkeit von verschiedenen intermetallischen Klathraten wurden effektive Potenziale erzeugt, die insbesondere die Gitterdynamik in diesen Systemen gut reproduzieren können.

Für die Wechselwirkung der Gerüstatome wurden richtungsabhängige Potenziale verwendet, um die gerichteten Bindungen in den tetraedrisch koordinierten Strukturen möglichst genau modellieren zu können. Die Referenzdaten zur Potenzialoptimierung wurden quantenmechanischen Simulationen von einfachen Klathraten entnommen. Der Schwerpunkt lag dabei auf den zwischenatomaren Kräften, die für die Gitterdynamik verantwortlich sind. Die Energien und Spannungen wurden ebenfalls berücksichtigt, allerdings nur mit einer geringen Gewichtung.

Die Potenzialerzeugung wurde in mehreren Stufen durchgeführt. Zuerst wurden die Potenziale für die leeren Klathrate ohne Gastatome angepasst. Anschließend wurden die binären Systeme zu den Referenzdaten hinzugefügt und die zusätzlich benötigten Potenziale gefittet. Zur Validierung der erzeugten Potenziale wurden sowohl die phononische Zustandsdichte als auch die Dispersionskurven berechnet. Für einfache Strukturen konnten diese Daten auch mit *Ab-initio*-Rechnungen verglichen werden. Bei komplexeren Strukturen war dies nicht immer möglich.

Die thermische Leitfähigkeit wurde sowohl für germanium- als auch siliziumbasierte Klathrate untersucht. Dabei wurden je drei Strukturen unterschiedlicher Komplexität verwendet. Die leeren Käfige besitzen die größte Leitfähigkeit. Durch die Gastatome, die in den Käfigen sitzen, werden Streuzentren für Phononen geschaffen, die Leitfähigkeit dieser Systeme ist deutlich reduziert. Werden zusätzlich noch einige der Gerüstatome durch Leerstellen ersetzt, kann die thermische Leitfähigkeit noch weiter verringert werden.

Zusammenfassung

Im Rahmen dieser Arbeit wurden effektive Potenziale für verschiedene komplexe metallische Phasen erstellt. Das dazu verwendete Programm *potfit* wurde dabei um einen Optimierungsalgorithmus und eine winkelabhängige Wechselwirkung

erweitert. Mit der eingesetzten Force-Matching-Methode können Potenziale für Materialien erstellt werden, die bisher in MD Simulationen nicht zugänglich waren.

Für das ternäre Al-Pd-Mn wurden Potenziale speziell für die Strukturoptimierung der ε-Phasen angepasst. Dabei wurde die Eignung verschiedener analytischer Funktionen im EAM Potenzialmodell untersucht. Für Oszillationen sowohl in der Paar- als auch Transferfunktion konnten die *Ab-initio*-Referenzwerte am genauesten reproduziert werden.

Zur Untersuchung der thermischen Leitfähigkeit in Klathraten wurden richtungsabhängige Potenziale für germanium- und silizium-basierte Systeme erzeugt. Die phononischen Zustandsdichten sowie die Phononendispersion konnten damit sehr gut wiedergegeben werden, was für den thermischen Transport von besonderer Bedeutung ist. Für beide Arten von Klathraten, Germanium und Silizium, wurden jeweils drei Strukturen mit steigender Komplexität erzeugt und deren thermische Leitfähigkeit mit der Green-Kubo-Methode simuliert. Dabei zeigte sich, dass mit steigender Komplexität die Leitfähigkeit reduziert wird.

Part I.

Theoretical background

Chapter 1:
Introduction

With the discovery of microchips in the 1950's and the following introduction of high performance computer systems the field of simulational physics was established. While it is considerably younger than the two traditional fields, theory and experiment, it has proven very valuable over the last decades. Many breakthroughs in different areas were only possible with the aid of computer simulations. Especially for statistical mechanics and quantum mechanics it can be regarded as a connection between theory and experiment. The complex theoretical models can be solved by numerical calculations and then be compared with experimental results. In this way a simulation can help test models or assist in the interpretation of new experimental results.

The aspects of computer simulations can be manifold. From simulations on an atomistic scale to macroscopic objects or even the whole universe, everything can be treated with the appropriate methods. While the systems are vastly different, the computational approaches are very similar. The underlying model has to be adapted to the deterministic nature of computers. Usually this is done by discretizing the physical dimensions like time and space. Afterwards the equations that govern the behavior of the system are solved with numerical methods.

The field that is concerned with in this work is atomistic computer simulations. They have a large scope of application in different research areas like materials science, chemical engineering as well as physics. Many different aspects of matter can be investigated, for example predicting properties of new materials or studying macroscopic processes on an atomistic scale.

There are three different methods which are currently used for atomistic simulations. The most accurate one is based on density functional theory. It accounts

for both electrons and nuclei and solves the quantum mechanical equations within some approximations. The accuracy of these so called *ab initio* methods, however, comes with a tradeoff. Only small systems with periodic boundary conditions can be simulated for short periods of time.

A simplified model is used for tight binding calculations. There single atom wave functions of free atoms are calculated, similar to the linear combination of atomic orbitals (LCAO) approach. When compared to *ab initio* calculations, tight binding is usually less accurate but considerably faster and can handle more atoms.

The most basic atomistic simulation method is classical molecular dynamics. The atoms are treated as point masses which interact through an effective potential according to Newton's laws. This simplification allows for the fast simulation of many billion atoms for several nanoseconds on state of the art supercomputers. Even on common desktop computers simulations of several hundred thousand atoms can be run in feasible time. The results of these calculations strongly depend on the quality of the interaction potentials.

With MD simulations it is possible to study new classes of materials, which have previously been inaccessible due to their inherent complexity. The best example for this are quasicrystals. Their crystal structure is aperiodic, i.e. the unit cell is infinitely large. But also for some periodic crystals the lattice structure can be complicated. Within the class of complex metallic alloys there are some structures that have several thousand atoms in their unit cell. To study these often highly disordered systems with computational methods, molecular dynamics simulations can be employed.

An important aspect of MD calculations is the model for the interactions. Commonly used effective potentials are fitted to experimental data or *ab initio* calculated parameters. For complex systems such data is often unavailable, the effective potentials used are mostly model potentials with no physical justification.

The main part of this work deals with the generation of accurate potentials for complex metallic alloys. This can be achieved with the force-matching method, which dramatically increases the amount of reference data used in the fitting process. The basic idea behind it is rather simple. Forces on individual atoms as well as energies and stresses of different atomic structures are calculated with *ab initio* methods. These values are then used as reference data for the potential fitting. The combination of the appropriate *ab initio* reference data makes it possible to fit potentials for complex systems containing more than a single chemical element.

The already existing implementation of the force-matching method in the *potfit* code has been greatly enhanced with new features and potential models. The

process of generating an effective potential is described and some applications for complex metallic alloys are discussed.

The thesis is divided into three parts. The first part introduces the theoretical basics. Complex metallic alloys are characterized and an overview of thermoelectric materials and their applications is given. The second part is about the algorithms and numerical methods used in this work. Density functional theory, molecular dynamics and force-matching are discussed in detail. In the last part the results obtained with the effective potentials are reported.

Part of this work has been previously published in other publications by the author, see *List of publications*, page 235.

Chapter 2:

Complex metallic alloys

The crystal structure of metals often is surprisingly simple. Most of them have either a face centered or body centered cubic unit cell containing only few atoms. Their arrangement has been determined at the beginning of the 20th century by X-ray diffraction. Because of their periodicity in real space they show a distinct diffraction pattern with sharp Bragg peaks. A typical experimental image from a diffraction experiment is shown in Fig. 2.1.

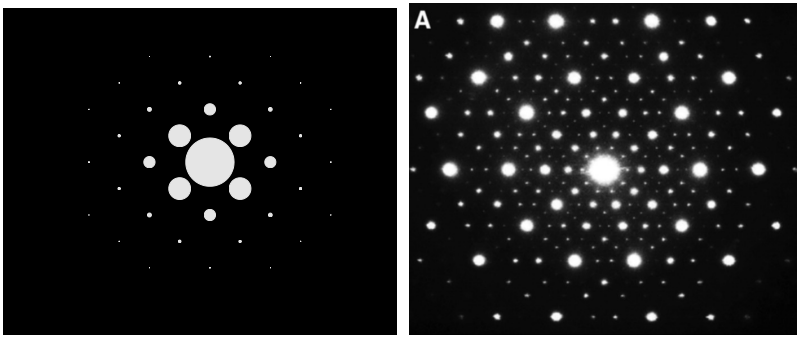

Figure 2.1: Two diffraction patterns of different crystal structures. Left: Simulated diffraction pattern of a bcc lattice. Right: Experimental diffraction pattern of a natural quasicrystal. From [16].

While this is also true for many intermetallic phases, there are some alloys which do not follow this rule. Maybe the most prominent one has been found by Pauling

[91]. In 1923 he discovered a $NaCd_2$ compound with so many Bragg peaks, that he was unable to determine all atomic positions. 30 years later it turned out that there were more than 1100 atoms sitting in a single unit cell.

This kind of complexity could not be handled by the methods available at that time. Nowadays experimental and theoretical studies have become feasible with the help of computers. A diffraction pattern with several thousand Bragg peaks can be resolved quickly with the help of powerful numerical algorithms. Atomistic simulations can provide new details on the structure and the dynamic behavior of complex phases.

In the following section some common properties of these complex metallic alloys will be discussed. The connection to quasicrystals is explained and clathrate systems are introduced. They are both special subclasses of complex metallic alloys which have been studied in detail for this work.

2.1 Properties

According to Urban and Feuerbacher [117], a complex metallic alloy can be characterized by the following three attributes:

1. They have a large unit cell.
2. The unit cell has a cluster substructure.
3. There is inherent disorder on the atomic scale.

Large unit cell The most remarkable fact of CMAs, when compared to other metallic alloys, is the number of atoms per unit cell. Common lattice types like body-centered cubic, hexagonal close packed and face-centered cubic have 2, 2 and 4 atoms per unit cell, respectively. The amount of disorder in these systems is thus very limited.

Over the last decades many different structures with several hundred atoms per unit cell have been discovered. In 2009 a complex metallic alloy with more than 23 000 atoms per unit cell has been reported by Weber *et al.* [120]. Due to the large number of atoms, different kinds of disorder can be found in these systems.

Some of these structures can be identified as rational approximants to quasicrystals, which have an infinitely large unit cell. They are discussed in Sec. 2.2.

Cluster substructure Understanding the crystal structure of CMAs on an atomic level is often very difficult. Fortunately the atoms are usually arranged in clusters, which in turn also arrange in regular patterns. Two of the most common cluster types are the Mackay [76] and the Bergman [14] cluster. They are built from basic polyhedra, like e.g. icosahedra or dodecahedra, which are packed into one another. The exact structure of both, Mackay and Bergman cluster, is shown in Fig. 2.2.

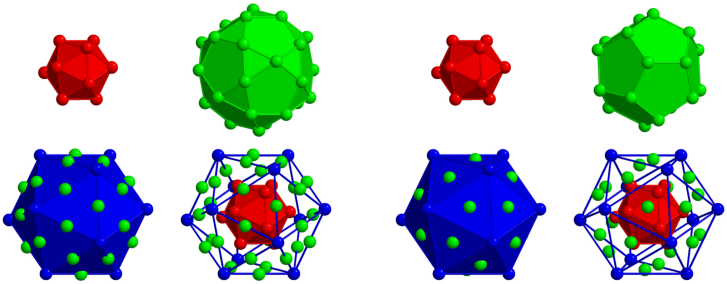

Figure 2.2: (a) The three innermost shells of a Mackay cluster: icosahedron (red), icosidodecahedron (green), icosahedron (blue) containing 55 atoms. (b) First three shells of the Bergman cluster: icosahedron (red), dodecahedron (green) icosahedron (blue) containing 45 atoms. From [36].

The size of these clusters can differ notably from the size of a unit cell. As a consequence interesting physical phenomena, like the metadislocations in the ε phases of Al-Pd-Mn [35], can be found in various CMAs.

Inherent disorder Due to the big unit cells and the large number of atoms, there can be disorder on different levels. The *configurational* disorder results from statistically varying orientations of the inner shell with respect to the outer shells. This type of disorder can also be created when the packing of the clusters is not perfectly compatible, e.g. when the size of an inner shell distorts the atomic positions of the outer shells. *Chemical* or *substitutional* disorder is created when different elements can occupy certain lattice sites. This phenomenon is called fractional occupancy. If there are geometrical constraints, *partial* site occupation can occur. The probability to find an atom at that particular lattice site is smaller than 1 to prevent additional defects. Finally *split* occupation can be found, which describes the case of two nearby lattice sites of which only one can be occupied at a time.

2.2 Quasicrystals

A very special subtype of complex metallic alloys are quasicrystals. They were discovered in 1984 by Shechtman *et al.* [104]. In an X-ray diffraction pattern of an Al-Mn alloy they observed fivefold symmetry, which is forbidden in periodic crystals. The sharp Bragg peaks, however, indicated long-range order. It became clear that this alloy had an icosahedral symmetry, incompatible with translational periodic order. Something similar was already know from mathematics, where Penrose [93] had discovered quasiperiodic tilings of the two-dimensional space. Those also show long-range nonperiodic translational and orientational order with a rotational symmetry incompatible with periodic translational order.

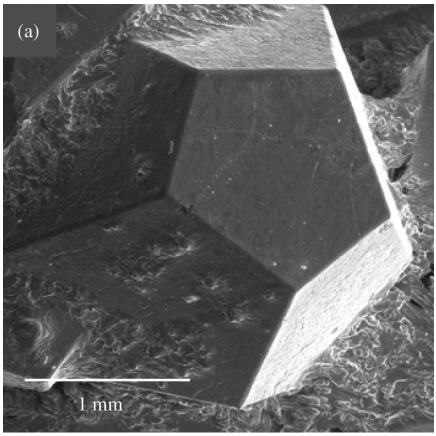

Figure 2.3: Scanning electron microscopy (SEM) micrograph showing an as-grown single-grain *i*-Al-Pd-Re quasicrystal. The icosahedral symmetry can be seen on a macroscopic scale. From [103].

The term *quasicrystal* was created by Levine and Steinhardt [75] to account for the quasiperiodic translational order in these systems. In the last decades not only icosahedral quasicrystals have been found, also octagonal, decagonal and dodecagonal quasicrystals were reported. They are periodic in one direction and aperiodic with eight-, ten- or twelve-fold symmetry in the plane perpendicular to it. An experimental image of an icosahedral quasicrystal is shown in Fig. 2.3.

With their infinitely large unit cell quasicrystals can be regarded as a special type

of complex metallic alloy. Many of them are aluminum-based alloys (Al-Ni-Co, Al-Pd-Mn, Al-Cu-Fe, etc.) yet other compositions have also been discovered (Cd-Yb, Zn-Mg-Sc, etc.). The region of the phase diagram where these quasicrystals are stable is often very narrow. The neighboring phases usually are (complex) metallic alloys.

2.2.1 Generating aperiodic structures

To describe the structure of quasicrystals an extension of the conventional crystallography is necessary. A quasiperiodic pattern in d-dimensional space can be generated from a higher-dimensional configuration space. A common approach is the cut-and-project formalism. It uses an acceptance stripe to project a subset of the higher dimensional lattice into a lower-dimensional space. An example to generate a one-dimensional quasiperiodic sequence is shown in Fig. 2.4.

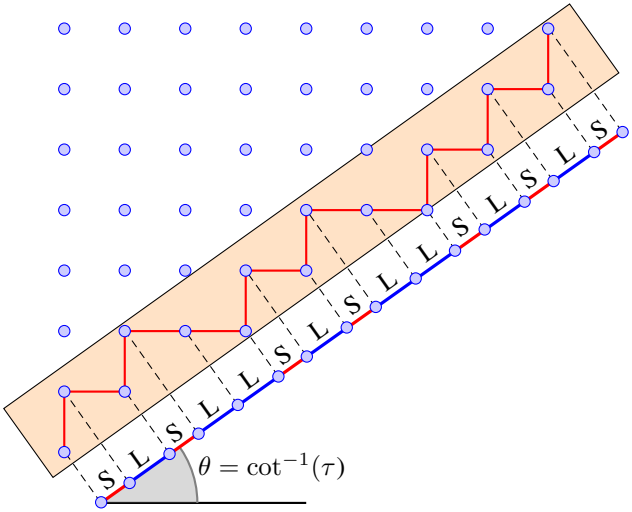

Figure 2.4: Creating a one-dimensional aperiodic sequence with the cut-and-project formalism. The acceptance stripe is shown in orange.

All points of the two-dimensional lattice that are within the acceptance stripe are projected onto a straight line. Two different distances are created, a short one S (marked red) and a long one L (marked blue). The sequence created with the

cut-and-project method is quasiperiodic if the hyperspace is cut by an irrational gradient and periodic for an rational one. For the two-dimensional example in Fig. 2.4, the resulting quasiperiodic pattern is a part of the well-known Fibonacci sequence. There are many other ways of generating it, in the end it can be reduced to the sequence $1, 1, 2, 3, 5, 8, 13, 21, \ldots$, the Fibonacci numbers F_n.

Another important property of quasicrystals is their relation to the golden mean τ. It can be calculated as $\tau = 2\cos(\pi/10) = (1 + \sqrt{5})/2$ and has the numeric value of approx. $1.618\,03$. Several ratios of the geometry of icosahedra, pentagons and decagons are related to τ. Many tilings and diffraction patterns can be in- or deflated by integer powers of τ, to yield patterns indistinguishable from the original.

2.2.2 Periodic approximants

In the literature many approximants of quasicrystals are studied. They are periodic structures, which can also be derived from the higher-dimensional description of the quasiperiodic lattice. Their unit cell is well-defined and finite with a similar local atomic arrangement as in the real quasicrystal.

To generate a Fibonacci quasicrystal with the cut-and-project formalism, the hyperspace has to be cut at an angle of $\theta = \cot^{-1}(\tau)$. If the golden mean is approximated by the ratio of two integer numbers, p/q, the resulting structure will be periodic. The integers p and q are chosen as two subsequent Fibonacci numbers, because of the following property:

$$\lim_{n\to\infty} \frac{F_n}{F_{n-1}} = \tau. \tag{2.1}$$

The periodic structures are then referred to as 1/1-, 2/1- or higher approximants of a quasicrystal.

Goldman and Kelton [44] give several reasons for studying approximants and why this can be helpful.

1. Quasicrystals typically form at compositions near those of crystalline approximant phases.
2. The approximants provide a well-defined starting point for models of the local atomic structure of quasicrystals
3. Both quasicrystalline and approximant phases have similar physical properties.

The properties of the approximants may be easier to understand theoretically, since all of the calculational mechanisms established for periodic crystals may be applied more readily to them.

All of the points mentioned above are obviously related. From the similarity of the composition a similarity in the local atomic arrangements and physical properties can be deduced. Approximants are important structures for studying the formation and stability of quasicrystals. They can be handled by tools developed for periodic structures, e.g. band-structure and phonon spectra calculations.

2.3 Clathrate systems

Another subtype of complex metallic alloys are clathrate systems. They can be characterized as host-guest structures, where guest atoms are trapped in the framework of the host structure. The first report of a clathrate system is from 1811 by Davy [28]. He discovered a hydrated clathrate system formed by chlorine and water molecules. The structure of these systems was solved with X-ray diffraction data by Pauling [92] in 1935. There are different structural modifications of hydrated clathrates, which are denoted by the roman letters I–VII. They differ in the structure of the cages in the framework, more details can be found in Karttunen *et al.* [57] and Fig. 2.5.

It was discovered that hydrated clathrates occur naturally at the ocean floor and the ice-cores of the Arctic and Antarctic. Under high pressure water can form the clathrate structure and trap gases such as methane or carbon dioxide. The interesting fact about these structures is their very low thermal conductivity when compared to ice. This fact makes them an interesting candidate for large scale hydrate deposits as an energy source.

The clathrate structure was also found for semiconducting group 14 elements. In 1965 Kasper *et al.* [58] discovered type I and II clathrates in the silicon-sodium system. Cros *et al.* [27] noted the fact, that clathrates are interesting because they are semiconductors with an adjustable band gap as early as 1970. The potential application as thermoelectric materials, however, was not considered for a long time. In 1998 Nolas *et al.* [87], using the "phonon glass – electron crystal" concept of Slack and Rowe [105], proposed clathrates as potential thermoelectric materials. That marked the beginning of the popularity of clathrates in thermoelectricity. This subject is covered in detail in chapter 3, the structural details of clathrates are discussed in the following subsection.

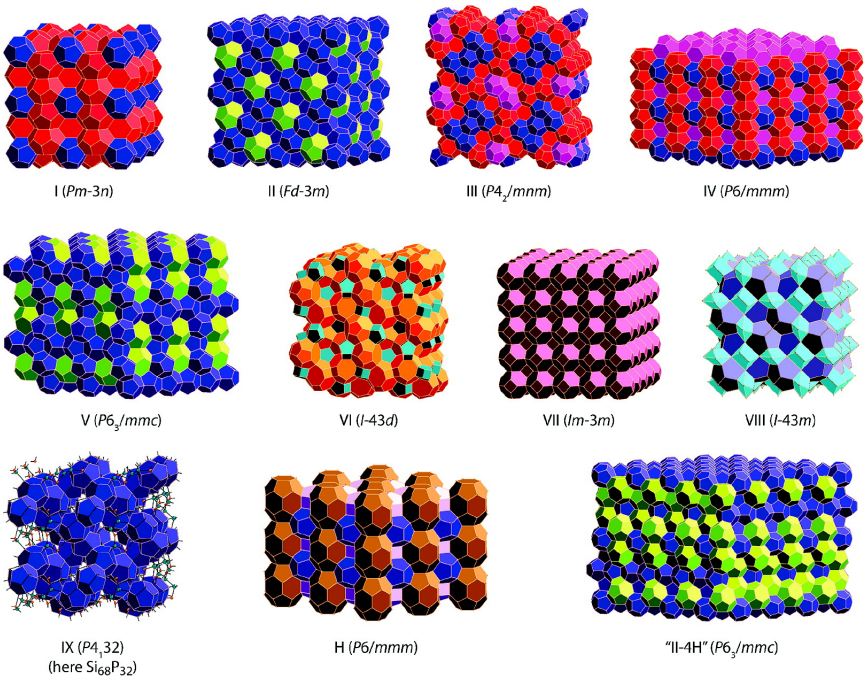

Figure 2.5: Different types of clathrate frameworks with the corresponding space group. The basic building blocks are given in the same color on the bottom. $[\alpha^b]$ stands for a cage with b α-membered rings, (M_x) gives the total number of atoms. From [57].

2.3.1 Structure of type I clathrates

The clathrates investigated in this work are all of the type I crystal structure. They can contain up to 54 atoms per unit cell. The space group is $Pm\bar{3}n$, with the Wyckoff positions given in Tab. 2.1. Different modifications of this structure have been found in experiment. There is an empty structure, Ge_{46}, where only the host framework is present. In binary systems the cages are filled with guest atoms. An example is the Ba_8Si_{46} structure. For ternary systems some atoms of the framework are then being replaced with a third element, e.g. in $Ba_8Ge_{40}Au_6$.

Multiplicity	Wyckoff letter	Site symmetry	
2	a	$m\bar{3}.$	inside small cage
6	d	$\bar{4}m.2$	inside large cage
6	c	$\bar{4}m.2$	host framework
16	i	.3.	host framework
24	k	$m..$	host framework

Table 2.1: Crystallographic lattice sites in type I clathrate systems.

The basic building blocks of type I clathrates are two cage-like structures. A dodecahedron and a tetrakaidecahedron formed by 20 and 24 atoms, respectively. They are shown as red and teal atoms in Fig. 2.6. A single unit cell contains two dodecahedra and six tetrakaidecahedra. The dodecahedra a form a bcc lattice, while the tetrakaidecahedra fill the remaining gaps. This is illustrated in Fig. 2.7.

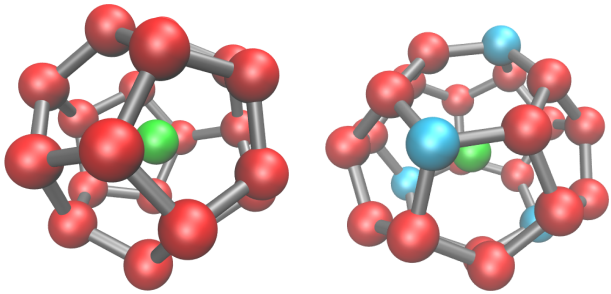

Figure 2.6: Cage structures in the framework of type I clathrates. Left: Dodecahedron formed by 20 red atoms. The central atom is shown in green. Right: Tetrakaidecahedron formed by 24 red and teal atoms.

In a binary system, the cages are filled. The most typical guest atoms are alkali, alkaline-earth and halogen atoms. Depending on the size of the framework atoms, it is necessary to introduce vacancies to stabilize the system. This is the case for $Ba_8Ge_{43}\square_3$. Three of the germanium atoms sitting on the $6c$ position are replaced by vacancies. This position is shared between four adjacent tetrakaidecahedra, it is shown in teal in Fig. 2.6 and 2.7.

The type I clathrate structure has also been found in ternary alloys. For the germanium system this are in particular $Ba_8Zn_xGe_{46-x-y}\square_y$ [4], $Ba_8Au_{5.3}Ge_{40.7}$ [122] and $Ba_8Ni_{3.5}Ge_{42.1}\square_{0.4}$ [86]. As for the binary systems, vacancies are required to stabilize the structure.

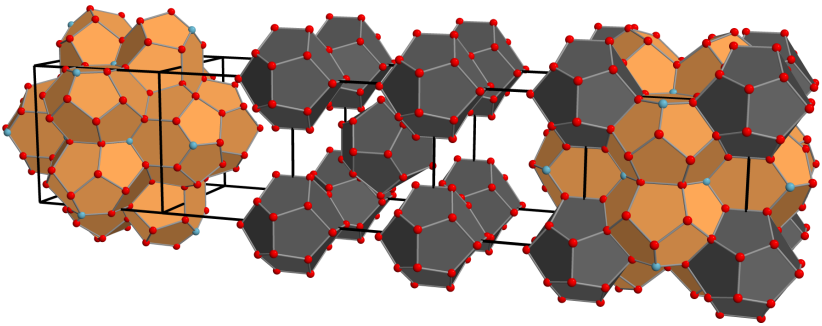

Figure 2.7: Spatial arrangement of the two types of clusters in a type I clathrate. The left and central cells show the arrangement of the six tetrakaidecahedra and two dodecahedra in the unit cell, respectively. The entire unit cell with both types of cages is shown on the righthand side.

The silicon-based type I clathrate systems have been investigated very thoroughly because of their superconducting properties [53]. Especially the clathrates $Ba_8TM_xSi_{46-x}$ (with TM = Au, Ag, Cu) have shown promising results. A clathrate I structure where different atoms occupy the different cages was reported by Böhme *et al.* [18]. In the $Na_2Ba_6Si_{46}$ structure the dodecahedra host a sodium atom while the tetrakaidecahedra host a barium atom.

2.3.2 Structure of type II clathrates

The first intermetallic type II clathrate structure was reported by Guloy *et al.* [47] in 2006. Like the type I clathrates, their framework consists of tetrahedrally

coordinated group 14 atoms, which are arranged in two cages. The dodecahedron $[5^{12}]$ cage, made up from 20 atoms is the same as in type I. Instead of the 24 atom tetrakaidecahedron a 28 atom hexakaidecahedron $[5^{12}6^4]$ is found. Each unit cell contains 16 dodecahedra and 8 hexakaidecahedra. These cages allow for 24 guest atoms, giving rise to the formula $\square_{24}Ge_{136}$.

Each hexakaidecahedron is surrounded by 16 dodecahedra, forming a super-tetrahedron (Fig. 2.8). The edges of this tetrahedron are aligned along the face diagonals of the cubic unit cell.

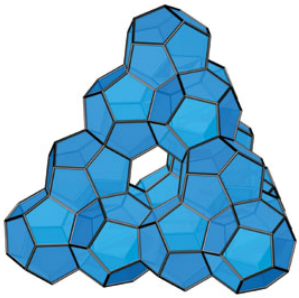

Figure 2.8: Sixteen dodecahedra in a type II clathrate structure. They form a super-tetrahedron, whose edges run parallel to the face diagonal of the unit cell. From [47].

Besides the germanium structure, type II clathrates were also discovered with silicon frameworks. The Na_xSi_{136} ($0 \leq x \leq 24$) structure was reported in 1965 by Kasper *et al.* [58]. Due to the lack of single crystal samples the physical properties could only be measured for microcrystalline specimens. In 2010 the first single crystal measurements were reported by Beekman *et al.* [12]. With special techniques it is now possible to create an almost empty Si clathrate Na_xSi_{136} ($x < 1$).

The applications for type II clathrate system, however, differ from the type I structures. The thermal conductivity is higher, so the overall thermoelectric efficiency is lower. The type II clathrates have also been investigated in theory and shown interesting optical properties, making them promising materials for optoelectronic devices [1].

Chapter 3:

Thermoelectric materials

In 2010 the world energy consumption was about 363 EJ[1]. While it is unlikely that this value will decrease in the foreseeable future, alternative ways of reducing the net energy consumption have to be investigated. Besides making processes more energy efficient, the recovery of energy from waste heat is of great interest in many different fields of applications.

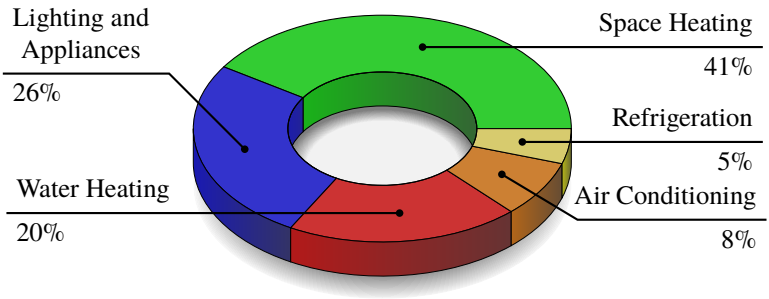

Figure 3.1: Domestic energy consumption in the United States in 2005. Source: U.S. Energy Information Administration, *Residential Energy Consumption Survey 2005*.

In the industrialized part of the world, there are usually four major sectors consuming energy. The largest is industry, followed by transportation, residential and

[1] according to *Key World Energy Statistics 2012* of the International Energy Agency, http://www.iea.org/publications/freepublications/publication/kwes.pdf

commercial use. The domestic energy consumption is shown in detail in Fig. 3.1. Almost 75 % of the energy is used for heating or cooling, one quarter for lighting and other appliances. In industry a large part is required for mechanical processes as well as heating or cooling.

The maximum efficiency for any thermodynamic process is given by the Carnot efficiency. It is defined as

$$\eta_{\text{Carnot}} = 1 - \frac{T_c}{T_h}, \tag{3.1}$$

where T_c and T_h are the lowest and highest temperatures occurring in the process. In every day work cycles this efficiency is never reached. The energy efficiency for mechanical processes is usually in the range of 0.1 to 0.5, for heating it is a little better, ranging from 0.3 to 0.8. This means that often only a small fraction of the energy is used and most of it is lost due to various effects.

With thermoelectric materials it is possible to convert a temperature gradient into an electric voltage and vice versa. Using these materials to recover electric energy from waste heat, the net energy consumption could be dramatically reduced. The problem with these materials is that they have a very low efficiency of about $10\,\%$. One aspect of recent research is finding thermoelectric materials with a higher efficiency. Another approach tries to manipulate the underlying physical properties of currently used materials to achieve a better conversion ratio.

In this chapter the basic principles of thermoelectric materials are presented. The different properties like electric and thermal conductivity are discussed and some examples for recent advances in the field are given. A more comprehensive introduction as well as a review on thermoelectrics is given by Nolas *et al.* [88].

3.1 History and technological applications

The development of thermoelectric materials happened during three distinct periods of time. In the decades from 1820 to 1850 the basic effects were discovered. Macroscopic explanations were found and their application in thermometry was recognized. For about 80 years there was no real progress. In the late 1930s the microscopic processes were understood and new materials were discovered. Most of today's thermoelectrics were developed in the late 1950s and 1960s. The development of the thermoelectric efficiency for this period is shown in Fig. 3.2.

The latest period of thermoelectric research started in the 1990s, when new com-

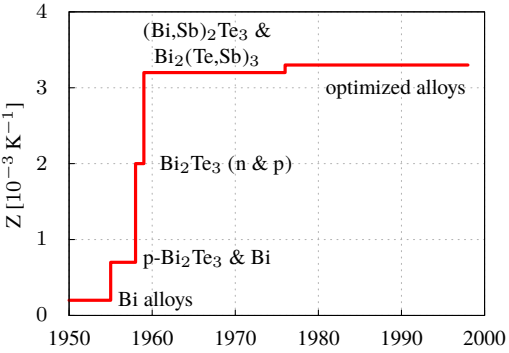

Figure 3.2: Development of the figure of merit of thermoelectric materials near room temperature during the 20th century. Adapted from [88].

pounds like skutterudites and clathrates were identified as possible thermoelectric materials. The recent activities concentrate on systems that can be characterized with the "phonon glass–electron crystal" (PGEC) concept of SLACK and ROWE [105].

Established materials

Before the latest research period in the 1990s, different compounds have been used for thermoelectric refrigeration. The most simple structure is bismuth telluride (Bi_2Te_3) with the space group D^5_{3d} [70]. It is also indicated in Fig. 3.2. The properties have been measured in great detail for both n- and p-type materials. Although it is not the best thermoelectric material, it is still of interest for the compounds it forms.

The two structures antimony telluride (Sb_2Te_3) and bismuth selenide (Bi_2Se_3) are not as good thermoelectric materials as Bi_2Te_3. However, they both have the same crystal structure as bismuth telluride. The addition of one or two to Bi_2Te_3 can greatly improve the thermoelectric properties.

There is complete solid solubility among the three compounds Bi_2Te_3, Sb_2Te_3 and Bi_2Se_3. A complete study of this pseudoternary system has not been attempted. This is because the best p-type material has a composition close to the $Bi_{2-x}Sb_xTe_3$ pseudobinary system and the best n-type material is close to the $Bi_2Te_{3-y}Se_y$

pseudobinary system. The thermoelectric efficiency of these materials is still very low, yet about $50\,\%$ higher than for simple alloys (cf. Fig. 3.2).

Other systems that have shown promising results are the bismuth and bismuth with antimony systems. Their thermoelectric efficiency is slightly worse than the previously described materials. However, if they are subjected to a magnetic field, the efficiency can be increased up to a factor of 2. This is a distinct disadvantage, because the strength of the magnetic field has to be in the order of $1\,\mathrm{T}$.

One of the first materials that was studied during the revival of interest in the middle of the twentieth century was lead telluride (PbTe). It has a higher melting temperature than Bi_2Te_3, $923\,^\circ\mathrm{C}$ compared to $585\,^\circ\mathrm{C}$. At room temperature the thermoelectric efficiency is lower than for Bi_2Te_3, but at higher temperatures it eventually becomes superior. As for the bismuth systems it is preferable to use solid solutions rather than simple compounds. Alloys can be formed by substituting tin for lead or by substituting sulfur or selenium for tellurium.

Another system that has a comparable thermoelectric efficiency is the so-called TAGS system. It stands for alloys containing the elements Te, Ag, Ge and Sb. They are essentially alloys between the compounds $AgSbTe_2$ and GeTe and closely related to the lead telluride system.

Since neither silicon nor germanium have properties, that yield good thermoelectric devices, it is surprising that solid solutions between the two elements form alloys which can be used for thermoelectric applications. This is mainly due to the significant reduction of the lattice thermal conductivity, which is about one order of magnitude smaller for the alloy when compared to the single elements. Their thermoelectric efficiency, however, is only comparable to the bismuth and lead systems at temperatures above $1000\,\mathrm{K}$.

3.2 Thermoelectric effects

The general term thermoelectric effects usually comprises three effects. In 1821 Thomas Seebeck discovered, that a compass needle is deflected by a metal to which a thermal gradient is applied. He had two metal rods which were connected at both ends. If the contacts had different temperatures, a magnetic field was created. He therefore called the effect “thermomagnetic”. The magnetic field, however, was only created by the induced current in the metals. This mistake was later corrected by Ørsted, who coined the term “thermoelectricity”. The effect to convert a temperature gradient into an electric voltage was named after it’s discoverer, the Seebeck effect.

The inverse effect was discovered by Jean Peltier in 1834. If an electric current runs over the contact of two metals, heat is created. Depending on the sign of the current this heat can be either created or consumed. A simple explanation for this effect can be found with the band theory of solids. The chemical potentials of the two metals at the junction are aligned, which leads to an energy difference in the conduction bands in the two metals. Electrons which cross the junction either have to gain or lose energy to enter the other band. This energy is taken from or stored in phonon modes, which heat up or cool down the junction.

The third effect, called the Thomson effect, was observed in in 1851 by Lord Kelvin. All current-carrying conductors, except for superconductors, with a temperature difference between two points either absorb or emit heat.

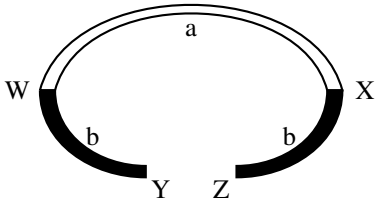

Figure 3.3: Schematic drawing of a basic thermocouple. It consists of two different materials a and b, which are connected at the two points W and X. The voltage is measured at the contact points Y and Z. Adapted from [88].

A basic thermoelectric circuit is shown in Fig. 3.3. There all three mentioned effects can be observed. The Seebeck, Peltier and Thomson coefficients α, Π and τ, respectively, can be defined like this. Two different metals, a and b, have junctions at W and X. If a temperature difference is created between these two points, a voltage V can be measured between the points Y and Z. The Seebeck coefficient is then defined as

$$\alpha_{\mathrm{ab}} = \frac{\mathrm{d}V}{\mathrm{d}T}. \tag{3.2}$$

The Peltier coefficient Π relates the heat Q, which is dissipated at the junctions, to the current I,

$$Q = \Pi_{\mathrm{ab}} I. \tag{3.3}$$

If a current is flowing and a temperature gradient is present, then there is also heat generated or absorbed within the thermocouple because α is temperature-dependent. The gradient of the heat current is given by

$$\frac{\mathrm{d}Q}{\mathrm{d}s} = \tau I \frac{\mathrm{d}T}{\mathrm{d}s}, \tag{3.4}$$

where s is a spatial coordinate and τ the Thomson coefficient.

3.3 Figure of Merit

The performance of a thermoelectric material is measured by the figure of merit Z. It is defined as

$$Z = \frac{\alpha^2 \sigma}{\kappa_L + \kappa_e}, \tag{3.5}$$

where α is the Seebeck coefficient, σ the electric conductivity and $\kappa_{L,e}$ the thermal conductivity of the lattice and the electrons, respectively. The figure of merit has the dimension of K^{-1}. It is common to multiply it with an absolute temperature T to yield the dimensionless number ZT.

The higher ZT for a specific material is, the greater the thermoelectric efficiency is. For the common thermoelectric materials as described in Sec. 3.1 a ZT value of 0.5 to 1.5 can be found. For special materials, the generally desired threshold value of 2 has been reached. In 2001 Venkatasubramanian *et al.* [118] reported a ZT value of about 2.4 at room temperature for a thin-film Bi_2Te_3/Sb_2Te_3 superlattice device. With the use of nanostructuring and mesoscale modeling a ZT value of ~ 2.2 at $915\,\mathrm{K}$ could be reached by Biswas *et al.* [17] for a bulk material in 2012.

Clathrate structures also have ZT values in the range of 0.5 to 1.5. One of the best materials is $Ba_8Ga_{16}Ge_{30}$ with $ZT = 1.35$ at $900\,\mathrm{K}$. An overview of several clathrate thermoelectrics is given by Kleinke [61].

The challenging fact about the optimization of the ZT value is that the quantities given in Eq. (3.5) are not independent of one another. To achieve a high thermopower, the Seebeck coefficient as well as the electric conductivity should be high while the thermal conductivity should be as low as possible. In metals there is usually a correlation between the electric and thermal conductivity. By changing one, the other is also changed because of the physical principles of the conduction processes. This lead to the "phonon glass–electron crystal" concept

[105]. To yield a high ZT value a material should behave like a glass for phonons and a crystal for electrons.

The following subsections will give brief introductions into the transport coefficients. More detailed explanations are given in NOLAS *et al.* [88].

3.3.1 Thermal conductivity

The conduction of heat in a solid is based on two processes. The electrons and the lattice contribute in different amounts, depending on the temperature. For thermoelectric devices the lattice part is the interesting one. The electronic part of the thermal conductivity is closely related to the electric conductivity and the Seebeck coefficient. To get a high ZT value, the lattice part, κ_L, should be as low as possible. In the following the mechanism of the lattice heat transport is discussed.

From the kinetic gas theory the following approximation for the thermal conductivity can be found:

$$\kappa = \frac{1}{3} C v l, \tag{3.6}$$

where C is the heat capacity per unit volume, v the average particle velocity and l the mean free path of a particle between collisions. This result was first applied by Debye to describe thermal conductivity in dielectric solids, with C as the heat capacity of the phonons, v the phonon velocity, and l the phonon mean free path.

The propagation of phonons in a crystal is restricted by two processes, the scattering on defects and the scattering by other phonons. For purely harmonic forces between atoms there are no phonon-phonon interactions and their mean free path l would only be restricted by the crystal boundaries and defects. The thermal conductivity in this case would be infinite. For anharmonic interactions there is a phonon-phonon interaction, which leads to a finite mean free path and a finite thermal conductivity.

At room temperature the thermal conductivity is dominated by phonon-phonon scattering. The most important processes involve three phonons and can be of two kinds. In the N-processes two phonons with wave vectors $\boldsymbol{k}_1$ and $\boldsymbol{k}_2$ interact to form a third phonon with wave vector $\boldsymbol{k}_3$ such that

$$\boldsymbol{k}_1 + \boldsymbol{k}_2 = \boldsymbol{k}_3. \tag{3.7}$$

The energy and momentum are conserved in this case, which only leads to a redis-

tribution of the phonons but not to a thermal resistance. In Umklapp or U-processes the momentum is not conserved. They do not have the form of Eq. (3.7) which conserves the total momentum $\boldsymbol{K}$. Instead

$$\boldsymbol{k}_1 + \boldsymbol{k}_2 = \boldsymbol{k}_3 + \boldsymbol{G}, \tag{3.8}$$

where $\boldsymbol{G}$ is a reciprocal lattice vector. The sum of the two wave vectors $\boldsymbol{k}_1$ and $\boldsymbol{k}_2$ lies outside of the Brillouin zone. By subtracting a reciprocal lattice vector $\boldsymbol{G}$ the result is mapped back into the Brillouin zone. This is illustrated in Fig. 3.4.

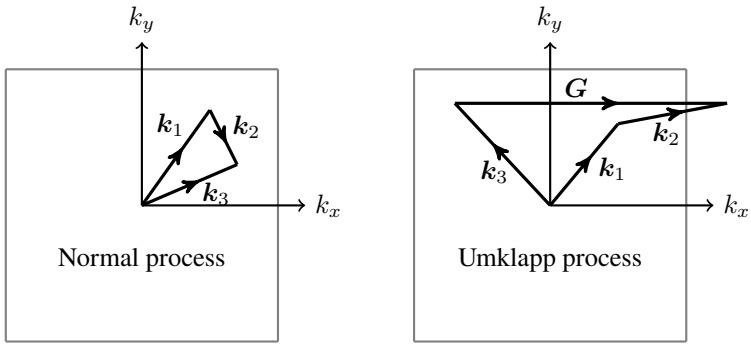

Figure 3.4: Two-dimensional representation of phonon-phonon scattering processes. The gray square represents the first Brillouin zone. Left: N-process, the total momentum is conserved. Right: U-process, the total momentum is not conserved.

The scattering of phonons by defects is only important for very low temperatures. The phonon mean free path l is then comparable to the dimensions of the crystal and the phonons are scattered at the crystal boundaries. A discussion of the scattering by the various point defects in crystals can also be found in [88].

3.3.2 Electric conductivity

The basic concept behind the electric conductivity is the band theory of solids. According to quantum theory the energy levels of electrons in a solid are band-like, which are separated from each other by forbidden zones. All charge carriers in the so-called conduction band can contribute to the transport of electric current.

In a perfectly periodic crystal the solution of the wave equation for an electron are Bloch waves. The electrons can move freely within the crystal, there are only certain restrictions to their energy levels and wave vectors.

The transport properties however do not depend on the concentration of charge carriers. This would lead to an infinite value for a perfectly periodic potential. The electric resistivity depends mainly on the scattering of the charge carriers. At elevated temperature the main source of scattering are phonons, for low temperatures it is the impurities and the defects.

Part II.

Algorithms and numerical methods

Chapter 4:

Ab initio simulations

After the discovery of the atomistic structure of matter at the beginning of the 20th century the stage was set for the formulation of the laws of quantum mechanics. This theory takes the existence of electrons and nuclei into account and allows for precise predictions of physical phenomena. About one century later, a theoretical approach for efficient computational methods that can treat a system of many electrons and nuclei is, however, still a great challenge.

After a short historical overview of the development of quantum theory and the different theoretical approaches to a quantum many-body system, several important concepts like density functional theory, pseudopotentials and basis functions will be introduced. This part will loosely follow the book of Martin [77], which provides many more details on all of these subjects. At the end of the chapter, the VASP code and the algorithms used therein will be presented.

4.1 History

The evolution of quantum theory started in the 1890s with the discovery of the electron by Lorentz, Zeeman and Thomson. They all predicted charged particles with a very small mass within the atoms. The corresponding positive mass, the proton, was first seen by Rutherford in 1911 in his famous scattering experiment of alpha particles. The atomic model of Bohr from 1913 tried to explain the stability of atoms by only allowing a discrete set of levels for electrons. Even though his model had some fundamental flaws, it inspired many famous physicists like Schrödinger, Heisenberg and de Broglie and finally led to the theory of quantum mechanics.

A very important steps was the introduction of the wave-particle duality. Einstein postulated this already in 1905 for light waves or photons and de Broglie generalized it for all particles in 1924. It relates the wavelength λ of a particle to its momentum p by

$$\lambda = \frac{h}{p},$$

with h being Planck's constant. Based on this theory, Schrödinger generalized the concept of particle waves in 1926. He found the equation for the propagation of these waves – the Schrödinger equation – which allows for the mathematical description of a quantum system. It can be obtained with a simple correspondence rule from the Hamilton function of the related classical system. The Schrödinger equation is the basic element of the wave formulation of quantum mechanics.

A different notation for quantum mechanics, the matrix formulation, had been found by Heisenberg, Born and Jordan one year before. Schrödinger could show that the wave and matrix formulations are equivalent. A generalization to the quantum theory we know today was done by Dirac shortly afterwards. He introduced the Bra-Ket notation, which is used as a standard way of representing quantum states in an abstract way. It represents the wavefunction or any other states of a quantum system with vectors in Hilbert space and allows for calculations without specifying a concrete basis.

In the 1920s and '30s many basic principles of quantum mechanics were discovered. Heisenbergs uncertainty principle, the exclusion principle of Pauli, the Fermi-Dirac and Bose-Einstein statistics and the symmetry or antisymmetry of the wavefunction of identical particles. Together with the formulation of relativistic quantum mechanics and the laws of statistical mechanics, these principles form the basis of all modern theories of atoms, molecules and condensed matter.

Over the course of the 20th century there were also great efforts made in developing accurate and fast algorithms to solve quantum mechanical problems numerically. The currently used methods are presented in sections 4.2 to 4.4.

The outlook for the future of *ab initio* simulations is very promising. With ever increasing computer power and new and improved algorithms, the number of possible scenarios for quantum mechanical calculations will be growing steadily. Especially with the possibility of finite-temperature and non-equilibrium simulations, which are non-trivial in an *ab initio* framework, these methods could be applied to a multitude of currently inaccessible problems.

4.2 The quantum many-body problem

In quantum mechanics the operator for the total energy is the Hamiltonian. For a system of electrons and nuclei it can be written as

$$\hat{H} = \hat{H}_{NN} + \hat{H}_{ee} + \hat{H}_{Ne}. \tag{4.1}$$

There are three contributions with the indices N for nuclei and e for electrons. The first term in (4.1) represents the kinetic energy and the interaction of the nuclei:

$$\hat{H}_{NN} = -\sum_{\alpha} \frac{\hbar^2}{2M_\alpha} \nabla_\alpha^2 + \frac{1}{2} \sum_{\substack{\alpha,\beta \\ \alpha \neq \beta}} \frac{Z_\alpha Z_\beta e^2}{|\boldsymbol{R}_\alpha - \boldsymbol{R}_\beta|}. \tag{4.2}$$

Upper case and greek subscript letters are used to indicate nuclei, lower case and latin subscripts for electrons. The second term, $\hat{H}_{ee}$, is equivalent to the first one, except it describes electrons.

$$\hat{H}_{ee} = -\sum_{i} \frac{\hbar^2}{2m} \nabla_i^2 + \frac{1}{2} \sum_{\substack{i,j \\ i \neq j}} \frac{e^2}{|\boldsymbol{r}_i - \boldsymbol{r}_j|} \tag{4.3}$$

The last term represents the interaction between the electrons and the nuclei:

$$\hat{H}_{Ne} = -\sum_{\alpha} \sum_{i} \frac{Z_\alpha e^2}{|\boldsymbol{r}_i - \boldsymbol{R}_\alpha|}. \tag{4.4}$$

The ground state of a non-relativistic quantum system can be calculated with the time-independent Schrödinger equation,

$$\hat{H}\Psi(\boldsymbol{r}_i, \boldsymbol{R}_\alpha) = E\Psi(\boldsymbol{r}_i, \boldsymbol{R}_\alpha), \tag{4.5}$$

where the many-body wavefunction

$$\Psi(\boldsymbol{r}_i, \boldsymbol{R}_\alpha) \equiv \Psi(\boldsymbol{r}_1, \ldots, \boldsymbol{r}_n, \boldsymbol{R}_1, \ldots, \boldsymbol{R}_N)$$

depends on the coordinates of the n electrons and the N nuclei. The time evolution

of the eigenstates of Eq. (4.5) is then given by $\Psi e^{-i(E/\hbar)t}$.

Solving the Schrödinger equation for the Hamiltonian given in Eq. (4.1) is not possible. Even for small systems containing only a few atoms the complexity of this problem is far beyond the capabilities of any currently available computer. For a single oxygen atom with eight electrons the amount of data is already incredibly large. Assuming 10 bytes are required to store a single value of the many-body wavefunction at a discrete point in space, the storage capacity needed for the entire function can be calculated. For a $10\times10\times10$ grid about 10^{24} bytes are needed, which could be stored on a trillion 1 TB hard drives.

The quantum many-body problem is thus only solvable within some approximations.

The Born-Oppenheimer approximation

The Born-Oppenheimer or adiabatic approximation is a very fundamental part of most theoretical approaches to the quantum many-body problem. It makes use of the fact, that the mass of the electrons is much smaller than the mass of the nuclei. Therefore the term for the kinetic energy of the nuclei is "small" when compared to the electron. The Born-Oppenheimer approximation can be thought of in different ways:

- The nuclei are decoupled from the electrons
- The electrons follow the motion of the nuclei adiabatically
- There is no exchange of energy between nuclei and electrons

As a consequence the first term in Eq. (4.2) can be neglected and the nuclei are considered as frozen at the positions $\{\boldsymbol{R}_\alpha\}$. The Schrödinger equation (4.5) can then be written as

$$\left[\hat{H}_{ee} + \hat{H}_{Ne} + \frac{1}{2}\sum_{\alpha,\beta}\frac{Z_\alpha Z_\beta e^2}{|\boldsymbol{R}_\alpha - \boldsymbol{R}_\beta|}\right]\phi = \varepsilon\phi. \tag{4.6}$$

The wavefunction ϕ and the energy ε depend on the positions of the nuclei only as parameters

$$\phi = \phi(\boldsymbol{r}_i, \{\boldsymbol{R}_\alpha\}) \qquad \text{and} \qquad \varepsilon = \varepsilon(\{\boldsymbol{R}_\alpha\}). \tag{4.7}$$

The $\varepsilon(\{\boldsymbol{R}_\alpha\})$ can be identified as a potential energy of the nuclei.

Rephrasing Eq. (4.5) yields

$$\left[-\sum_{\alpha}\frac{\hbar^2}{2M_\alpha}\nabla_\alpha^2+\varepsilon(\{\boldsymbol{R}_\alpha\})\right]\varphi=E^*\varphi, \tag{4.8}$$

where $\varphi=\varphi(\boldsymbol{R}_\alpha)$ is the wave function of the nuclei. The energy E^* is the total energy E from Eq. (4.5). Using this approach, the wavefunction Ψ can be separated into a part for the nuclei and a part for the electrons:

$$\Psi(\boldsymbol{r}_i,\boldsymbol{R}_\alpha)=\phi(\boldsymbol{r}_i,\{\boldsymbol{R}_\alpha\})\cdot\varphi(\boldsymbol{R}_\alpha). \tag{4.9}$$

Ignoring the nuclear kinetic energy, the Hamiltonian for the electrons can then be written as

$$\hat{H}=\hat{T}+\hat{V}_{\text{ext}}+\hat{V}_{\text{int}}+E_{\text{II}}. \tag{4.10}$$

The operator for the kinetic energy of the electrons is

$$\hat{T}=-\sum_i\frac{\hbar^2}{2m}\nabla_i^2,$$

$\hat{V}_{\text{ext}}$ is the potential acting on the electrons due to the nuclei,

$$\hat{V}_{\text{ext}}=\sum_{i,\alpha}V_\alpha(|\boldsymbol{r}_i-\boldsymbol{R}_\alpha|),$$

and $\hat{V}_{\text{int}}$ is the electron-electron interaction,

$$\hat{V}_{\text{int}}=\frac{1}{2}\sum_{i\neq j}\frac{e^2}{|\boldsymbol{r}_i-\boldsymbol{r}_j|}.$$

The final term E_{II} in Eq. (4.10) is the interaction of the nuclei with each other and also includes terms that contribute to the total energy of the system. The effect of the nuclei upon the electrons is put into an effective external potential for the electrons, $\hat{V}_{\text{ext}}$. In this way, the Hamiltonian is still valid for pseudopotentials (see Sec. 4.3.3) or other external fields.

The variational principle

The expectation value of an operator $\hat{O}$ for an eigenstate is given by the time independent expression

$$\langle \hat{O} \rangle = \frac{\langle \Psi | \hat{O} | \Psi \rangle}{\langle \Psi | \Psi \rangle}, \tag{4.11}$$

which involves an integral over all coordinates. For the total energy, which is represented by the Hamiltonian from equation (4.10), this yields

$$E = \frac{\langle \Psi | \hat{H} | \Psi \rangle}{\langle \Psi | \Psi \rangle} \equiv \langle \hat{H} \rangle = \langle \hat{T} \rangle + \langle \hat{V}_{\text{int}} \rangle + \int d\boldsymbol{r}\, V_{\text{ext}}(\boldsymbol{r}) n(\boldsymbol{r}) + E_{\text{II}} \tag{4.12}$$

The expectation value of the external potential has been explicitly written as an integral over the particle density $n(\boldsymbol{r})$, defined as

$$n(\boldsymbol{r}) = \frac{\langle \Psi | \hat{n}(\boldsymbol{r}) | \Psi \rangle}{\langle \Psi | \Psi \rangle}, \qquad \text{where} \qquad \hat{n}(\boldsymbol{r}) = \sum_i \delta(\boldsymbol{r} - \boldsymbol{r}_i). \tag{4.13}$$

The nucleus-nucleus term E_{II} is important for total energy calculations, for the electronic structure, i.e. the wavefunctions, it is only a classical additive term.

The basic task of *ab initio* simulation programs is finding the eigenstates of the many-body Hamiltonian. These eigenstates are stationary points of the energy expression Eq. (4.12). Using the variational principle this can be expressed as

$$\delta \left[\langle \Psi | \hat{H} | \Psi \rangle - E \left(\langle \Psi | \Psi \rangle - 1 \right) \right] = 0, \tag{4.14}$$

where the orthonormality of the wavefunction ($\langle \Psi | \Psi \rangle = 1$) is ensured with a Lagrange multiplier. This is equivalent to the Rayleigh-Ritz variation method.

The ground state wavefunction Ψ_0 can thus be obtained by minimizing the total energy with respect to all parameters in $\Psi(\{\boldsymbol{r}_i\})$.

4.3 Density functional theory

The basic consequence of density functional theory is that any property of a system of many interacting particles can be calculated as a functional of the ground state

density $n_0(\boldsymbol{r})$. It has become the primary tool for calculating the electronic structure of condensed matter and is increasingly popular for molecules and other finite systems.

The modern formulation of density functional theory was given by HOHENBERG and KOHN [54] in 1964. They proved that the density of the particles can be considered a "basic variable", from which all properties of the systems are unique functionals. This concept was extended to finite temperature canonical and grand canonical ensembles in 1965 by MERMIN [79]. In the same year the work of KOHN and SHAM [62] was published, which is the basis of most modern approaches to calculating the electronic structure of atoms, molecules and condensed matter.

The approach of HOHENBERG and KOHN is to formulate density functional theory as an exact theory of a many-body system. This formalism can be applied to any system of interacting particles in an external potential $V_{\text{ext}}(\boldsymbol{r})$, especially to electrons and fixed nuclei, where the Hamiltonian can be written as

$$\hat{H} = -\frac{\hbar^2}{2m_e}\sum_i \nabla_i^2 + \sum_i V_{\text{ext}}(\boldsymbol{r}_i) + \frac{1}{2}\sum_{i\neq j}\frac{e^2}{|\boldsymbol{r}_i - \boldsymbol{r}_j|}. \tag{4.15}$$

The basis are the following two theorems [77], which can be proven very easily [54]:

Theorem I: For any system of interacting particles in an external potential $V_{\text{ext}}(\boldsymbol{r})$, the potential $V_{\text{ext}}(\boldsymbol{r})$ is determined uniquely, except for a constant, by the ground state particle density $n_0(\boldsymbol{r})$.

As a conclusion of this theorem, the Hamiltonian is fully determined, except for a constant shift of the energy. Thus the many-body wavefunction is also fully determined for all ground and excited states. This means that all properties of the system are completely determined simply be the ground state density $n_0(\boldsymbol{r})$.

Theorem II: A universal functional for the energy $E[n]$ in terms of the density $n(\boldsymbol{r})$ can be defined, valid for any external potential $V_{\text{ext}}(\boldsymbol{r})$. For any particular $V_{\text{ext}}(\boldsymbol{r})$, the exact ground state energy is the global minimum value of this functional, and the density $n(\boldsymbol{r})$ that minimizes the functional is the exact ground state density $n_0(\boldsymbol{r})$.

This implies, that the functional $E[n]$ is sufficient to determine the exact ground state energy and density. This only holds for ground states, for excited states requires additional information, such as the free-energy functional [79].

The total energy functional for a system of interacting particles is given by

$$E_{\mathrm{HK}}[n] = T[n] + E_{\mathrm{int}}[n] + \int d\boldsymbol{r}\, V_{\mathrm{ext}}(\boldsymbol{r}) n(\boldsymbol{r}) + E_{\mathrm{II}} \tag{4.16}$$

$$\equiv F_{\mathrm{HK}}[n] + \int d\boldsymbol{r}\, V_{\mathrm{ext}}(\boldsymbol{r}) n(\boldsymbol{r}) + E_{\mathrm{II}}, \tag{4.17}$$

which can be derived from Eq. (4.10). The functional $F_{\mathrm{HK}}[n]$ includes all internal energies, potential and kinetic, of the interacting electron system,

$$F_{\mathrm{HK}}[n] = T[n] + E_{\mathrm{int}}[n]. \tag{4.18}$$

The Hohenberg-Kohn theorems however are not enough to perform electron structure calculations. An instruction on how to determine the energy functional $E[n]$ is required, which was given only one year later.

4.3.1 The Kohn-Sham equations

In 1965 Kohn and Sham proposed an ansatz, that is the most widely used for electronic structure calculations [62]. Instead of using the original many-body problem, they solved an auxiliary independent-particle problem. Using a self-consistent method, the Kohn-Sham approach involves independent particles but an interacting density.

The ansatz assumes that the density of the ground state of the original interacting system is equal to that of some chosen non-interacting system. This leads to independent-particle equations for the non-interacting system. They can be solved exactly with numerical methods, the complicated many-body terms are incorporated into an exchange-correlation functional of the density. It can be shown that the accuracy of the results for this auxiliary system depends only on the approximation for the exchange-correlation functional.

The Kohn-Sham equations are based on the total energy functional of the Hohenberg-Kohn theorem 4.17. The ground state energy functional is rewritten in the form

$$E_{\mathrm{KS}} = T_S[n] + \int d\boldsymbol{r}\, V_{\mathrm{ext}}(\boldsymbol{r}) n(\boldsymbol{r}) + E_{\mathrm{Hartree}}[n] + E_{\mathrm{II}} + E_{\mathrm{XC}}[n], \tag{4.19}$$

with the independent-particle kinetic energy T_S and the classical Coulomb interac-

tion energy of the electron density $n(\boldsymbol{r})$ with itself,

$$E_{\text{Hartree}}[n] = \frac{1}{2}\int d\boldsymbol{r}\, d\boldsymbol{r}\,' \frac{n(\boldsymbol{r})n(\boldsymbol{r}')}{|\boldsymbol{r}-\boldsymbol{r}'|}, \tag{4.20}$$

known as the Hartree energy.

All many-body effects of exchange and correlation in Eq. (4.19) are grouped into the exchange-correlation energy E_{XC}. It can be written in the form

$$E_{\text{XC}}[n] = \langle \hat{T} \rangle - T_S[n] + \langle \hat{V}_{\text{int}} \rangle - E_{\text{Hartree}}[n]. \tag{4.21}$$

Applying the variational principle leads to the Kohn-Sham Schrödinger-like equations:

$$(H_{\text{KS}} - \epsilon_i)\psi_i(\boldsymbol{r}) = 0, \tag{4.22}$$

where the ϵ_i are the eigenvalues and H_{KS} is the effective Hamiltonian

$$H_{\text{KS}}(\boldsymbol{r}) = -\frac{\hbar^2}{2m}\nabla^2 + V_{\text{KS}}(\boldsymbol{r}), \tag{4.23}$$

with

$$\begin{aligned} V_{\text{KS}}(\boldsymbol{r}) &= V_{\text{ext}}(\boldsymbol{r}) + \frac{\delta E_{\text{Hartree}}}{\delta n(\boldsymbol{r})} + \frac{\delta E_{\text{XC}}}{\delta n(\boldsymbol{r})} \\ &= V_{\text{ext}}(\boldsymbol{r}) + V_{\text{Hartree}}(\boldsymbol{r}) + V_{\text{XC}}(\boldsymbol{r}). \end{aligned} \tag{4.24}$$

If the exchange-correlation potential V_{XC} were known, these equations would lead to the exact ground state density and energy for the interacting system. The advantage of this approach is, that the remaining functional $E_{\text{XC}}[n]$ can be expressed as a local or nearly local functional of the density. The long range Hartree terms and the independent-particle kinetic energies are separated out. This means that the energy E_{XC} can be expressed in the form

$$E_{\text{XC}}[n] = \int d\boldsymbol{r}\, n(\boldsymbol{r})\epsilon_{\text{XC}}([n], \boldsymbol{r}), \tag{4.25}$$

where $\epsilon_{\text{XC}}([n], \boldsymbol{r})$ is an energy per electron at point $\boldsymbol{r}$ that depends only upon the density $n(\boldsymbol{r})$ in some neighborhood of point $\boldsymbol{r}$.

4.3.2 Functionals for exchange and correlation

The crucial quantity in the Kohn-Sham approach is the exchange-correlation energy, expressed as a functional of the density $E_{\mathrm{XC}}[n]$. There are different approaches on how to choose an appropriate functional, the two most popular being the local density approximation (LDA) and the generalized-gradient approximation (GGA). Recent developments in the field also use non-local formulations like orbital-dependent functionals.

Local density approximation

The idea for the LDA is very simple. It was already presented by Kohn and Sham in their original publication. Solids are often well described as a homogeneous electron gas. The exchange-correlation energy is then simply an integral over all space where the exchange-correlation energy density at each point is the same as in a homogeneous electron gas with that density,

$$E_{\mathrm{XC}}^{\mathrm{LDA}}[n] = \int d\boldsymbol{r}\, n(\boldsymbol{r}) \epsilon_{\mathrm{XC}}^{\mathrm{hom}}(n(\boldsymbol{r})). \tag{4.26}$$

Despite of this approximation the LDA yields reasonable results for a wide range of solids. It is implemented in most modern computer codes and has lead to improved functionals, like GGA.

Generalized-gradient approximation

A natural approach to improve the results of the LDA for inhomogeneous densities is the incorporation of the gradient. The "gradient expansion approximation" (GEA) was already proposed by Kohn and Sham in the original paper and realized by Herman *et al.* [52] in 1969. The form

$$E_{\mathrm{XC}}[n] = \int d\boldsymbol{r}\, n(\boldsymbol{r}) f_{\mathrm{XC}}(n(\boldsymbol{r}), \nabla n(\boldsymbol{r}), \nabla^2 n(\boldsymbol{r})) \tag{4.27}$$

however has some drawbacks. The first order derivatives often worsen the result, while second order terms may have divergences. The basic problem is that gradients in real materials are so large that the expansion breaks down.

To deal with these problems the generalized-gradient approximation (GGA) was developed. It splits the exchange-correlation energy density ϵ_{XC} into the local

exchange energy of the homogeneous gas and a dimensionless gradient-dependent part F_{XC},

$$E_{\mathrm{XC}}^{\mathrm{GGA}}[n] = \int d\boldsymbol{r}\, n(\boldsymbol{r})\epsilon_{\mathrm{XC}}(n(\boldsymbol{r}), \nabla n(\boldsymbol{r}), \ldots)$$
$$\equiv \int d\boldsymbol{r}\, n(\boldsymbol{r})\epsilon_{\mathrm{X}}^{\mathrm{hom}}(n) F_{\mathrm{XC}}(n(\boldsymbol{r}), \nabla n(\boldsymbol{r}), \ldots). \tag{4.28}$$

The functional form of the F_{XC} term is rather complicated. It is usually written as an expansion, for which the coefficients have to be determined from training data or from mathematical constraints. The most common parametrizations for the GGA are BLYP [11, 71], PW91 [95] and PBE [94].

Advanced and hybrid functionals

Besides the basic local density formulations LDA and GGA there also are some non-local approaches. That are the average density approach (ADA) and the weighted density approximation (WDA). The results with these functionals are superior in certain situations. A general comparison of local and non-local functionals has not yet been performed.

A common issue of the Kohn-Sham approach is that many materials with localized or strongly interacting electrons cause problems. Usually transition metal oxides as well as rare earth elements and compounds are difficult to deal with. Different methods have been developed to incorporate effects that are important in these systems. In particular the SIC and LDA+U approach are used.

SIC stands for "self-interaction corrections" and tries to correct for the unphysical self-interaction in many functionals for exchange and correlation E_{XC}. The LDA+U methods use the regular local density calculations LDA or GGA and couple it with an additional orbital-dependent interaction. Its purpose is to shift the localized orbits relative to the other orbits, to correct errors known to be large in usual LDA and GGA calculations.

Another class of functionals are called "hybrid" because they are a combination of orbital-dependent Hartree-Fock and an explicit density functional. For the accuracy of the energy these functionals provide the best results.

4.3.3 Pseudopotentials

One of the most expensive parts of electronic structure calculations is the treatment of the core electrons. These tightly bound electrons have a strongly localized wavefunction, which can vary on short distances. For numerical calculations that is very unfavorable. To reduce the efforts needed for the core electrons the concept of pseudopotentials was established. The idea is to replace the strong Coulomb potential of the nucleus and the effects of the tightly bound core electrons by an effective ionic potential that acts on the valence electrons.

Frozen core approximation

The motivation for the introduction of pseudopotentials is the frozen core approximation. It assumes that the core electrons do not participate in chemical bonding or other electronic properties. Only the valence electrons have an overlap with electrons from other atoms. The inner shells can thus be treated as frozen and their wavefunctions be calculated independently from the many-body system. This can be done either by replacing the inner shells with an effective potential, like for most pseudopotential methods, or by using pseudopotential operators but retaining the full core wavefunctions, like in the projector augmented wave (PAW) approach.

Formal justification for pseudopotentials

A short proof for the justification of pseudopotentials, which also gives some insight into their construction, shall be given here. It uses the ansatz

$$|\Psi\rangle = |\phi\rangle + \sum_n c_n |\chi_n\rangle, \tag{4.29}$$

where $|\Psi\rangle$ is the true wavefunction, $|\phi\rangle$ the pseudo wavefunction and $|\chi_n\rangle$ are the core wavefunctions. The core and the true wavefunctions need to be orthogonal, from which one can deduce

$$0 = \langle\chi_n|\Psi\rangle = \langle\chi_n|\phi\rangle + c_n \quad \Rightarrow \quad c_n = -\langle\chi_n|\phi\rangle, \tag{4.30}$$

$$\text{and} \quad |\Psi\rangle = |\psi\rangle - \sum_n \langle\chi_n|\phi\rangle|\chi_n\rangle. \tag{4.31}$$

The Schrödinger equation then yields

$$\hat{H}|\Psi\rangle = \hat{H}|\phi\rangle - \sum_n \underbrace{\hat{H}|\chi_n\rangle}_{E_n|\chi_n\rangle}\langle\chi_n|\phi\rangle = E|\Psi\rangle = E|\phi\rangle - E\sum_n |\chi_n\rangle\langle\chi_n|\phi\rangle. \tag{4.32}$$

Rearranging these terms leads to

$$\underbrace{\left\{\hat{H} + \sum_n (E - E_n)|\chi_n\rangle\langle\chi_n|\right\}}_{\text{pseudopotential Hamiltonian}} |\phi\rangle = E|\phi\rangle, \tag{4.33}$$

where E is the exact eigenvalue of the true wave function Ψ. Solving this equation in a self-consistent way, the pseudo wavefunction as well as the correct energy values can be obtained.

The basic idea of pseudopotentials is illustrated in Fig. 4.1. For distances smaller than a certain cutoff radius r_c the real potential is replaced by the pseudopotential V_{pseudo}. The real wavefunction, which has several knots in the core region, is then replaced by a pseudo wavefunction without any knots. For distances greater than r_c, the all electron wavefunction and the pseudo wavefunction are identical.

The important property, which must be conserved by the pseudopotential, is the phase shift $\delta_l(\epsilon)$. The index l stands for the angular momentum of the scattered wavefunction and ϵ for its energy. The scattering properties of a localized spherical potential can be formulated in terms of this phase shift. The scattering cross-section and all properties of the wavefunction outside the localized region are determined by it.

By choosing a potential with more desirable properties, which can reproduce the phase shift up to a modulo of $2\pi n$, the numerical effort can be reduced greatly. This does not change the properties of the wavefunctions outside of the scattering region, they are invariant for such phase shifts.

Different approaches for pseudopotentials

The first ideas on how to effectively describe electron scattering from electrons were published in the 1930s by Fermi and coworkers. A first application of pseudopotentials to solids was presented by Hellmann [50] in 1935. The orthogonalized plane waves (OPWs) method of Herring was the basis for the pseudopotential research

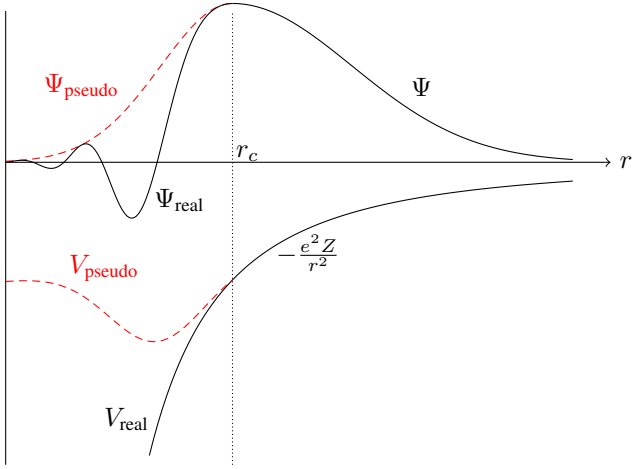

Figure 4.1: Schematic representation of pseudopotentials and the corresponding wavefunctions.

in the 1950s. It yielded accurate descriptions which led to the basic understanding of many properties of sp-bonded metals and semiconductors. In modern computer codes usually there are several different approaches to pseudopotentials available. They are briefly discussed in the next paragraphs.

Norm-conserving pseudopotentials (NC-PP) are the basis for most modern pseudopotential calculations. In 1979 HAMANN *et al.* published a list of requirements for a "good" pseudopotential [49]. It comprises the following points:

1. All-electron and pseudo valence eigenvalues agree for the chosen atomic reference configuration.
2. All-electron and pseudo valence wavefunctions agree beyond a chosen core radius r_c.
3. The logarithmic derivatives of the all-electron and pseudo wavefunctions agree at r_c.
4. The integrated charge inside r_c for each wavefunction agrees (norm-conservation).

The points 1 and 2 are already clear from the definition of pseudopotentials. Point 3 follows from the requirement of a smooth potential, the dimensionless logarithmic derivative D is defined as

$$D_l(\epsilon, r) \equiv r\psi_l'(\epsilon, r)/\psi_l(\epsilon, r) = r\frac{d}{dr}\ln\psi_l(\epsilon, r), \tag{4.34}$$

where ψ_l is either the all-electron or pseudo wavefunction.

Inside of the core radius r_c the integrated charge Q_l has to be the same for the all-electron (AE) and pseudo (PS) wavefunction,

$$Q_l = \int_0^{r_c} dr\, r^2 \left|\psi_l^{AE}\right|^2 = \int_0^{r_c} dr\, r^2 \left|\psi_l^{PS}\right|^2. \tag{4.35}$$

This conservation ensures that the total charge in the core region is correct and that the normalized pseudo-orbital is equal to the true orbital outside of r_c. For solids this means, that the pseudo-orbitals are correct between the atoms, in the region where the bonding occurs.

Ultrasoft pseudopotentials (US-PP) are another approach to reducing the computational efforts. Usually the goal of pseudopotentials is to have a function that is as "smooth" as possible and yet accurate. One reason for this is that smooth functions can be expressed with less Fourier components, which in turn require less computational time. Increasing the "smoothness" of a pseudopotential is equivalent to reducing the size of the Fourier space needed to describe the valence properties with a given accuracy. For norm-conserving pseudopotentials this accuracy is usually reached by sacrificing some of the "smoothness".

The ultrasoft pseudopotentials maintain the smoothness with a different approach. The wavefunction is split up into two parts, a smooth function and an auxiliary function that represents the rapidly varying part close to the core. In cases where most of the orbitals are tightly bound in the core region, US-PP can yield a huge speedup compared to norm-conserving pseudopotentials, while keeping the accuracy the same.

Projector augmented waves (PAW) are a general approach to the solution of the electronic structure problem with the help of modern computational methods. As the ultrasoft pseudopotentials it includes auxiliary localized functions. The full

wavefunction in all space can be written as

$$|\Psi\rangle = |\tilde{\Psi}\rangle + \sum_m \langle \tilde{p}_m | \tilde{\Psi} \rangle \left\{ |\Psi_m\rangle - |\tilde{\Psi}_m\rangle \right\}, \tag{4.36}$$

where $|\Psi\rangle$ and $|\tilde{\Psi}\rangle$ are the all-electron and the smooth wavefunctions, respectively. Both can be expanded into partial waves m in a sphere, $|\Psi\rangle = \sum_m c_m |\Psi_m\rangle = \sum_m \langle \tilde{p}_m | \tilde{\Psi} \rangle |\Psi_m\rangle$, which are the solution of the Schrödinger equation for an isolated atom. The projection operators $\tilde{p}$ are defined by $\langle \tilde{p}_m | \tilde{\Psi}_{m'} \rangle = \delta_{mm'}$.

With the PAW ansatz the full all-electron wavefunction is kept for the valence part while the smoothness is also incorporated in the core region. Especially for systems with both localized and delocalized valence states it can be beneficial. The PAW method combines the accuracy of all-electron methods with the efficiency of pseudopotentials. It is available in many commercial and free simulation packages.

4.4 Basis functions

For numerically calculating wave functions in a solid there are two approaches. Plane waves are favorable in a periodic system while grid methods are usually applied to finite systems. In modern computer codes both plane waves and grids are used together with the fast Fourier transformation.

To expand a wavefunction in an infinite system an infinitely large basis set is required. Using the Bloch theorem this problem can be solved. It states that in a periodic solid all wavefunctions can be written as a product of a plane wave and a lattice periodic function,

$$\psi_n(\boldsymbol{r}) = \exp(i\boldsymbol{k}\boldsymbol{r}) u_n(\boldsymbol{r}), \tag{4.37}$$

where

$$u_n(\boldsymbol{r} + \boldsymbol{l}) = u_n(\boldsymbol{r}). \tag{4.38}$$

The periodic function u_n is invariant under the translation of any lattice vector $\boldsymbol{l}$. It can be expanded into plane waves, using the reciprocal lattice vectors $\boldsymbol{G}$ as wave

vectors,

$$u_n(\boldsymbol{r}) = \sum_{\boldsymbol{G}} c_{n,\boldsymbol{G}} \exp(i\boldsymbol{G}\boldsymbol{r}), \tag{4.39}$$

$$\text{with} \quad \boldsymbol{G} \cdot \boldsymbol{l} = 2\pi m, \quad m \in \mathbb{Z}. \tag{4.40}$$

Therefore all electronic wave functions in a periodic solid can be written as sums of plane waves,

$$\psi_n(\boldsymbol{r}) = \sum_{\boldsymbol{G}} c_{n,\boldsymbol{k}+\boldsymbol{G}} \exp\left[i(\boldsymbol{k}+\boldsymbol{G})\boldsymbol{r}\right]. \tag{4.41}$$

The Bloch theorem changes the problem of calculating an infinite number of electronic wavefunctions to one of calculating a finite number of plane waves at an infinite number of $\boldsymbol{k}$ points. Electronic states, however, are only allowed at certain $\boldsymbol{k}$ points, determined by the boundary conditions. If the grid of these points is chosen densely, the real wavefunction will agree almost perfectly with the interpolated one. In this case the entire wavefunction can be represented by a discrete set of points in $\boldsymbol{k}$ space. Methods to efficiently choose these special points in the Brillouin zone were proposed, a popular one by Monkhorst and Pack [83].

The error originating from this $\boldsymbol{k}$ space sampling can always be reduced by using a denser set of $\boldsymbol{k}$ points. The computational cost of performing a densely sampled $\boldsymbol{k}$ space simulation can be significantly reduced with the $\boldsymbol{k} \cdot \boldsymbol{p}$ total-energy method of Robertson and Payne [99]. It uses a coarse grid of $\boldsymbol{k}$ points and the $\boldsymbol{k} \cdot \boldsymbol{p}$ perturbation theory to calculate the data for a dense grid.

4.4.1 Plane wave basis sets

Using Bloch's theorem the wavefunctions at each $\boldsymbol{k}$ point can be expanded into terms of a discrete plane wave set. This also requires an infinite set of plane waves. The coefficients $c_{n,\boldsymbol{k}+\boldsymbol{G}}$ of those waves with a large kinetic energy $(\hbar^2/2m)|\boldsymbol{k}+\boldsymbol{G}|^2$ are usually small and can be neglected. Only the plane waves up to a certain energy need to be considered, which leads to a limited number of plane wave basis functions.

Introducing this cutoff energy leads to an error in the computed total energy. The cutoff value should be increased until the calculated energy has converged. In practice there are methods to perform calculations at lower cutoff energies with only marginal errors.

When plane waves are used as a basis set, the Kohn-Sham equations assume a simple form. Substituting Eq. (4.41) into Eq. (4.22) and integrating over $\boldsymbol{r}$ yields the matrix equation

$$\sum_{\boldsymbol{G}'} H_{\boldsymbol{G},\boldsymbol{G}'} c_{n,\boldsymbol{k}+\boldsymbol{G}'} = \epsilon_n c_{n,\boldsymbol{k}+\boldsymbol{G}}, \tag{4.42}$$

where

$$H_{\boldsymbol{G},\boldsymbol{G}'} = \frac{\hbar^2}{2m}|\boldsymbol{k}+\boldsymbol{G}|^2 \delta_{\boldsymbol{G},\boldsymbol{G}'} + V_{\mathrm{KS}}(\boldsymbol{G}-\boldsymbol{G}'). \tag{4.43}$$

The kinetic energy is diagonal in this form, the potential is described as the Fourier transform. This matrix has to be solved for every $\boldsymbol{k}$ point with a diagonalization method. The size of the matrix is determined by the choice of the cutoff energy $(\hbar^2/2m)|\boldsymbol{k}+\boldsymbol{G}|^2$ for the plane wave basis, it can be significantly reduced by using pseudopotentials.

4.5 Physical properties from electronic structure calculations

Calculating physical properties from electronic structure simulations can be a costly problem. According to Newton's laws the basic equations of motion for a set of interacting nuclei are given by

$$M_I \ddot{\boldsymbol{R}}_I = -\frac{\partial E}{\partial \boldsymbol{R}_I} = \boldsymbol{F}_I[\{\boldsymbol{R}_J\}], \tag{4.44}$$

where $\{\boldsymbol{R}_I\}$ are the coordinates of the particles and $E[\{\boldsymbol{R}_I\}]$ is their interaction energy. These equations can be solved very efficiently with numerical algorithms (cf. Sec. 5.2). In electronic structure calculations the forces on the nuclei, however, also depend on the positions of the electrons.

To account for them, the Hellmann-Feynman theorem [41] can be used. It states the the force on a nucleus is given strictly in terms of the charge density and does not depend on the electron kinetic energy, exchange or correlation. From the general expression of the total energy, Eq. (4.12), with the assumption of $\langle\Psi|\Psi\rangle = 1$, one

can calculate the force as

$$\boldsymbol{F}_I = -\frac{\partial E}{\partial \boldsymbol{R}_I} = -\langle\Psi|\frac{\partial \hat{H}}{\partial \boldsymbol{R}_I}|\Psi\rangle - \langle\frac{\partial \Psi}{\partial \boldsymbol{R}_I}|\hat{H}|\Psi\rangle - \langle\Psi|\hat{H}|\frac{\partial \Psi}{\partial \boldsymbol{R}_I}\rangle - \frac{\partial E_{\text{II}}}{\partial \boldsymbol{R}_I}. \tag{4.45}$$

The middle two terms of the righthand side vanish for the fact that the exact ground state solution is extremal with respect to all possible variations. The term of Eq. (4.12) which depends on the position of the nuclei $\boldsymbol{R}_I$ is the only one that has to be accounted for:

$$\boldsymbol{F}_I = -\frac{\partial E}{\partial \boldsymbol{R}_I} = -\int d\boldsymbol{r}\, n(\boldsymbol{r}) \frac{\partial V_{\text{ext}}(\boldsymbol{r})}{\partial \boldsymbol{R}_I} - \frac{\partial E_{\text{II}}}{\partial \boldsymbol{R}_I}. \tag{4.46}$$

Here $n(\boldsymbol{r})$ is the unperturbed density and the nuclei are held fixed. It can be shown that the right hand side of Eq. (4.46) is equal to the nuclear charge times the electric field due to the electrons.

The force theorem can be generalized to calculate the derivative of the energy with respect to any parameter λ in the Hamiltonian. This is also done using the variational properties of the wavefunction. Additionally it can also be used to calculate finite energy differences between any two state connected by a continuous variation of the Hamiltonian. The general expression is given as

$$\frac{\partial E}{\partial \lambda} = \langle\Psi_\lambda|\frac{\partial \hat{H}}{\partial \lambda}|\Psi_\lambda\rangle \tag{4.47}$$

and

$$\Delta E = \int_{\lambda_1}^{\lambda_2} d\lambda \frac{\partial E}{\partial \lambda} = \int_{\lambda_1}^{\lambda_2} d\lambda \langle\Psi_\lambda|\frac{\partial \hat{H}}{\partial \lambda}|\Psi_\lambda\rangle. \tag{4.48}$$

Using the force-theorem the calculations of interatomic forces can be done very efficiently. This lead to the development of quantum molecular dynamics (QMD) simulations. In 1985 Car and Parrinello [23] introduced a new algorithm that unifies the two problems of the motion of the ions and of the electrons into a single problem. This Car-Parinello algorithm solves the quantum electronic problem using MD by adding a fictitious kinetic energy for the electronic states. Based on this approach many forms of QMD simulations were developed.

With the establishment of QMD simulations many dynamic properties of solids could be calculated with high accuracy. This includes diffusion and transport processes, mechanical properties as well as simple lattice dynamics.

4.6 VASP – The Vienna Ab initio Simulation Package

The Vienna Ab initio Simulation Package (VASP) is a widely used commercial computer code for electronic structure calculations and quantum-mechanical molecular dynamics, from first principles. It was created at the University of Vienna by Kresse and Hafner [64–67]. All *ab initio* calculations performed for this work were carried out with this program.

VASP is a plane wave DFT code which supports LDA, GGA and metaGGA for the exchange-correlation energies. Different pseudopotential approaches, like norm-conserving, ultrasoft or PAW potentials, can be used to solve the many-body Kohn-Sham equations selfconsistently. The employed algorithms for matrix diagonalization are highly optimized and work very efficiently even with small plane wave basis sets. Further increase in computational speed is gained by symmetry analysis which reduces the number of degrees of freedom as much as possible.

The capabilities of VASP were greatly extended in the latest releases. It can now perform Born-Oppenheimer molecular dynamics, structure relaxation as well as transition state searches like the nudged elastic band method. Several physical properties can be calculated directly by VASP without the need for external data analysis tools. This includes phonons as well as elastic properties.

With the VASP code it is possible to run molecular dynamics simulations with a few hundred atoms (≤ 500) on a ps timescale. This, however, requires several weeks of computation time on regular computers, the bigger problem is the memory requirement. Even for medium cutoff energies more than 50 GB may be necessary for such large systems.

A detailed review on the VASP package with comparisons to other, open-source DFT codes, can be found in [48].

Chapter 5:

Molecular dynamics simulations

A different approach to the simulation of solids is classical molecular dynamics (MD). Compared to *ab initio* methods, it can treat particle numbers several magnitudes larger in much shorter time. There obviously is a tradeoff, which for MD simulations is the accuracy. After the discussion of the algorithms and atomic interactions, the two different computer codes used in this work – IMD and LAMMPS – will be shortly introduced and compared.

5.1 Basic assumptions

In Chapter 4, the Hamiltonian for a system of N interacting atoms was given in Eq. (4.1). Applying the Born-Oppenheimer approximation is also possible in a different way. For *ab initio* simulations the positions of the nuclei are kept fixed and the electronic structure is calculated. Classical molecular dynamics uses the exactly opposite approach. The contributions of the electrons are put into an effective potential acting on the nuclei. This makes it possible to treat the atoms as simple point masses.

With the further assumption that the classical description is correct, the Hamiltonian $\mathcal{H}$ can be written as a sum of kinetic and potential energy functions

$$\mathcal{H}(\boldsymbol{q}, \boldsymbol{p}) = \mathcal{T}(\boldsymbol{p}) + \mathcal{V}(\boldsymbol{q}), \tag{5.1}$$

which depend on the generalized coordinates $\boldsymbol{q} = (\boldsymbol{q}_1, \ldots, \boldsymbol{q}_N)$ and momenta $\boldsymbol{p} = (\boldsymbol{p}_1, \ldots, \boldsymbol{p}_N)$ of each atom. For MD simulations of condensed matter the coordinates $\boldsymbol{q}_i$ can be replaced by the Cartesian coordinates $\boldsymbol{r}_i$ of the atoms.

The kinetic energy $\mathcal{T}$ usually is of the simple form

$$\mathcal{T} = \sum_{i=1}^{N} \frac{\boldsymbol{p}_i^2}{2m_i}, \tag{5.2}$$

with m_i being the mass of atom i.

The potential energy $\mathcal{V}$ contains all the information on the interactions of the particles. If $\mathcal{V}$ is well behaved, it is possible to obtain equations of motion from $\mathcal{H}$ which govern the time-evolution of the system. Generally these equations will be of Newtonian form, but Hamiltonian or Lagrangian form are also possible.

A common approach for the potential energy $\mathcal{V}$ is to write it as a sum of terms depending on the coordinates of single atoms, pairs of atoms, triplets of atoms, etc.:

$$\mathcal{V} = \sum_i V_1(\boldsymbol{r}_i) + \sum_{i<j} V_2(\boldsymbol{r}_i, \boldsymbol{r}_j) + \sum_{i<j<k} V_3(\boldsymbol{r}_i, \boldsymbol{r}_j, \boldsymbol{r}_k) + \dots . \tag{5.3}$$

The notation $i < j$ in the indices of the sums indicates summation over all pairs i and j without counting any pair twice. The first term V_1 represents an external potential, like gravity or boundary conditions, acting on the particles. The remaining terms represent particle interactions. The pair potential part, V_2, as a rule depends only on the magnitude of the pair separation $r_{ij} = |\boldsymbol{r}_j - \boldsymbol{r}_i|$ and can be written as $V_2(r_{ij})$. Many effective potentials include the pair contribution in this simple form. The triplet term, V_3, is becoming more popular with increasing computer power. It allows the calculation of directionally dependent forces, but computation costs scale with $\mathcal{O}(N^3)$. There are a few potentials which include this term, they are explained in section 5.3.2. Four-body and higher terms in (5.3) are generally assumed to be small compared to V_2 and V_3, so they are usually neglected.

This approximation for the potential energy has been used over the last decades with great success. In the days of the first computers, using only the simple two-body term V_2 allowed for simulations with very limited resources. The understanding of many properties and processes, provided by these calculations, was very useful and could not have been acquired easily by other means. New results, however, have indicated that this approximation is not appropriate for all systems and produces results inconsistent with many experiments due to the neglect of many-body interactions. Potentials that include the three-body term V_3 can give more precise predictions, especially for metals and semiconductors. But this comes at the cost of a more complex calculation scheme and a more difficult way of defining and

obtaining these multi-body interactions.

Comparing the molecular dynamics approach with *ab initio* simulations from chapter 4, there are some fundamental differences. The time and length scales that can be reached with MD calculations exceed *ab initio* simulations by at least two orders of magnitude. A sketch, comparing these scales, is shown in Fig. 5.1.

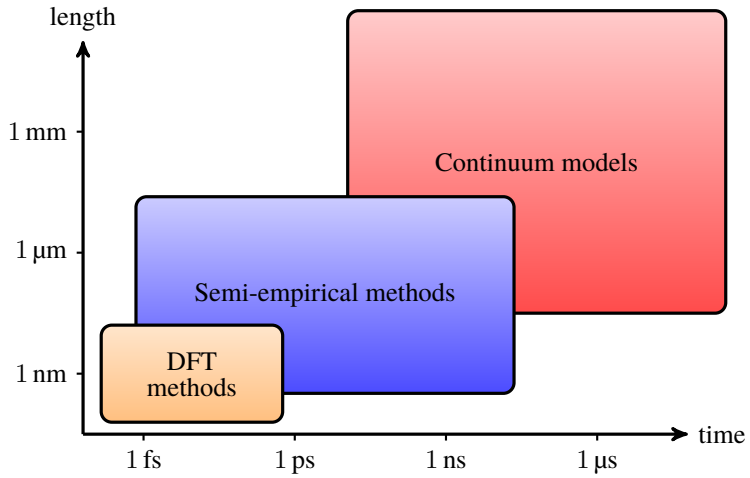

Figure 5.1: Time and length scales of different simulation methods. *Ab initio* methods typically can cover system sizes up to a few nanometers and simulation times up to a picosecond. The next group of simulation schemes are the semi-empirical methods, which rely on some kind of parametrization of the interactions. For even larger simulations, the atomistic representation of matter is replaced by a continuum. This is the basis for mesoscopic methods and finite element methods (FEM).

Ab initio simulations can typically handle up to a thousand atoms on short timescales. The semi-empirical methods, like MD calculations, can be used to study billions of atoms for a few nanoseconds. The trade-off for the increased system sizes and longer time scales is the precision of the simulations. The empirical potentials that are used to approximate the potential energy $\mathcal{V}$ can never be as accurate as calculations, which take the electronic structure into account. Another problem for most of the potentials used in MD simulations is the transferability. Theoretically the approximations for $\mathcal{V}$ should be valid for all possible scenarios. In

reality, effective potentials only have a limited application range, where the simulation results agree with experimental data. This can be special crystal structures or temperature and pressure ranges. The problem of transferability is discussed in more detail in Sec. 6.4.

5.2 Equations of motion

A fundamental part of every molecular dynamics simulation is the integration of the equations of motion. There are several ways to obtain them, e.g. using the Lagrange or Hamilton formalism known from classical mechanics. The most simple way is to use Newton's equations, which yield

$$m_i \ddot{\boldsymbol{r}}_i = \boldsymbol{F}_i = -\nabla_{\boldsymbol{r}_i} \mathcal{V}. \tag{5.4}$$

The force $\boldsymbol{F}_i$, acting on atom i, is given by the negative gradient of the potential energy $\mathcal{V}$ with respect to its position $\boldsymbol{r}_i$. The second order differential equation can be rephrased as two differential equations of first order:

$$\dot{\boldsymbol{r}}_i(t) = \boldsymbol{p}_i(t)/m_i \tag{5.5a}$$

$$\dot{\boldsymbol{p}}_i(t) = \boldsymbol{F}_i(\boldsymbol{r}_1, \ldots, \boldsymbol{r}_N) = -\nabla_{\boldsymbol{r}_i} \mathcal{V}(\boldsymbol{r}_1, \ldots, \boldsymbol{r}_N). \tag{5.5b}$$

The explicit dependencies are given in equations (5.5) – it is assumed that the potential energy $\mathcal{V}$ does not depend on the time and that the particles move without friction. This, however, is not always the case, e.g. Langevin dynamics explicitly includes a velocity term in (5.5b) to simulate Brownian motion.

To compute the trajectories of N particles, one has to solve either $3N$ second-order differential equations, Eq. (5.4), or an equivalent set of $6N$ first-order differential equations, Eq. (5.5). This problem is known as the classical initial value problem. If the initial positions $\boldsymbol{r}_i(t=0)$ and velocities $\boldsymbol{v}_i(t=0)$ are given, the set of first-order differential equations (5.5) can be used to calculate the time-evolution of the system. To do this numerically, the problem has to be discretized in time. The state of the system is then only defined at discrete time steps, equally spaced by a distance τ: $t = t_0, t_1, t_2, \ldots$, where $\tau = t_{n+1} - t_n$. In the following the short notation

$$\boldsymbol{r}(t) = (\boldsymbol{r}_1(t), \boldsymbol{r}_2(t), \ldots, \boldsymbol{r}_N(t))^{\mathrm{T}}$$

will be used. The equations of motion can then be written as

$$\dot{\boldsymbol{v}}(t) = \boldsymbol{a}(\boldsymbol{x}(t)) \tag{5.6a}$$
$$\dot{\boldsymbol{r}}(t) = \boldsymbol{v}(t), \tag{5.6b}$$

where $\boldsymbol{a}$ is the acceleration of the particles, defined as $\boldsymbol{a}_i = \boldsymbol{F}_i/m$.

Integration schemes

There are many different methods to solve the differential equations (5.6) numerically. Not all of them can be used in molecular dynamics simulations for different reasons. The two principal criteria by which the algorithms have to be chosen is speed and numerical accuracy. Simple methods, like the Euler and Euler-Cromer method, cannot be used because they do not conserve the total energy of a system. The very popular Runge-Kutta methods do conserve the energy, however, they need many function evaluations per step, which is not favorable for MD simulations. Most of the simulation codes for classical molecular dynamics use the Verlet algorithm or a slight modification called the leap frog method.

The Verlet method uses the centered 3-point formula for the second derivative to get

$$\begin{aligned} \ddot{\boldsymbol{x}}(t) &= \frac{\boldsymbol{x}(t+\tau) + \boldsymbol{x}(t-\tau) - 2\boldsymbol{x}(t)}{\tau^2} + \mathcal{O}(\tau^2) \\ \Rightarrow \boldsymbol{x}(t+\tau) &= 2\boldsymbol{x}(t) - \boldsymbol{x}(t-\tau) + \tau^2 \boldsymbol{a}(\boldsymbol{x}(t)) + \mathcal{O}(\tau^4). \end{aligned} \tag{5.7}$$

Using also the centered 3-point formula for the velocity,

$$\boldsymbol{v}(t) = \dot{\boldsymbol{r}}(t) = \frac{\boldsymbol{x}(t+\tau) - \boldsymbol{x}(t-\tau)}{2\tau} + \mathcal{O}(\tau^2), \tag{5.8}$$

the Verlet method can be derived as

$$\boldsymbol{x}(n+1) = 2\boldsymbol{x}(n) - \boldsymbol{x}(n-1) + \tau^2 \boldsymbol{a}(n) \tag{5.9a}$$
$$\boldsymbol{v}(n) = \frac{\boldsymbol{x}(n+1) - \boldsymbol{x}(n-1)}{2\tau}. \tag{5.9b}$$

This iteration scheme is not self-starting, to calculate $\boldsymbol{x}(1)$ the value of $\boldsymbol{x}(-1)$ is

required. A simple solution is to use

$$\boldsymbol{x}(-1) = \boldsymbol{x}(0) - \tau\boldsymbol{v}(0) + \frac{\tau^2}{2}\boldsymbol{a}(0) \tag{5.10}$$

which will reproduce the value of $\boldsymbol{v}(0)$, if put into equations (5.9).

This method has several advantages, which make it suitable for molecular dynamics simulations. The discretization error for the positions is of $\mathcal{O}(\tau^4)$, the method is time-reversible and has an upper bound for the error.

With a small modification, this method can be improved to yield better numerical performance and be less susceptible to round-off errors. For that purpose the velocities are not defined at the time-steps t_n, but at the half-steps at intermediate times:

$$\boldsymbol{v}(t_n + \frac{\tau}{2}) = \frac{\boldsymbol{x}(t_n + \tau) - \boldsymbol{x}(t_n)}{\tau} + \mathcal{O}(\tau^2). \tag{5.11}$$

Using the centered 3-point formula in the half steps, the velocity can be expressed as

$$\begin{aligned} \boldsymbol{a}(t_n) = \dot{\boldsymbol{v}}(t_n) &= \frac{\boldsymbol{v}(t_n + \frac{\tau}{2}) - \boldsymbol{v}(t_n - \frac{\tau}{2})}{\tau} + \mathcal{O}(\tau^2) \\ \Rightarrow \boldsymbol{v}(t_n + \frac{\tau}{2}) &= \boldsymbol{v}(t_n - \frac{\tau}{2}) + \tau\boldsymbol{a}(t_n) + \mathcal{O}(\tau^3) \end{aligned} \tag{5.12}$$

From the definition in equation (5.11) $\boldsymbol{x}(n) - \boldsymbol{x}(n-1) = \tau\boldsymbol{v}(n - \frac{1}{2})$, which can be substituted into (5.9a):

$$\begin{aligned} \boldsymbol{x}(n+1) &= \boldsymbol{x}(n) + \tau\boldsymbol{v}(n - \frac{1}{2}) + \tau^2\boldsymbol{a}(n) \\ &= \boldsymbol{x}(n) + \tau\boldsymbol{v}(n + \frac{1}{2}). \end{aligned} \tag{5.13}$$

The leap frog scheme is thus

$$\boldsymbol{v}(n + \frac{1}{2}) = \boldsymbol{v}(n - \frac{1}{2}) + \tau\boldsymbol{a}(n) \tag{5.14a}$$

$$\boldsymbol{x}(n+1) = \boldsymbol{x}(n) + \tau\boldsymbol{v}(n + \frac{1}{2}). \tag{5.14b}$$

To the start the iteration, a similar formula like (5.10) can be used:

$$\boldsymbol{v}(-\frac{1}{2}) = \boldsymbol{v}(0) - \frac{1}{2}\tau\boldsymbol{a}(0). \tag{5.15}$$

The main advantage of this leap frog algorithm is that is suffers less from round-off errors, as no τ^2 term appears in (5.14a) when compared to (5.9a). This is important because the time step in MD simulations may become small. Therefore, it is the method of choice for running molecular dynamics simulations.

Thermodynamical ensembles

By using the leap frog scheme with no additional constraints, the simulations are carried out in the microcanonical ensemble. The number of particles N, the volume V of the system and the total energy E of the system are conserved. In experimental situations this may not be the case, often the temperature is kept fixed and the energy is changing. There are also situations where changing the volume is necessary while keeping the pressure fixed. To reflect these constraints in MD simulations, the integration schemes given in the previous subsection have to be adjusted. In this subsection the most popular methods for simulating a constant volume, constant temperature (NVT) and constant pressure, constant temperature ensemble (NPT) will be briefly outlined.

To keep the temperature of a system constant, a heat bath much larger than the system is used. The latter has a well-defined temperature and the smaller system has no influence on the heat bath. Microscopically the heat is exchanged by collisions of the particles with the wall that separates the system from the heat bath.

The temperature of a finite system is generally defined in the same way as for infinite systems, it is proportional to the average of the kinetic energy per degree of freedom. To impose a temperature on a system, rescaling the kinetic energies of the particles is the most simple way. By rescaling the momenta $\boldsymbol{p}_i$ of the particles with

$$\boldsymbol{p}_i \to \boldsymbol{p}_i \sqrt{\frac{3/2(N-1)k_{\mathrm{B}}T}{E_{\mathrm{kin}}}} \tag{5.16}$$

after each integration step, a system can be forced to a certain temperature. As it turned out [89], this velocity rescaling induces deviations from the canonical distribution and should therefore not be used.

The Nosé-Hoover thermostat for simulating a NVT ensemble tries to introduce the coupling to a heat bath via an external force acting on the particles. The equation of motion (5.4) then depends explicitly on the velocities of the particles:

$$m_i \ddot{\boldsymbol{r}}_i = \boldsymbol{F}_i(\boldsymbol{r}) - \zeta(\boldsymbol{r}, \dot{\boldsymbol{r}}) \dot{\boldsymbol{r}}_i. \tag{5.17}$$

Adding a friction term is the most direct way of affecting the kinetic energy of the particles. The friction coefficient ζ can be determined from the differential equation:

$$\frac{\mathrm{d}\zeta}{\mathrm{d}t} = \left(\sum_i \boldsymbol{v}_i^2 - 3Nk_\mathrm{B}T_\mathrm{D} \right) \Big/ Q, \tag{5.18}$$

where Q is a parameter that determines the strength of the coupling to the heat bath and T_D is the desired temperature. This equation can be derived from the equations of motion for a modified Hamiltonian, where the heat bath is explicitly introduced into the system in the form of a single degree of freedom s. The Hamiltonian of the total system is given as

$$\mathcal{H}(\boldsymbol{q}, \boldsymbol{p}, s, p_s) = \sum_i \frac{\boldsymbol{p}^2}{2m_i s^2} + \sum_{i<j} \mathcal{V}(\boldsymbol{q}) + \frac{p_s^2}{2Q} + g k_\mathrm{B} T \ln(s). \tag{5.19}$$

g is the number of independent momentum-degrees of freedom of the system and p_s the canonical conjugate momentum of s. The derivation of the equations of motions is shown in Thijssen [115].

A method to run simulations with constant temperature and constant pressure was first presented by Andersen [5]. The basic idea is to incorporate the volume into the equations of motion while scaling the spatial coordinates back to a unit volume:

$$\boldsymbol{r}_i' = \boldsymbol{r}_i V^{1/3}, \tag{5.20}$$

where the prime denotes the real coordinate. This is also done for the momenta,

$$\boldsymbol{p}_i' = \boldsymbol{p}_i / (s V^{1/3}). \tag{5.21}$$

The Hamiltonian (5.19) is extended by the volume V and the canonical momentum p_V. This can be thought of as the momentum of a piston closing the system. The

two extra terms in the Hamiltonian are the 'potential energy' PV and the 'kinetic energy' $p_v^2/2W$, where P is the pressure and W another parameter like Q.

$$\mathcal{H}(\boldsymbol{q},\boldsymbol{p},s,p_s,V,p_V) = \sum_i \frac{\boldsymbol{p}_i^2}{2m_i V^{2/3} s^2} + \sum_{i<j} \mathcal{V}(V^{1/3}\boldsymbol{q}) + \frac{p_s^2}{2Q} + g k_\mathrm{B} T \ln(s) + PV + \frac{p_V^2}{2W}. \tag{5.22}$$

The corresponding equations of motion are also given in Thijssen [115].

Performing simulations in the NPT ensemble is not a trivial task. Tuning the two free coupling parameters Q and W to the proper values can be very difficult. There exist formulas for crude estimates of these properties, the temperature and pressure, however, have to be monitored during the simulation. If the fluctuations become too large, the parameters Q or W have to be adjusted and the simulation has to be restarted.

5.3 Interatomic potentials

In Sec. 5.1 the potential energy $\mathcal{V}$ of a system of interacting particles is given as

$$\mathcal{V} = \sum_i V_1(\boldsymbol{r}_i) + \sum_{i<j} V_2(\boldsymbol{r}_i,\boldsymbol{r}_j) + \sum_{i<j<k} V_3(\boldsymbol{r}_i,\boldsymbol{r}_j,\boldsymbol{r}_k) + \ldots. \tag{5.3}$$

For running molecular dynamics simulations, an appropriate form of this potential energy has to be chosen. Over the last decades many different approaches have been proposed, which, however, are often limited in their range of applicability. A criterion to classify them is by the number of directly interacting particles. Potentials that only use V_2 and neglect any higher term contributions are called pair interactions. The most common forms are discussed in Sec. 5.3.1. If the term V_3 is used in the potential form, they are referred to as three- or many-body interactions. While theoretically there are potentials which use the V_4 term, in practice this is very unfeasible for mainly two reasons. It is very expensive to calculate four-body interactions and also very difficult to obtain them. Many-body potentials are the topic of Sec. 5.3.2.

Tricks of the trade

To speed up molecular dynamics calculations, some clever methods can be used. An important aspect is the size of the simulation box. On one hand it should be as small as possible to keep the computational cost at a minimum. On the other hand it has to be big enough to correctly reproduce the physical processes and allow for reasonable statistical averages. The influence of the system size is discussed in chapter 9 for the calculation of the thermal conductivity.

For the simulation of bulk properties, a system with periodic boundary conditions (PBC) can be used. This reduces the computational load greatly because supercells with the dimension of a few unit cells per side are enough for reliable simulations. To use periodic boundary conditions, the simulation program has to create periodic images for each surface and edge of the simulation box. In two dimensions these are eight and in three dimensions 28. Particles that leave the simulation box on one side are mapped back into the box on the opposite side. For 2D this is illustrated in Fig. 5.2.

Using PBC effectively removes surfaces and allows for the calculation of an infinite bulk system. It is also possible to apply other boundary conditions like rigid boundaries, where atoms are fixed in space, or open boundaries. Often several of these technique are combined to run simulations which are periodic in two directions and open in the third. An example is the simulation of laser ablation, where the system is open in the propagation direction of the laser and periodic in the other directions.

In metallic systems the range of the interatomic forces is usually limited to a few angstroms. This fact can be used to effectively reduce the computational cost of the force calculations. The potential function only has to be calculated up to a certain distance, all atoms further away do not contribute. This distance is called the cutoff radius r_c, which usually lies in the range of 4 to 8 Å.

Another way of reducing the computation time is the implementation of neighbor lists. To calculate the energy or force for atom i, a loop over all atoms j has to be performed. Usually a large percentage of the atoms j is at a distance much larger than the cutoff radius r_c, thus they do not interact with atom i. By generating a list, which contains only atoms that are closer than $\alpha \cdot r_c$, the loop over all atoms can be avoided. The parameter α has to be greater than 1, to include atoms that may leave or enter an atom's interaction radius. This neighbor list has to be updated on average every 10 to 20 steps, there are sophisticated algorithms for an automatic update scheme which are more efficient than a regular update after a fixed number of timesteps.

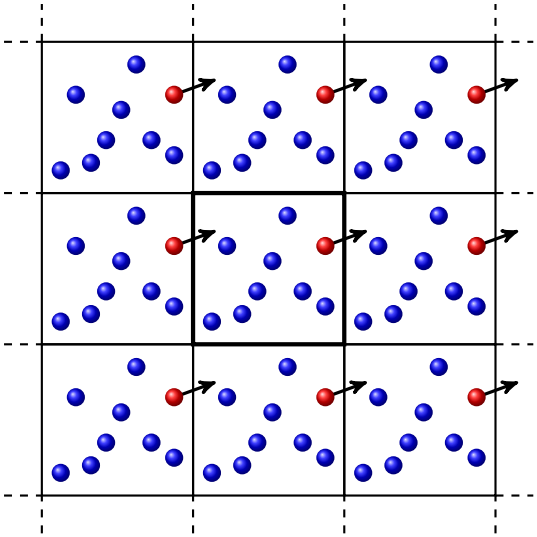

Figure 5.2: Schematic representation of periodic boundary conditions in two dimensions. The main simulation box is in the center with bold lines. If the red atom leaves this box to the right, its periodic image from the left enters the box.

The bottleneck of neighbor lists is the update process. It requires two nested loops over all atoms. To avoid this, the simulation box can be split up into smaller regions, so called cells. These cells ideally should be only slightly larger than the cutoff radius for the system. Then only atoms from the same or the neighboring cells need to be considered for the interactions. To update the neighbor list for a single atom, only the host cell of the atom as well as the neighbor cells have to be processed. The algorithm is well suited for parallelization and scales very good with the number of atoms. More details on these topics can be found in the book of Allen and Tildesley [3].

A very recent development to speed up different kinds of computer simulations is the use of graphics processors. It turned out, that the highly specialized graphics processing units (GPU), primarily developed for computer games, can be used in a very general way to run numerical simulations. This “General-purpose computing on graphics processing units” (GPGPU) is very fast compared with a traditional

computer processor, because a GPU is built to run many calculations in parallel. With an efficient parallelization scheme an MD simulation can be speed up by a factor of 100, compared to a single processor calculation. Porting an existing MD code like IMD to graphics processors is not a trivial task. There are some restrictions regarding the memory and data transfer which have to be circumvented with special techniques. In this work no GPGPU has been used, since the many-body interactions of IMD have not been adapted for the use with graphics processors yet.

5.3.1 Pair interactions

The most simple potentials that can be derived from Eq. (5.3) are pair interactions. They are assumed to be isotropic, i.e. they only depend on the pair distance $r_{ij} = |\boldsymbol{r}_j - \boldsymbol{r}_i|$ of the two atoms i and j. The potential energy for a system described by pair interactions is given as

$$\mathcal{V} = \sum_{i<j} V_2(\boldsymbol{r}_i, \boldsymbol{r}_j) = \sum_{i<j} V_2(r_{ij}) \tag{5.23}$$

and the force $\boldsymbol{F}_i$ acting on atom i as

$$\boldsymbol{F}_i = -\sum_{i<j} \nabla_i V_2(r_{ij}). \tag{5.24}$$

The potential energy V_2 can be expressed in different ways. The review paper of Vitek [119] gives an overview of pair potentials used for metal research. The most important ones will be discussed in the following paragraphs.

Pair potentials

In the early days of MD simulations, when computer power was very limited, the potentials had to be very simple. The function V_2 was chosen as a single function $\phi(r_{ij})$. In systems with more than one type of atoms, the different potentials are labeled $\phi_{s_i s_j}$, where s_i denotes the species of atom i. The s in the index of the potential function ϕ is usually omitted for reasons of simplicity – is is written ϕ_{ij}.

The force $\boldsymbol{F}_i$ can then be calculated as

$$\boldsymbol{F}_i = -\sum_{i<j} \nabla_{\boldsymbol{r}_i} \phi_{ij}(r_{ij}) = -\sum_{i<j} \frac{\partial \phi_{ij}}{\partial r_{ij}} \frac{\boldsymbol{r}_{ij}}{r_{ij}}. \tag{5.25}$$

The gradient $\nabla_{\boldsymbol{r}_i}$ acts on $\boldsymbol{r}_i$, it can be written as $\nabla_{\boldsymbol{r}_{ij}}$. To do this for all atoms in an MD simulation, a single loop over all pairs of atoms is enough. Using neighbor lists and exploiting Newton's third law the calculation can be performed very efficiently.

Despite their very simple form pair potentials provide very accurate results for some classes of materials. The famous Lennard-Jones potential [73] is often used for noble gases while the Morse potential [84] can accurately describe the bonding of diatomic molecules. Both potentials have an repulsive part due to the Pauli principle and an attractive part for the van der Waals force. The functional forms of all of the potentials mentioned are given in Sec. 6.6.3 and on the *potfit* homepage.

There are limitations to pair potentials which arise from the missing manybody terms. Prominent examples are the Cauchy discrepancy and the "cohesive energy-vacancy formation energy"-dilemma [90].

EAM potentials

There are several attempts to model many-body interactions with effective potentials. Most of them rely on the term V_3 from (5.3). They are discussed in Sec. 5.3.2. By using many-body pair-function potentials it is possible to implicitly include these effects without the term V_3. A term which accounts for the environment of the atoms has to be added to the previously introduced pair potentials. These interactions are commonly known as embedded atom method (EAM) potentials. It was introduced by Daw and Baskes [30], however the potential of Finnis and Sinclair [42] and the glue model of Ercolessi *et al.* [38] use a very similar approach, they only differ in the physical interpretation of the additional term.

All of these models are inspired by density functional theory. The basic idea is, that the cohesive energy of an atom is determined by the electron density of the neighboring atoms. This concept was presented by Stott and Zaremba [109] in a quasiatom model, which calculates the embedding energy of an impurity atom as a function of the electron density without the respective atom. For the embedded atom method the electron density is calculated as a linear superposition of the single atom electron densities.

The total energy for an EAM potential is given by

$$\mathcal{V} = \sum_{i<j} \phi_{ij}(r_{ij}) + \sum_i U_i(n_i), \tag{5.26}$$

$$\text{where} \qquad n_i = \sum_{j \neq i} \rho_j(r_{ij}). \tag{5.27}$$

When compared to pair potentials, the term V_2 of Eq. (5.3) is no longer a simple function. It consists of the regular pair term ϕ_{ij} and the embedding energy U_i of atom i in the host density n_i. For each atom the density n_i (5.27) is calculated as a sum over all neighboring atoms, with ρ_j being the transfer function of atom j. It does not represent an actual physical density; n_i is a purely empirical quantity. A mathematically correct derivation of the EAM model from density functional theory is given in [29].

Applying (5.4) to calculate the force $\boldsymbol{F}_i$, acting on atom i, yields

$$\boldsymbol{F}_i = \phi'_{ij}(r_{ij}) \frac{\boldsymbol{r}_{ij}}{r_{ij}} + \left[U'_i(n_i)\rho'_j(r_{ij}) + U'_j(n_j)\rho'_i(r_{ij}) \right] \frac{\boldsymbol{r}_{ij}}{r_{ij}}, \tag{5.28}$$

where the prime signifies the derivative with respect to the distance r_{ij}. To calculate the forces in an MD simulation a single loop over all atoms pair is no longer enough. The force depends on the derivative of the embedding function of atom j. A first loop which calculates all energies and densities and a subsequent second loop to calculate the forces are therefore required. When compared to pair potentials, EAM potentials are slower by a factor two. This, however, is acceptable, because they can be applied to a wider range of materials and often yield more accurate results.

The shortcomings of pair potentials described earlier do not apply to EAM potentials.

ADP potentials

Another approach for a simple model of many-body interactions was presented by Mishin *et al.* in 2005 [82]. It is based on the embedded atom method but has an additional bond-angle dependence. The model is called "Angular-Dependent Potential" (ADP) method. In an orthogonal Cartesian system the potential energy

is approximated by

$$\mathcal{V} = \sum_{i<j} \phi_{ij}(r_{ij}) + \sum_i U_i(n_i) + \frac{1}{2}\sum_{i,\alpha}(\mu_i^\alpha)^2 + \frac{1}{2}\sum_{i,\alpha,\beta}(\lambda_i^{\alpha\beta})^2 - \frac{1}{6}\sum_i \nu_i^2. \tag{5.29}$$

The indices i and j run over all atoms and the superscripts $\alpha, \beta = 1, 2, 3$ refer to the Cartesian directions x, y and z. ϕ and U are the pair potential and embedding function respectively, defined in the same way as for EAM potentials (cf. Eq. (5.26)). The empirical host electron density n is the superposition of the single particle densities ρ:

$$n_i = \sum_{j\neq i} \rho_j(r_{ij}) \tag{5.27}$$

The terms three to five in Eq. (5.29) are responsible for the indirect directional dependence of the potential. The vectors

$$\mu_i^\alpha = \sum_{j\neq i} u_{ij}(r_{ij}) r_{ij}^\alpha \tag{5.30}$$

and tensors

$$\lambda_i^{\alpha\beta} = \sum_{j\neq i} w_{ij}(r_{ij}) r_{ij}^\alpha r_{ij}^\beta \tag{5.31}$$

are functions of two additional pairwise potentials $u(r)$ and $w(r)$, which should, like ϕ, be written as $u_{s_i s_j}$ and $w_{s_i s_j}$. The quantities ν_i are traces of the λ-tensor:

$$\nu_i = \sum_\alpha \lambda_i^{\alpha\alpha}. \tag{5.32}$$

Angular-dependent potentials can be thought of as a kind of multipole expansion. μ_i and λ_i are measures of the dipole and quadrupole distortion of the local environment of atom i. In the original publication the role of these terms is to penalize the total energy for deviations from cubic symmetry. By fitting these potential models to *ab initio* reference data, these terms no longer penalize but contribute regularly to the total energy.

The total energy can formally also be derived from the MEAM formalism, which

is introduced in Sec. 5.3.2. In MEAM, the angular dependence is introduced through dipole and higher-order multipoles, similar to ADP. The difference is, that in an MEAM potential these contributions make up a tensor electron density and in ADP they contribute directly to the total energy (Equation (5.29)).

The ADP force $\boldsymbol{F}_i$, calculated with (5.4) from Eq. (5.29) consists of two parts:

$$\boldsymbol{F}_i = \sum_{j \neq i} \left[\varphi_{ij} + \psi_{ij} \right]. \tag{5.33}$$

φ is the same expression as for the EAM force (Eq. (5.28)) and ψ is the contribution of the angular-dependent forces. As before, the prime signifies differentiation with respect to the interatomic distance r_{ij}.

$$\begin{aligned} \psi_{ij}^{\gamma} = & \left(\mu_i^{\gamma} - \mu_j^{\gamma}\right) u_{ij}(r_{ij}) + \sum_{\alpha} \left(\mu_i^{\alpha} - \mu_j^{\alpha}\right) u'_{ij}(r_{ij}) \frac{r_{ij}^{\gamma} r_{ij}^{\alpha}}{r_{ij}} \\ & + 2 \sum_{\alpha} \left(\lambda_i^{\alpha\gamma} + \lambda_j^{\alpha\gamma}\right) w_{ij}(r_{ij}) r_{ij}^{\alpha} + \sum_{\alpha,\beta} \left(\lambda_i^{\alpha\beta} + \lambda_j^{\alpha\beta}\right) w'_{ij}(r_{ij}) \frac{r_{ij}^{\alpha} r_{ij}^{\beta} r_{ij}^{\gamma}}{r_{ij}} \\ & + \frac{1}{3} \left(\nu_i + \nu_j\right) \left[w'_{ij}(r_{ij}) r_{ij} + 2 w_{ij}(r_{ij}) \right] r_{ij}^{\gamma} \end{aligned} \tag{5.34}$$

To calculate ADP energy and forces only takes about twice as long as for EAM potentials. This is another advantage over MEAM potentials.

5.3.2 Many-body interactions

For pair interactions the expansion of the total energy (Eq. (5.3)) is truncated after the pair term V_2. Developments in the last decades, however, made it feasible to include the three-body term V_3 as well. The computational time required for such interactions is increased, because not only two but three nested loops over all atoms have to be performed. An overview of empirical many-body potentials is given in Erkoç [39]. The three most popular potentials will briefly be introduced in the next paragraphs.

MEAM potentials

In 1987, Baskes proposed an extension of the embedded atom method to account for the directionality of interatomic bonding [10]. The total potential energy of the modified embedded atom method (MEAM) potential was initially only defined for a monoatomic system. It is given as

$$\mathcal{V} = \sum_{i<j} \phi_{ij}(r_{ij}) + \sum_i U_i(n_i), \tag{5.35}$$

$$\text{with} \qquad n_i = \sum_{j\neq i} \rho(r_{ij}) - a \sum_{\substack{j\neq i \\ k\neq i}} (1 - \cos^2 \theta_{jik}) \rho(r_{ij}) \rho(r_{ik}), \tag{5.36}$$

where θ_{jik} is the angle between atoms j, i and k. Meanwhile the model has been extended for binary and ternary systems and there are many parametrizations available for different metallic systems. A simplified version has been published by Lenosky *et al.* [74], which is also available in *potfit*.

The addition of the three-body terms makes the calculation of energy and forces slower about a factor of three to five, when compared to EAM potentials.

Tersoff potentials

To model covalent bonds, Tersoff introduced an empirical potential which incorporates the bond order in an intuitive way [112]. There were several problems with the first model, which were corrected in a subsequent paper [113]. The potential energy has a rather complex form and contains 13 adjustable parameters.

There is a fundamental difference between the Tersoff potential and the other potentials previously discussed. For models like EAM or ADP only the expression for the total energy is given but not the specific form of the functions like the pair function ϕ. The Tersoff potential already gives specific functions and only requires the parameters to be adjusted for any new potential. On the one hand that makes the fitting of a new potential rather straightforward, on the other hand the potential model can never be as flexible as the EAM or ADP potentials.

Stillinger-Weber potentials

Another potential, that has predefined potential functions and only requires the parameters, is the Stillinger-Weber potential [107]. Like the Tersoff potential, it is designed to model silicon systems with two- and three-body contributions. The

original potential energy is given in [107]. A slightly optimized version, as it is implemented in the LAMMPS code, has 9 free parameters. Like the Tersoff potential, the Stillinger-Weber model uses predefined potential functions.

The main application for Stillinger-Weber potentials are silicon and other materials which crystallize in the diamond structure. A tetrahedral configuration is inherently embedded in the functional form. For surface or interface simulations the potential yields wrong results, as for the case of an external pressure. Due to the three-body contributions the computational effort is high, a short comparison with ADP and Tersoff potentials is given in Sec. 9.5.

5.4 Lattice dynamics

To explain most thermodynamic properties like heat capacities or phase stability, the motions of the atoms have to be taken into account. For example, the stable phase of any material is determined by the minimum of the free energy G, defined by

$$G = H - TS, \tag{5.37}$$

where H is the enthalpy and S the entropy. The primary source for the entropy are thermal vibrations of the atoms. Neglecting the dynamics is thus equivalent to zero temperature, which also means zero entropy.

In lattice dynamics the energy of a system is expressed as a Taylor expansion

$$\begin{aligned} E = E_0 &+ \frac{1}{2} \sum_{\substack{j,j' \\ \alpha,\alpha'}} \frac{\partial^2 E}{\partial u_{\alpha,j} \partial u_{\alpha',j'}} u_{\alpha,j} u_{\alpha',j'} + \dots \\ &+ \frac{1}{n!} \sum_{\substack{j^{(1)},\dots,j^{(n)} \\ \alpha^{(1)},\dots,\alpha^{(n)}}} \frac{\partial^n E}{\partial u_{\alpha^{(1)},j^{(1)}} \cdots \partial u_{\alpha^{(n)},j^{(n)}}} u_{\alpha^{(1)},j^{(1)}} \cdots u_{\alpha^{(n)},j^{(n)}} \\ &+ \dots, \end{aligned} \tag{5.38}$$

where E_0 is the equilibrium lattice energy and $u_{j,\alpha}$ describes a component of the vector displacement ($\alpha = x, y, z$) of the atom labeled j from its equilibrium position. The first order term in the expansion vanishes, because the residual forces for the equilibrium positions vanish by definition. The second order term is the

harmonic energy, all higher-order terms are grouped together as the anharmonic energy.

To keep the equations as simple as possible, the harmonic approximation is usually applied. There all anharmonic terms are neglected, which leads to a mathematical model for the lattice vibrations that has exact solutions. The accuracy of this approach is rather good. Many of the features of lattice dynamics are available, such as the dependence of frequency on the wave vector. The corrections of the higher-order terms can be introduced easily into the harmonic model, as long as the atomic displacements are small, which is usually the case.

In DFT calculations the harmonic approximation is used, the derivatives in Eq. (5.38) can be calculated from static simulations. With these data it is possible to calculate the dynamical matrix, from which phonon properties can be deduced (cf. Sec. 7.1).

One advantage of MD simulations is that the dynamic properties can be calculated from the trajectories of the atoms. Anharmonic contributions are implicitly included, as long as they are present in the effective potentials.

5.4.1 Anharmonic contributions

While the harmonic approximation can explain certain phenomena, e.g. the propagation of sound waves or the interaction of radiation with crystalline matter, there are also deficiencies. It is not possible to explain the finite lifetime of phonons, the thermal expansion, the thermal conductivity and the temperature dependence of phonons. All of these processes require the additional anharmonic terms in Eq. (5.38), which account for interaction of three or more phonons.

In the framework of the second quantization it can be shown, that the anharmonic terms have a physical interpretation in terms of collisions between phonons that lead to changes in their frequencies and wave vectors. Even creation and annihilation of phonons is described by them. The possible anharmonic three- and four-phonon interactions are shown in Fig. 5.3. Due to the addition or subtraction of a reciprocal lattice vector $\boldsymbol{G}$, the flow of energy can be changed, even reversed, by the anharmonic interactions (cf. Sec. 3.3.1).

Thermal conductivity

The anharmonic terms are of special importance for the thermal conductivity in a crystal lattice. In the harmonic approximation the phonons will transport the heat from one end of the sample to the other without any impairment. There is

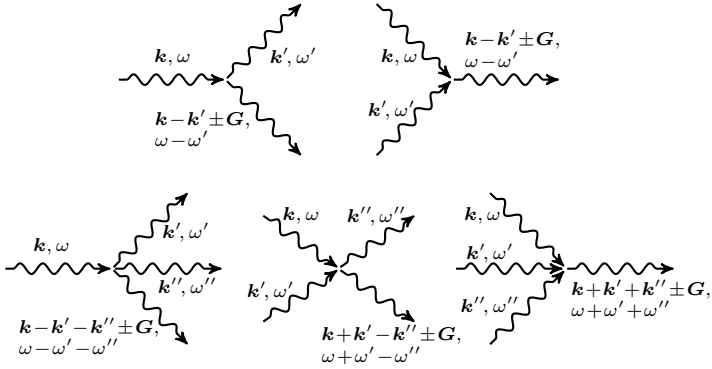

Figure 5.3: Third and fourth-order anharmonic phonon interactions with conservation restrictions. Phonons are represented by waves with arrows. Adapted from [33].

nothing in the harmonic model that inhibits the flow of phonons, the lattice thermal conductivity would be infinite. It is known from experiment, that the thermal conductivity decreases with increasing temperature, which implies that the phonons must be inhibiting the flow of heat.

In MD simulations the anharmonic effects are included implicitly via the effective potential. If the physical properties like the phonon density of states or the thermal conductivity are deduced from the trajectories of the particles, the anharmonic contributions can be accounted for. In DFT simulations, where the dynamical matrix approach is used, only the harmonic interactions can be calculated.

5.5 MD simulation packages

Mainly for two facts, the number of available molecular dynamics simulation packages is incredibly large. First, a simple MD code can be implemented rather quickly. Secondly, not all available packages support all features. There often are different fields of applications, e.g. there are codes that specialize in soft matter or liquids, while others can only handle periodic crystal structures or special interactions.

For this work the IMD package was used for most simulations. The LAMMPS code has been used to verify the results with a different implementation.

IMD – ITAP Molecular Dynamics

The development of the ITAP molecular dynamics code, called IMD, was started in 1995. It was publicly announced in 1997 by STADLER *et al.* [106]. IMD was designed for running short range molecular dynamics simulations on massively parallel computers. Over the course of time, many people have contributed to the code and extended IMD by various features. Because of the focus on efficient parallelization, it can be used on simple desktop computers as well as on state of the art supercomputers. IMD was the holder of the world record for the simulation with the most particles – in 1997 with 1.2×10^9 atoms and in 1999 even with 5.1×10^9 atoms.

Funding for the projects which contributed to the development were provided by the Deutsche Forschungsgemeinschaft (DFG) through two Collaborative Research Centers (SFB) 382 and 716. More information can be found in the IMD homepage[1].

Since the first version of IMD, more effective potentials and different simulation features were added. Today, IMD supports the most common short range potentials like EAM, ADP, Tersoff and Stillinger-Weber as well as long-range coulomb interactions. It is possible to run simulations in different thermodynamical ensembles like NVE, NVT and NPT or with relaxation algorithms. Other features are deforming a sample during the simulation, applying extra forces to specific atoms, constraining the movement of certain atoms and calculating correlation functions. The applications for these features are very diverse. The main research topics at the ITAP, using IMD, are crack propagation and shock wave simulation, laser ablation, structure optimization and lattice dynamics. In this work, IMD is used to calculate dynamic properties of complex metallic alloys like phonon spectra and the thermal conductivity.

The development of *potfit*, the ITAP force-matching code, is closely coupled to IMD. Early versions were part of the IMD code, later it was split into a separate package. The close relationship can still be seen as the *potfit* force routines were adopted directly from IMD with only little adjustment. After *potfit* has completed an optimization run, potentials in IMD format are written and can directly be used in MD simulations.

[1] http://imd.itap.physik.uni-stuttgart.de/

LAMMPS – Sandia Code

Among the multitude of available MD codes, LAMMPS[1] is one of the most used. The acronym stands for Large-scale Atomic/Molecular Massively Parallel Simulator. It is developed and maintained at Sandia National Labs. People from institutions all over the world have contributed to the program. Its features exceed the capabilities of IMD in some areas, in others it is LAMMPS which lacks some functionality. For this work LAMMPS was used as a comparison tool. More details are given in Sec. 7.3.2.

One of the most interesting features of LAMMPS is the possibility to use some sort of meta-programming in the input files. It is easily possible to write output data in a required format or do some post-processing without the need of external tools. An example is given in Sec. 9.5, where the LAMMPS output is written in a way, that the IMD post-processing tools can read it.

[1] http://lammps.sandia.gov/

Chapter 6:

Force matching with the potfit code

There are different approaches on how to get an empirical potential for classic MD simulations. A common way is to fit a potential to experimental data like lattice constants, cohesive energies, surface energies and other important quantities. For CMAs however, this approach is not viable, because there is only very little or no reference data available for these systems.

A different method, which does not rely on any experimental data is the force matching method [37]. It uses reference data calculated with first principle methods to establish an effective interatomic potential. While the *ab initio* forces provide the main source of reference data, one can use other *ab initio* calculated data to arrive at potentials for very special applications. Potentials generated for fracture simulations for example, should be fitted to lots of surfaces and strained/stressed configurations.

This chapter will give a description of the implementation of the force matching method in the *potfit* code and the algorithms used for optimization. An overview over the different interactions is given and the details of the analytic potentials are explained.

6.1 Overview of *potfit*

The *potfit* code has been developed by Peter Brommer during his diploma and PhD thesis work [21, 22]. The first versions were bundled with the IMD package (see Sec. 5.5). As more features were added, *potfit* was released as a standalone

application. It is freely available on the *potfit* homepage[1], licensed under the GNU General Public License, Version 2[2].

The capabilities of *potfit* have been greatly extended since the first release. The first version could only fit tabulated pair potentials, EAM potentials were added shortly afterwards. Initially there were only two optimization algorithms available, a third one has been added for the use with analytic potentials, which were implemented during the author's diploma thesis work [P1]. For the present thesis, the angular dependent potentials were added. More potential models like MEAM or electrostatic interactions were contributed by different authors. More information can be found on the *potfit* homepage and in [P4].

The application flow of *potfit* is very simple. After the program has read the parameter file, the configuration file and the potential file, neighbor lists for an efficient calculation of forces and energies are created. If the optimization is enabled, *potfit* enters the optimization loop, otherwise it is skipped. Finally the potential is evaluated and the output is written. This contains the deviations, some averaged deviations and the potential in various formats. The individual steps are described in detail in the following sections.

6.2 Force matching

Many interatomic potentials in the literature are fitted to experimental data, which is a convenient and reliable method to generate potentials for simple systems. Based on structural data from diffraction experiments, modules of elasticity or other quantities like vacancy formation or surface energy a potential can be fitted. For simple systems with only few atoms per unit cell this is not a problem. Complex metallic alloys usually have more atoms per unit cell, from about 20 to up to a few thousand. For such large structures it is unfeasible to create a viable structure model from diffraction data. If the diffraction data is available, the structure model very often contains split positions and fractional occupancies which cannot be implemented in computer simulations.

A different approach of generating an effective potential for a solid or liquid phase of a material is the force-matching method of Ercolessi and Adams [37]. It does not rely on any experimental data, only *ab initio* reference data is required. The main idea is to replace the few experimental data by a large number of first-principle

[1] http://potfit.sourceforge.net
[2] http://www.gnu.org/licenses/old-licenses/gpl-2.0

calculations. By using many different reference configurations, a force-matched potential is usually more reliable than the experimental approach. The drawbacks of these potentials are discussed in Sec. 6.4.

In order to use the force-matching method, a potential model is required which maps the potential to a set of discrete datapoints. The most common models are tabulated and analytic potentials. Tabulated potentials are defined by n parameters $\alpha_1, \ldots, \alpha_n$ which represent the value of the potential at a certain distance. Analytic potentials are also defined by n values of α, they represent the parameters of the analytic potential functions. Both methods are shown in Fig. 6.1.

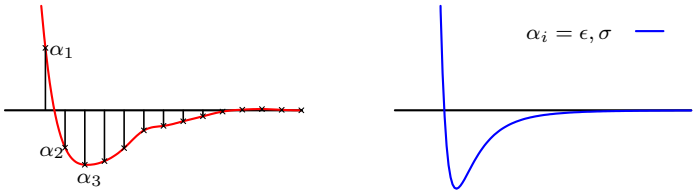

Figure 6.1: Two different ways of defining a potential model with n parameters $\alpha_1, \ldots, \alpha_n$. The tabulated potential is shown on the left. The parameters α_i represent the value of the potential at a certain distance. The analytic potential on the right is a Lennard-Jones potential with the functional form $V(r) = 4\epsilon[(\sigma/r)^{12} - (\sigma/r)^6]$. The parameters α_i represent the depth ϵ and width σ of the potential.

With either potential model, the set of parameters $\boldsymbol{\alpha}$ has to be optimized to reproduce the reference data as accurate as possible. An efficient way is by creating a mathematical function, which maps the parameters $\boldsymbol{\alpha}$ onto a single number. For force-matching, usually a sum of squares is used to form the so-called target function $Z(\boldsymbol{\alpha})$. It is defined as

$$Z(\boldsymbol{\alpha}) = Z_F(\boldsymbol{\alpha}) + Z_C(\boldsymbol{\alpha}), \tag{6.1}$$

with

$$Z_F(\boldsymbol{\alpha}) = \sum_{i=1}^{m} u_k (F_k(\boldsymbol{\alpha}) - F_k^0)^2, \tag{6.2}$$

and

$$Z_C(\boldsymbol{\alpha}) = \sum_{r=1}^{N_c} w_r (A_r(\boldsymbol{\alpha}) - A_r^0)^2. \tag{6.3}$$

The target function Z consists of two parts. Z_F is the contribution from all deviations to the reference data and Z_C can be used to put additional constraints on the parameters $\boldsymbol{\alpha}$. Both parts are calculated from deviations to a reference value. $F_k(\boldsymbol{\alpha})$ are the quantities calculated with the current parameter set $\boldsymbol{\alpha}$, for example forces, energies and stresses. The *ab initio* calculated values are denoted with a superscript 0. Each summand can be assigned a weighting factor u_k. The deviations for the constraints follow the same scheme, $A_r(\boldsymbol{\alpha})$ are the values calculated with the potential and A_r^0 are the desired values. It is also possible to assign weighting factors w_r to the different constraints.

If a potential can reproduce the reference data perfectly, the sum vanishes. In every other case, the sum is larger than zero. The objective of an optimization algorithm is to find the set of parameters $\boldsymbol{\alpha}$ which yield the smallest target function. Because the calculation of the individual components of the target function is very expensive, the algorithms used for optimization have to be efficient.

6.3 Optimization algorithms

Finding an optimal configuration is a common problem in many parts of scientific research. There is a whole area within computer sciences that only deals with optimization algorithms of different kinds. Many distinct approaches have been developed for engineering, economical and social problems.

In order to select an appropriate algorithm, the problem has to be analyzed in detail. The target function $Z(\boldsymbol{\alpha})$ is a function of continuous variables, which has many local minima. One requirement for the algorithm is the ability to leave local minima and cover a large area of the parameter space in an efficient manner. For the coarse optimization in *potfit* there are two different algorithms available. The simulated annealing has been implemented by Peter Brommer, the differential evolution algorithm has been added during this work. When running *potfit*, the user can choose between these two algorithms. Subsequently a conjugate gradient algorithm is used to descend to the minimum. While the former algorithms may be skipped, the latter one cannot be disabled.

The simulated annealing and the conjugate gradient algorithm are described in detail in the PhD thesis of Brommer [22]. Only short summaries will be given here. The new differential evolution algorithm is discussed extensively afterwards.

Random number generation

An important aspect of all stochastic optimization algorithms is the quality of the random number generator. Over the course of a *potfit* run, up to one billion random numbers may be required. To make sure that the random number sequence is reproducible, a pseudorandom number generator has to be used. The Mersenne twister algorithm from Saito and Matsumoto [102] has been implemented in *potfit*. It provides equidistributed random numbers in up to 623 dimensions, has a period of $2^{216\,091}-1$ and is optimized for double digits. Because of the high quality random numbers it provides, it is used in many computer codes for scientific research.

6.3.1 Simulated annealing

The simulated annealing algorithm is modeled after the annealing process in metallurgy. There a metal is heated and slowly cooled down again to increase the crystal size and reduce the number of defects of the material. This process allows the atoms to leave local minima of the configuration space and find new structures with lower internal energy.

The first implementation of the simulated annealing algorithm was presented by Kirkpatrick *et al.* [59] in 1983. It was used to find the optimal placement of chips on a module while taking into account the wiring. The algorithm is closely related to statistical mechanics and uses random numbers to find global minima. By allowing uphill moves that increase the value of the target function it is possible to leave local minima. The stochastic approach makes the algorithm feasible for problems with many degrees of freedom. While the original implementation was done for discrete problems, a version for continuous variables was proposed by Corana *et al.* [26]. A short summary of the algorithm is given in the next paragraph.

Optimization of functions with continuous variables

Let $\boldsymbol{x}$ be a vector in $\mathbb{R}^n$ with the components $(x_1, x_2, \ldots, x_n)$ and $f(\boldsymbol{x})$ the function to be minimized. The algorithm starts from a point $\boldsymbol{x}_0$, which can be generated randomly, given by the user or be the result of a previous optimization. Possible

candidates for a point $\boldsymbol{x}_{i+1}$ are generated by applying random moves along each coordinate direction to $\boldsymbol{x}_i$. The new coordinates are uniformly distributed around the corresponding coordinate of $\boldsymbol{x}_i$; the width of the distribution is given by the step vector $\boldsymbol{v}$. A candidate point $\boldsymbol{x}'$ is accepted according to the Metropolis criterion:

If $\Delta f \leq 0$, then accept the new point: $\boldsymbol{x}_{i+1} = \boldsymbol{x}'$
else accept the new point with a probability $p(\Delta f) = \exp(-\Delta f/T)$

where $\Delta f = f(\boldsymbol{x}') - f(\boldsymbol{x}_i)$ and T is a parameter which is identified with temperature.

For a constant value of T, the series of points $\boldsymbol{x}_i$ does not follow a downhill direction of the target function f. A large temperature, compared to the average of Δf, will accept all candidate points and yield a random sampling of f.

For a successful optimization the simulated annealing algorithm has to be started at a "high" temperature given by the user. After a certain number of trial steps is performed, which is three times the dimension of $\boldsymbol{x}$ in *potfit*, it is assumed that the algorithm has sampled the target function f sufficiently. The step vector $\boldsymbol{v}$ is periodically adjusted, to ensure a balance between accepted and rejected sampling points. A new optimal point found is stored as $\boldsymbol{x}_{\text{opt}}$. The temperature is reduced and the algorithm starts again with creating trial points and evaluating the target function.

There are different stopping criteria for this algorithm. In *potfit* the optimization is aborted if there is only little or no improvement in the lowest value of the target function $f(\boldsymbol{x}_{\text{opt}})$ or the temperature has been decreased 1000 times.

Determination of the starting temperature

It may be difficult for the user to select an appropriate starting temperature. If it is chosen too high, many unnecessary optimization steps are performed. If the temperature is too low, the sampling of the target function f might not cover the whole parameter space.

There are methods to approximate a proper starting temperature T_0 for simulated annealing algorithms. The idea is to randomly sample the parameter space and determine a temperature, that accepts almost all steps. Such a procedure, however, can only be applied, if the initial point is a random point. It does not work when $\boldsymbol{x}_0$ is already optimized.

To enable the feature in *potfit*, the `anneal_temp` parameter has to be set to `auto`. The starting temperature will then be determined before the optimization of the potential. Starting from the potential given by the user, m_0 sample steps are

performed and the temperature T_0 is given by

$$T_0 = \overline{\Delta f^+} \left(\log \frac{m_2}{m_2 \chi_0 - m_1(1-\chi_0)} \right)^{-1}. \tag{6.4}$$

m_1 and m_2 denote the number of steps ($m_1 + m_2 = m_0$) with $\Delta f \leq 0$ and $\Delta f > 0$, respectively and $\overline{\Delta f^+}$ is the average value of those Δf values, for which $\Delta f > 0$. The number of steps m_0 is chosen as ten times the number of free parameters and the acceptance rate χ_0 as 0.8, as proposed by Ali and Gabere [2].

6.3.2 Powell's conjugate gradient algorithm

After the optimization of the potential with either the simulated annealing or differential evolution algorithm, a conjugate gradient method is applied subsequently. Unlike the previous algorithm, is not able to leave local minima. However, it is very efficient, regarding the number of function evaluations, in finding the local minimum.

The algorithm used in *potfit* was first described by Powell [96] in 1965. It is an enhancement of the generalized least squares method, which can be found in [97]. Many of the implementations of the generalized algorithm are not suited for the optimization of the error sum in *potfit* for two reasons. They assume a general form of Z and do not take the high computational cost of calculating the gradient of Z into account.

Powell's method is designed to work with a sum of squares of non-linear functions. It needs the gradient only for the initial step and uses an approximation for all further steps. The errors due to the approximation do not disturb the optimization and the algorithm exhibits convergence properties comparable to the generalized least squares method.

The generalized least squares method

The force-matching problem can be recast as the minimization of

$$Z(\boldsymbol{\alpha}) = \sum_{k=1}^{m} [f^{(k)}(\boldsymbol{\alpha})]^2, \tag{6.5}$$

where the $f^{(k)}$ represent all quantities from (6.2) and (6.3) that contribute to the error sum. To solve this problem, different numerical algorithms are available. A

common way is to rephrase it into a linear system of equations,

$$\boldsymbol{A}\boldsymbol{\chi} + \boldsymbol{b} = 0, \tag{6.6}$$

which can be solved quickly with the help of linear algebra routines. A comprehensive description of the derivation of the least squares and Powell algorithms is given by Brommer [22].

Minimization according to Powell

Powell's algorithm can be used to minimize a sum of squares without calculating derivatives. It uses difference quotients to estimate the gradient along a certain direction in space. The errors from this approximation are negligible for the convergence of the algorithm. One disadvantage of the applied gradient method is the fact, that a local minimum cannot be left. A careful choice of the starting point is essential for the success of this method. In *potfit* the starting point is usually the result of a previous global optimization like simulated annealing or differential evolution.

6.3.3 Evolutionary algorithm

Another stochastic optimization scheme has been implemented in *potfit* alongside analytic potentials. The algorithm belongs to the class of evolutionary methods, which have become increasingly popular over the last decade. Great efforts have been made to improve these methods and to broaden their range of application. The idea is based on the principles of the evolution theory from biology. There the natural selection often is paraphrased with the "survival of the fittest".

An evolutionary algorithm works with many approximate solutions to a problem, which are referred to as the population. During one optimization step the population is subjected to mechanisms inspired by biological evolution: reproduction, mutation, recombination and selection. New approximate solutions are created and in the end only the ones with the best target function values are carried over to the next step.

One advantage of evolutionary algorithms is, that there are no special requirements for the target function. Other algorithms, like conjugate gradient methods, need a smooth target function with a well-defined derivative. That is not the case for differential evolution. For *potfit* it is not an issue, but there are many optimization problems where the target function has no mathematical closed-form expression. The fact that the evolutionary algorithm yields good results for many different types

of applications made it very popular.

In the following, the algorithm used in *potfit* is described in detail. Some additional techniques, which can speed up the optimization are also discussed.

Differential evolution

The algorithm used in *potfit* is called Differential Evolution (DE). It is a vector based stochastic optimization method, which has been introduced by Storn and Price [108]. Like all evolutionary algorithms it does not work with a single solution, instead a uses a population P:

$$P_g = \{\boldsymbol{x}_{i,g}\}, \quad i = 0, 1, \ldots, N_p - 1, \quad g = 0, 1, \ldots, g_{\max} \tag{6.7}$$

$$\boldsymbol{x}_{i,g} = \{x_{j,i,g}\}, \quad j = 0, 1, \ldots, D - 1, \tag{6.8}$$

where N_p denotes the number of population vectors, g counts the generations and D is the dimensionality of the problem. In *potfit* D is equal to the number of free parameters and N_p is set to $15D$. The vector $\boldsymbol{x}_i$ in (6.7) is equivalent to a set of parameters $\boldsymbol{\alpha}$ from (6.1).

The initialization of the population is done is two steps. At first, the initial potential provided by the user is read and stored as $\boldsymbol{x}_{0,0}$. All remaining vectors are then generated by adding random numbers to each parameter:

$$\lambda_j = \text{rand}_j \tag{6.9}$$

$$x_{j,0,0} = \begin{cases} x_{0,0,0} + \lambda_j (b_{j,\text{U}} - x_{j,0,0}) & \text{if } \lambda_j > 0 \\ x_{0,0,0} + \lambda_j (x_{j,0,0} - b_{j,\text{L}}) & \text{if } \lambda_j < 0. \end{cases} \tag{6.10}$$

λ_j is a normally distributed random number, scaled by a factor of 0.33. The index j indicates that a new random number is generated for each parameter. The D-dimensional initialization vectors $\boldsymbol{b}_\text{L}$ and $\boldsymbol{b}_\text{U}$ indicate the lower and upper bounds of the parameter vectors $\boldsymbol{x}$. The target function Z is calculated for each $\boldsymbol{x}_{i,0}$ and stored in an array for later use. The second step is an opposite check – a special technique which is not part of the standard DE algorithm. It is explained later on.

After the initialization is complete, the main optimization loop is entered. It consists of three parts: mutation, crossover and selection. For reasons of parallelization, DE works with two arrays for the population. One holds the current and one the next generation. If the selection has been performed, the next generation is copied to the array holding the current one. Afterwards the loop is started again unless some

abortion criteria have been met. In *potfit*, the DE loop also includes an opposite check, which is performed after the selection, but before the start of a new loop.

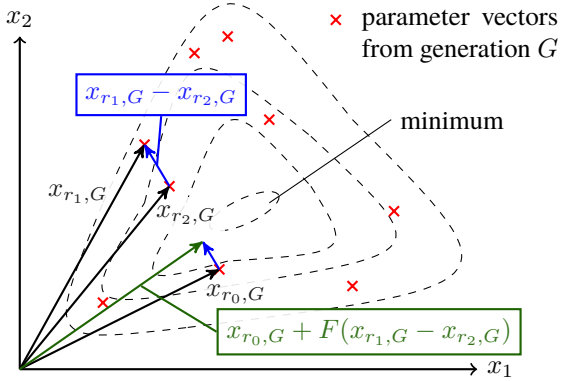

Figure 6.2: Contour plot of a two-dimensional cost function. The creation of a mutation vector is illustrated. Individuals are drawn as black arrows, the mutation vector in green.

Mutation In the first part of the DE optimization loop a mutation vector $\boldsymbol{v}_{i,g}$ is created from the current population by combining several individuals $\boldsymbol{x}_{i,g}$. There are several different approaches on how to perform the combination. The basic version of DE uses the following:

$$\boldsymbol{v}_{i,g} = \boldsymbol{x}_{r_0,g} + F\left(\boldsymbol{x}_{r_1,g} - \boldsymbol{x}_{r_2,g}\right). \tag{6.11}$$

The indices r_0, r_1 and r_2 are integer random numbers which should be mutually exclusive. Each mutation vector is composed of a random vector plus the difference of the other random vectors scaled by an amplification factor F. A schematic representation of a two-dimensional optimization is shown in Fig. 6.2.

Other possible ways of generating mutation vectors are:

$$\boldsymbol{v}_{i,g} = \boldsymbol{x}_{\text{best},g} + F\left(\boldsymbol{x}_{r_1,g} - \boldsymbol{x}_{r_2,g}\right), \tag{6.12}$$

$$\boldsymbol{v}_{i,g} = \boldsymbol{x}_{r_0,g} + F\left(\boldsymbol{x}_{r_1,g} + \boldsymbol{x}_{r_2,g} - \boldsymbol{x}_{r_3,g} - \boldsymbol{x}_{r_4,g}\right), \tag{6.13}$$

$$\boldsymbol{v}_{i,g} = \boldsymbol{x}_{r_0,g} + (1-F)\left(\boldsymbol{x}_{\text{best},g} - \boldsymbol{x}_{r_1,g}\right) + F\left(\boldsymbol{x}_{r_2,g} - \boldsymbol{x}_{r_3,g}\right). \tag{6.14}$$

The index 'best' indicates the vector with the lowest target function and r_i are again mutually exclusive random numbers in $[0, N_p - 1]$. There is a notation to classify all different mutation variants of the DE algorithm – DE/x/y/z. The x denotes the base vector, y denotes the number of difference vectors used and z represents the crossover method. The version in Eq. (6.11) is called DE/rand/1/exp, it uses a random base vector $\boldsymbol{x}_{r_0,g}$ and one difference vector. Mutation schemes in Eqs. (6.12) to (6.14) are called DE/best/1/bin, DE/rand/2/bin and DE/rand-to-best/1/bin, respectively. They are all available in *potfit*, as well as DE/best/2/bin and DE/rand-to-best/2/bin. As a rule of thumb, the value for the amplification factor F should be between 0.5 and 1. In *potfit* the value is determined automatically by an algorithm, which is explained in detail in the paragraph "Self adapting parameters".

Crossover To get a diversity enhancement in the population, a crossover step is performed. It mixes the previously generated mutation vectors $\boldsymbol{v}_{i,g}$ with the target vectors $\boldsymbol{x}_{i,g}$ in order to generate trial vectors $\boldsymbol{u}_{i,g}$. Generally just a binary choice is made, which is defined as

$$\boldsymbol{u}_{i,g} = u_{j,i,g} = \begin{cases} v_{j,i,g} & \text{if } \mathrm{rand}_j[0,1) < C_r \\ x_{j,i,g} & \text{otherwise.} \end{cases} \tag{6.15}$$

The jth component of the mutant vector is accepted for the trial vector with a probability of C_r. If this is not the case, the component of the target vector is retained. $\mathrm{rand}_j[0,1)$ is a uniformly created random number and C_r is called crossover rate. In order to prevent the case $\boldsymbol{u}_{i,g} = \boldsymbol{x}_{i,g}$ at least one component of the mutant vector $\boldsymbol{v}_{i,g}$ is always accepted. The general recommendation of $C_r \in [0.8, 1.0]$ is given in [108]. In *potfit* this parameter is also part of the self-adapting algorithm and is not set explicitly.

Selection The last part of the DE optimization loop is a simple one-to-one selection. Each trial vector $\boldsymbol{u}_{i,g}$ competes against the corresponding target vector $\boldsymbol{x}_{i,g}$. The one which yields the lower target function Z survives into the next generation $g + 1$:

$$\boldsymbol{x}_{i,g+1} = \begin{cases} \boldsymbol{u}_{i,g} & \text{if } Z(\boldsymbol{u}_{i,g}) \leq Z(\boldsymbol{x}_{i,g}) \\ \boldsymbol{x}_{i,g} & \text{otherwise.} \end{cases} \tag{6.16}$$

After the selection has been performed the algorithm checks, if any of the abortion criteria are met. If that is the case, the optimization is complete, otherwise another optimization loop is performed. The abortion criterion given by STORN and PRICE is very simple. After $g_{\max}$ generations have been calculated, the algorithm should be canceled. As there is no real prediction possible, how many iterations the algorithm needs to achieve an acceptable result, a different criterion have been implemented in *potfit*. A critical threshold is introduced with a value of 10^{-6}, which can be adjusted by the user. After each loop, the difference of the target vectors with the smallest and largest target function is calculated. As long as the difference is greater than the critical threshold the optimization will do another loop. That means until all target vectors have not yet retracted to a very narrow area in parameter space the algorithm will continue. Additionally, the optimization is stopped if the target function is less than the critical threshold.

Some additional methods are available, which can improve the performance of the DE algorithm. They were not part of the original version, they have been added later by different authors. In the case of *potfit* two enhancements are used, the opposite check and the self-adapting parameters. They both can speed up the optimization and make it computationally more efficient.

Opposition-based differential evolution

The regular DE scheme starts with some candidate solutions and tries to improve them towards an optimal solution. The computational time, among others, is related to the distance of these initial guesses from the optimal solution. One way of speeding up the optimization process is to simultaneously check the opposite solutions. A detailed description of the opposition-based DE along with verifications and tests can be found in [24].

The enhancement is based on the concept of opposite numbers. For a real number x in the interval $[a, b]$ the opposite, denoted by $\breve{x}$, is defined as

$$\breve{x} = a + b - x. \tag{6.17}$$

This definition can also be applied to a point in higher dimensional space. For a D-dimensional point $Q(x_1, x_2, \ldots, x_D)$, where $x_1, x_2, \ldots, x_D$ are real numbers and $x_i \in [a_i, b_i], i = 1, 2, \ldots, D$, the opposite point $\breve{Q}$ is defined as $\breve{Q}(\breve{x}_1, \breve{x}_2, \ldots, \breve{x}_D)$ where

$$\breve{x}_i = a_i + b_i - x_i. \tag{6.18}$$

In the implementation there are two distinguishable stages, the initialization stage and the generation advancement.

Initialization After the DE algorithm has finished the initialization, an opposite check is performed. There are three steps, which are necessary. First the opposite population O_0 is created as described above in Eq. (6.18):

$$O_{i,j} = a_j + b_j - P_{i,j}, \quad i = 1, 2, \ldots, N_p, \quad j = 1, 2, \ldots, D. \tag{6.19}$$

Then the target function is evaluated for each target vector $\boldsymbol{x}_{i,0}$ in O_0. Finally the N_p target vectors from the set $\{P_0, O_0\}$, which yield the lowest error sum, are determined. They are stored in P_0 and will be used as the initial population of the DE algorithm.

To determine the target vectors with the lowest error sum, the set $\{P_0, O_0\}$ is stored in a single array, as well are the corresponding error sums. Then a quicksort algorithm is used to efficiently sort both arrays. Finally the first N_p entries of the array can be used as the new population.

Generation advancement The opposite check for the generation advancement works basically in the same way as for the initialization step. It is performed after the selection stage, with a certain probability J_r, called jumping rate. Usually the probability is set to $60\,\%$ at the beginning of the optimization. After every ten opposite checks, J_r is multiplied by a factor of 0.9. For an ongoing optimization, the probability to perform an opposite check is continuously reduced. The reasons for that are rather simple. First, the opposite check is computationally almost as expensive as one iteration of the basic DE algorithm. Second, as the optimization progresses, all target vectors move closer and closer together. The probability to achieve a significant improvement with an opposite check will thus become smaller and smaller. Finally, RAHNAMAYAN *et al.* [98] showed, that a decreasing jumping rate leads a faster convergence than a constant or increasing one.

The generation advancement however has one important difference from the initialization routine. The opposite of each parameter is calculated dynamically. That means, that the maximum and minimum value of each parameter no longer is given by the predefined interval $[a_j, b_j]$. It is determined from the minimum and maximum values of the individual parameters in the current population:

$$O_{i,j} = \mathrm{MIN}_j^g + \mathrm{MAX}_j^g - P_{i,j}, \quad i = 1, 2, \ldots, N_p, \quad j = 1, 2, \ldots, D. \tag{6.20}$$

MIN_j^g (MAX_j^g) denotes the minimal (maximal) value of the jth component of all target vectors in generation g. That is necessary, to prevent a jump outside of the already shrunken search space, which would destroy the converged population. Hence, the opposite is calculated with respect to the extent of the current population and not the initial range $[a_j, b_j]$.

Self-adapting control parameters

The choice of the control parameters in differential evolution simulations is a complex task. A set which works well for one problem may fail for a different one. Heuristic rules to determine these parameters were developed. However, these rules are not applicable globally. They also may only work for certain problems. A simple solution that can handle all problems is to include the control parameters into the population and allow them to evolve along with the main parameters.

According to Eiben *et al.* [34], the change of control parameters can be categorized into three classes.

1. *Deterministic parameter control*, which alters the parameters according to a deterministic scheme.
2. *Adaptive parameter control*, which uses some kind of feedback from the optimization to change the parameters.
3. *Self-adaptive parameter control* is the idea of "evolution of the evolution". The control parameters are also subject of the optimization and will be adjusted to optimal values.

One possible way of using the self-adaptive parameter control with differential evolution has been proposed by Brest *et al.* [20]. The algorithm optimizes the two parameters F and C_r while keeping the population size N_p fixed.

Each target vector $\boldsymbol{x}_{i,g}$ is extended by two additional parameters, $F^{(i)}$ and $C_r^{(i)}$. The previously global parameters F and C_r are now replaced by "per vector" parameters, which can be added to the optimization very easily. The new control parameters are calculated as

$$F_{g+1}^{(i)} = \begin{cases} F_l + \mathrm{rand}_1 F_u & \text{if } \mathrm{rand}_2 < \tau_1 \\ F_g^{(i)} & \text{otherwise} \end{cases} \tag{6.21}$$

and

$$C_{r,g+1}^{(i)} = \begin{cases} \text{rand}_3 & \text{if rand}_4 < \tau_2 \\ C_{r,g}^{(i)} & \text{otherwise.} \end{cases} \tag{6.22}$$

rand_i, with $i \in \{1, 2, 3, 4\}$, are uniform random values from $[0, 1]$, τ_1 and τ_2 represent the probabilities of adjusting the control parameters F and C_r, respectively. F_l and F_u are the lower and upper bound for the amplification factor F, C_r takes values from $[0, 1]$. In *potfit* the values for τ_1, τ_2, F_l, F_u are taken as fixed values $0.1, 0.1, 0.1, 0.9$. The new values for F and C_r are calculated before the mutation is performed, so they are used in the generation of the new population P_{g+1}.

Field of application

The DE algorithm has primarily been implemented for the use with analytic potentials (Sec. 6.6). It can also be used for tabulated potentials, but there are some drawbacks, which make it less efficient than the simulated annealing algorithm. The support of differential evolution has to be enabled explicitly at compile time, otherwise simulated annealing is used.

The main reason why DE does not work well with tabulated potentials are the missing bounds for the parameters. For analytic potentials, the user has to specify the range $[a_j, b_j]$ for each parameter explicitly. That is not the case for tabulated potentials. Using the DE scheme without any bounds is possible, but very error-prone. A simple one-dimensional example shall be given to explain the problem.

Let P be a generation with $N_p = 4$ individuals. Their values are $x_i = i$, $i = 1, 2, 3, 4$ and the minimum value of the target function is at $x_0 = 20$. It is very unlikely to reach x_0 by the means of the mutation rules given in Eqs. (6.11) to (6.14). For a simple downhill target function, the optimal value can be reached after few generations. For complex target functions, it might never be reached.

If all parameters of a potential are in a very narrow range far away from the optimum, the DE algorithm might be very ineffective. The solution of adding upper and lower bounds for tabulated potentials is not possible. In *potfit*, the unit system is not fixed, it can be chosen be the user. Bounds for the potential values which work for electron volts may be completely wrong for a different energy unit.

The simulated annealing does not suffer from this problem. It does not rely on bounds and is thus the standard optimization algorithm in *potfit*.

6.4 Reference data

The quality of a force-matched potential significantly depends on the reference data used in the fitting process. The key concept which is important in this context is transferability. It describes the ability of a certain potential to correctly describe different configurations with the same parametrization. For effective potentials there is usually a trade-off between transferability and precision. A potential that can reproduce energy and forces of a single configuration with high accuracy is less transferable. In contrary, a transferable potential can describe different configurations, but with lower accuracy.

In *potfit* there are two ways to influence the fitting process with regard to transferability. One is the possibility to use weights for the different parts of the target function Z. The other is the proper choice of reference configurations. To get a transferable potential, which is usable in different situations, a wide range of reference structures should be used. Configurations with different lattice types as well as surfaces, grain boundaries or any type of defects may be included. For a precise potential the selection of reference structures should contain mostly related configurations with similar local atomic environments. Reducing ambiguities in the reference data usually leads to a more accurate potential.

The decision, if a potential should be more precise or more transferable depends on its intended use. An example for the application of a transferable potential are phase transitions, where the potential has to be able to describe all phases which are involved. For a structure optimization, a very precise potential is needed. All occurring structures are very similar, the important quantity is the accuracy of the energy. The direction of the potential fitting can be steered with different weighting factors.

Another problem, which has to be considered is the radial distribution function $g(r)$ of the reference data. To generate a reliable potential, forces should be available from a minimum distance $r_{\min}$ to the cutoff distance r_c. Otherwise the optimization problem may contain degrees of freedom that do not influence the result. An example is shown in Fig. 6.3.

There are two different approaches to eliminate unsupported parameters. On the one hand the set of reference configurations can be extended to include additional structures, which, however, is not always possible or might require new and time consuming DFT calculations. On the other hand the parametrization of the potential can be changed. For a tabulated potential the unsupported nodes at the beginning can be omitted or the spacing between nodes can be changed to solve the problem.

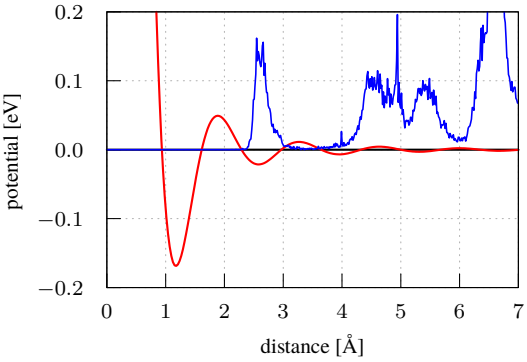

Figure 6.3: A potential (red) with unsupported parameters and the corresponding radial distribution function (blue). The first minimum of the potential at a distance of about 1.1 Å is not supported by the reference data. All parameters, that are responsible for the first minimum can be changed without changing the error sum.

In the case of analytic potentials the solution may not always be trivial, but the lower and upper bounds of the parameters can be used to prohibit such features.

6.4.1 Weights

The influence of the different kinds of reference data on the potential fitting can be adjusted with several weighting factors. There are two global weights, the energy weight w_E and the stress weight w_S. When the contributions to the error sum are calculated, these factors are multiplied onto the errors to increase or decrease their influence on the optimization. The deviation part Z_F of (6.2) can be written in detail as

$$Z_F = \sum_{i=0}^{m} \left(F_i - F_i^0\right)^2 + w_E \sum_{j=0}^{k} \left(E_j - E_j^0\right)^2 + w_S \sum_{l=0}^{6k} \left(S_l - S_l^0\right)^2 . \quad (6.23)$$

The weighting factors w can be used to adjust the relative importance of the force, energy and stress deviations. While the force term is always fixed at a weight of

$w_F = 1$, the other weights can be any number greater or equal to 0. The special case $w = 0$ disables the contribution to the error sum.

By choosing the correct ratio of the weighting factors, the optimization can be guided into different directions. A high energy or stress weight will yield a precise potential, which is only little transferable. Small weights put the emphasis on the forces. To arrive at transferable potentials, the weights should be chosen in such a way that all parts of (6.23) do contribute to the error sum. In practice this can be a really tricky issue as several aspects have to be considered.

The most important thing is the different number of summands in each sum in (6.23). There are m forces, k energies and $6k$ stress deviations which are all summed up. While m, which is equal to three times the total number of atoms, can be as large as a few ten thousands, k is usually in the range from 20 to 100. Another point are the different units for forces, energy and stresses. Forces are given in eV/Å, energy in eV/atom and stresses in units of 160.2 GPa. The numeric values of the deviations often differ by several orders of magnitude. As there is no general rule, the weights have to be adjusted for each optimization run individually. To support the user, *potfit* will write all contributions to the error sum into different files. They can be used to generate scattering plots, which yield a rough estimation of the contribution for each type of data. An example is shown in Fig. 6.4. These data can be used to choose the appropriate weighting factors.

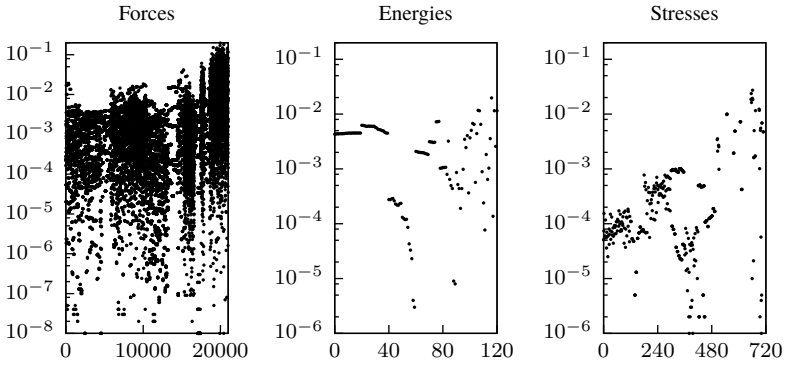

Figure 6.4: All contributions to the error sum of a MgZn potential, created for testing purposes in [P1]. The horizontal axis counts the number of datapoints for each quantity. The unweighted error sums for the individual parts are 72.207 for forces, 0.395 for energies and 0.910 for stresses.

There is also another type of weighting factors available, which can be used to control the optimization. They are called configuration weights and apply to all quantities calculated from a single configuration. The total error sum of all deviations Z_F can be expressed as a sum over all configurations,

$$Z_F = \sum_{c=0}^{P} w_c Z_F^c, \tag{6.24}$$

where P is the total number of configurations, w_c the configuration weight and Z_F^c the sum of errors for a single configuration. These weights can be used to put the emphasis of the fitting process on specific configurations while retaining others which are less important.

6.5 Tabulated potentials

A convenient way of storing interatomic potentials is a simple table. The value of each potential function at a few thousand sampling points is stored in a text file. The tabulated format was the first one supported by *potfit*. It is inspired by MD codes, where potentials are usually stored in memory as arrays. Computers can perform table lookups much faster than calculating the potential value from an analytic formula. For running MD simulations the tabulated potential is read at the beginning and stored in memory. To determine a value between two sampling points, different kinds of interpolation methods can be used.

Optimizing tabulated potentials in *potfit* uses sampling points with cubic spline interpolation. However, the number of sampling points has to be reduced greatly, compared to MD potentials. There is no limit, yet no more than 15 should be used for a single potential. There are two reasons for that. First, the number of degrees of freedom should be as small as possible. The optimization algorithms can handle problems with about one hundred parameters in reasonable time. With an increasing number of degrees of freedom the optimization time increases and the probability to find the global optimum decreases. Second, the parameters should all be independent of one another. For densely tabulated potentials the single parameters cannot be changed individually. Changing a single value also changes the neighboring values significantly. Fig. 6.5 illustrates the problem.

Changing a parameter in a tabulated potential is not straightforward. To fulfill the energy and momentum conservation, a potential and its derivative have to be

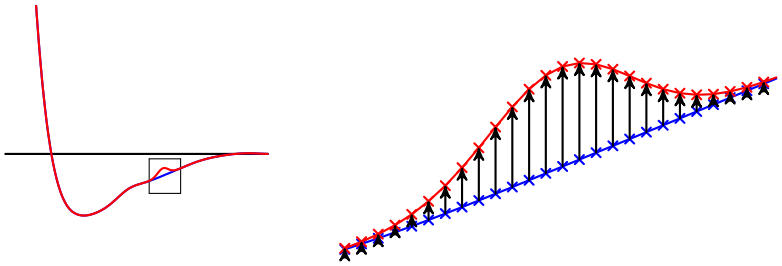

Figure 6.5: Changing a parameter of a densely tabulated potential. The blue potential on the left is tabulated with 200 sampling points. Its value at $r = 5$ Å is changed by adding a Gaussian, yielding the red potential. The area inside the square is magnified on the righthand side. At each sampling point the old blue potential is connected to the new red potential with an arrow.

smooth. By simply adjusting a single parameter without adapting its neighbors, the interpolated potential may lead to undesired results in MD simulations. One possible solution is using Gaussians to change a potential. Instead of changing a single value, a Gaussian, centered at the distance of the considered parameter, is added to the potential. Neighboring parameters are automatically changed while keeping the potential function and its derivative smooth. An example is shown in Fig. 6.5.

For a reasonable spacing of the sampling points, the neighboring values only should only be changed marginally. The parameters can be considered independent and the optimization algorithms work at optimal performance. No additional artificial constraints need to be taken care of. A potential with proper spacing is shown in Fig. 6.6.

If *potfit* is compiled for tabulated potentials, the way parameters are changed depends on the optimization algorithm. For simulated annealing, the previously described Gaussian is added to the current potential to generate a new trial potential. The properties of the Gaussian are also determined with a random number generator. The width and height are the absolute value of normally distributed random numbers, yet the height is multiplied by the distance vector $\boldsymbol{v}$ (see Sec. 6.3.1). Powell's least squares algorithm is used for finding the absolute minimum of a prerelax

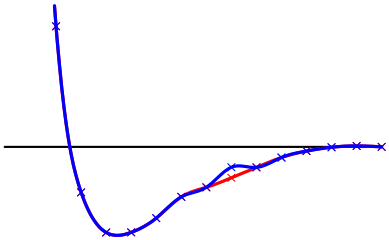

Figure 6.6: The same potential as in Fig. 6.5, tabulated at only 15 sampling points. The potential between the sampling points is interpolated with splines. Applying the same change as before, adding a Gaussian at $r = 5$ Å, yields the red potential. The parameter at the center is changed as desired whereas the neighboring parameters remain virtually unchanged.

potential. The changes for single parameters are very small and usually do not affect the neighboring datapoints. That is why the parameters are changed directly without the addition of Gaussians. The third optimization algorithm, differential evolution, is not suitable for tabulated potentials. The main reason is the same as for densely tabulated potentials. By combining parameter values from different potentials, the neighbors would also have to be changed. This is contradicting to the biological principles the algorithm is based on. It is however possible to use the differential evolution scheme with tabulated potentials, the results are usually not as good as with simulated annealing.

For the present work only analytic potentials have been used. More details on tabulated potentials can be found in [22] and on the *potfit* homepage.

6.6 Analytic potentials

A different way of representing interatomic potentials with a set of parameters are analytic functions. In addition to the free parameters a functional form has to be defined. There are several well-known analytic potentials, Lennard-Jones [73] and Morse [84] being the most popular ones. Many different functional forms have been developed since. An overview of the functions used in this work can be found

in Sec. 6.6.3, all available potentials in *potfit* are listed on the *potfit* homepage.

In general analytic potentials can be defined with few parameters. The Lennard-Jones potential has only two free parameters (cf. Fig. 6.7). With a small number of parameters the optimization space is also very limited and the algorithms can work efficiently. On average an analytic potential consists of three to six free parameters. An EAM potential for a binary system has about 30 parameters, an ADP potential about 50 to 60. Tabulated potentials on the other hand usually have more free parameters, up to twice of the number of analytic potentials

For analytic potentials, there is the possibility that the parameters have a physical meaning. In a Lennard-Jones potential, the parameters ϵ and σ are directly related to the dimer binding energy and the equilibrium distance, respectively. Another example are the EAM potentials from Johnson and Oh [56] for bcc metals. They contain the unrelaxed vacancy formation energy, the atomic volume, the Voigt shear modulus as well as the anisotropy ratio. These kind of relations can be derived analytically for simple lattice types like fcc or bcc. For CMAs, these relations do not hold because of the complex atomic arrangements.

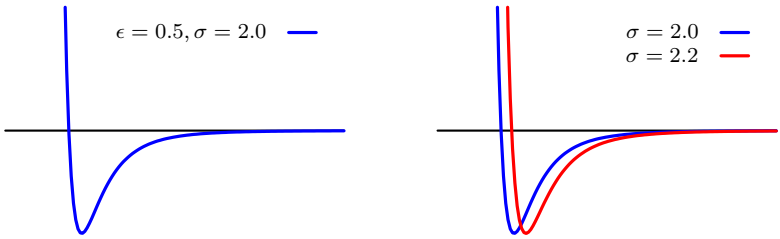

Figure 6.7: Two plots of analytic Lennard-Jones potentials. The potential on the left is defined by the two parameters $\epsilon = 0.5$ and $\sigma = 2.0$. The right plot highlights the influence of a single parameter on the whole range of the potential. Changing σ from 2.0 to 2.2 changes the potential at almost every distance.

When comparing analytic to tabulated potentials, they have one decisive advantage. For tabulated potentials it is very important to support all sampling points with reference data. Otherwise these parameters are unsupported and can obstruct a proper optimization. Analytic potentials do not suffer from this problem. Param-

eters are no longer local, as for tabulated potentials, they have an effect at most distances. An example is shown in the right part of Fig. 6.7. By choosing the proper analytic function for a potential, the reference data need not be continuous. It may contain gaps or consist only of a few peaks. One important aspect is the fitting of potentials for systems with minor constituents. If there are only few atoms of a certain species in each reference configuration, the tabulated approach will usually yield a potential which is only reliable at certain distances. With analytic functions the problem can be circumvented.

The drawback of analytic potentials are the predefined functional forms. While tabulated potentials can assume virtually all possible functions, analytic potentials are very limited. By choosing a Lennard-Jones potential for a certain interaction, it is not possible to generate a parametrization which incorporates oscillations or a second minimum. If an analytic function is inadequate for a system, the result of the optimization will exhibit considerable deficits. Selecting the appropriate functional form for an analytic potential is a crucial step in the optimization process. As a starting point, potentials of similar systems can be used or functions which are more flexible can be considered.

There are analytic potentials which are very rigid and which are more flexible. The behavior depends on the number of free parameters to some degree. Potentials with two or three parameters often have the same shape, which can only be scaled or translated. Typical examples for rigid potentials are the Lennard-Jones and the Morse potentials. An example for a flexible parametrization is the EOP potential from Mihalkovič *et al.* [81]. It is discussed in detail in Sec. 6.6.3.

In the next subsections some technical details of analytic potentials in *potfit* will be discussed. The format of a potential file is explained, the internal data flow as well as additional aspects of analytic potentials are reviewed. Finally the functional forms used for this work will be introduced.

6.6.1 Potential files and internal calculations

To store analytic potentials efficiently a simple data format has been defined. It consists of two parts, a header and a body. The header contains information on the type of the interaction and the number of potentials. An example is shown in Code Listing 6.1. The body holds the actual potential data, like the type and the parameters.

The first line, starting with `#F`, has two parameters. One for the potential format and one for the number of potentials. In *potfit*, the potential formats were adopted

```
#F 0 5
#T ADP
#C Ge
## Ge-Ge Ge Ge Ge-Ge Ge-Ge
#I 0 0 0 0 0
#E
```

Code Listing 6.1: Potential file header data for a Germanium ADP potential. Each header line starts with a # character, comment lines are marked with ##. More details are given in the text.

from IMD, so the formats 3 and 4 stand for tabulated potentials while format 0 denotes analytic potentials. The line with the `T` specifies the type of potential. From a computational point of view it is unnecessary, but it can be very helpful for the user. The same is true for the `C`-line, which holds the names of the chemical elements. It is mainly used to properly label output data with interaction names, like Al-Mn, instead of numbers like 0-1. A line starting with two # characters is considered a comment and is ignored. Usually all interactions are listed there in the same order as the appear in the file. To disable the optimization for one or more potential the `I`-line can be used. There has to be a single digit for each potential, setting it to `1` will not optimize that particular potential. The end of the header has to be marked with line containing only `#E`. Only body data is allowed after this point.

```
type     lj
cutoff   7
epsilon  0.10 0.00 1.00
sigma    2.50 1.00 4.00
```

Code Listing 6.2: Definition of a Lennard-Jones potential in *potfit*.

To specify analytic potentials there is also a special format. A Lennard-Jones potential is shown in Code Listing 6.2. Each potential definition starts with the `type` keyword. It is followed by the unique identifier for a potential function, `lj` in this case. The keywords for all available functions can be found on the *potfit* homepage. The next line specifies the cutoff distance for the potential. It is not a global setting, it can be different for each potential. After the type and cutoff lines, the parameter values have to be specified. Each line needs exactly four entries.

They are the parameter name, its value, minimum and maximum. The order of the parameters for a functional form is fixed and has to be obeyed. The parameter name given in the potential file is not respected for. It is only used for easy readability. Detailed descriptions for each function and the order of parameters are available on the *potfit* homepage.

After the potential files have been read by *potfit* the data is stored in memory. To speed up the calculation, each analytic potential is tabulated at 500 sampling points. The potential value is then interpolated from the table instead of calculated directly from the analytic formula. Tabulating the analytic potentials has two advantages. First, the force routines for tabulated and analytic potential can almost be identical. They can access the potential data in the same way without any further conversion. Second, new force routines from IMD or other MD codes can be adapted to *potfit* rather easily because of the similar potential data structures.

Every time a potential value is changed, the corresponding table has to be updated. The computational effort, however, is negligible, usually only one potential has to be updated while the other ones remain unchanged. Depending on the mathematical functions used in the functional forms, tabulating potentials can improve the performance of the force calculation by several orders of magnitude. Especially potentials with exponential or trigonometric functions are computationally expensive functions.

Smooth cutoff

Another problem for analytic potentials is the cutoff distance r_c. To conserve energy and momentum in an MD simulation, the potential as well as its derivative have to vanish smoothly at the cutoff. Otherwise, atoms entering or leaving the interaction distance of other atoms can suddenly become accelerated or decelerated.

For tabulated potentials the problem can be solved easily by adding a sampling point at the cutoff distance with the fixed value of 0. The spline interpolation makes sure that the potential and its derivative go smoothly to zero.

If an analytic potential is cut off at a certain distance, neither its value nor its derivative will be zero in general. There are different solutions, the simplest one is to shift the potential by the negative value at the cutoff distance. Doing so removes the discontinuity of the function itself but not of the derivative. Another possibility is to replace the potential for all distances greater than δr_c with a parabola. The parameter δ has to be chosen in such a way, that the connection at δr_c is continuously differentiable. Determining δ is very difficult for a fixed cutoff radius. The first analytic version of *potfit* was implemented with a fixed value of δ, which lead to a

varying cutoff radius. To guarantee the cutoff distance entered by the user, a cutoff function $\Psi(r)$ is introduced. It is shown in Fig. 6.8. At each sampling point, the potential is multiplied with the cutoff function, the result is the effective potential used in the force calculation.

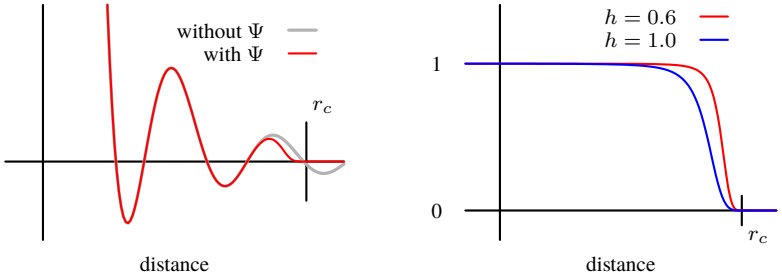

Figure 6.8: Left: Oscillating pair potentials with a cutoff distance r_c. The gray potential has no cutoff function, it is simply cut off, leading to a discontinuity at r_c. The red curve is equal to the gray potential multiplied with the cutoff function $\Psi(r)$. Right: Plots of the cutoff function $\Psi(r)$ with two different parameters h. It determines from where on the potential is smoothed.

The functional form of $\Psi(r)$ used in *potfit* is taken from Mishin *et al.* [82]. It is defined as

$$\Psi(x) = \begin{cases} \frac{x^4}{1+x^4} & \text{for } r < r_c \\ 0 & \text{for } r > r_c \end{cases}, \qquad \text{where} \qquad x = \frac{r - r_c}{h}. \tag{6.25}$$

The parameter h determines the width of the smoothing, r_c is the cutoff distance. For small distances the function has a value of 1. At larger values, close to the cutoff, it decreases gradually until it reaches zero exactly at r_c. The high order of x^4 also guarantees that the derivatives of the potentials goes smoothly to zero. This is important for the spline interpolation, it uses the second derivative to generate continuously differentiable functions.

To enable the smooth cutoff for an analytic potential in *potfit*, the string `_sc` has to be appended to the type identifier. An additional entry at the end of the parameter list is required, which is usually called h. An example for a potential is shown in

Code Listing 6.3.

```
type     lj_sc
cutoff   7
epsilon  0.10 0.00 1.00
sigma    2.50 1.00 4.00
h        1.00 0.50 2.00
```

Code Listing 6.3: Definition of a Lennard-Jones potential with the smooth cutoff option enabled.

With the parameter h added, each potential which uses the smooth cutoff has an additional degree of freedom. The parameter is treated in exactly the same way as a regular parameter. For an analytic potentials defined over distance the smooth cutoff should be enabled. It is enabled for all potentials fitted in chapters 8 and 9, except for the embedding function of EAM and ADP potentials.

6.6.2 Analytic parameters

The implementation of analytic potentials requires special functions for the treatment of the parameters. Most important is the implementation of lower and upper bounds for the parameters. A functional form can yield a reasonable potential with one set of parameters and an unusable one with another set. To remove these inappropriate potentials from the optimization, the parameter space should optimally only include the reasonable potentials. As there is no simple and fast algorithm to test for this, the user has to specify an allowed range for each parameter. There are defaults available for each potential from the `makeapot` utility, which should work in most cases.

After a new parameter has been generated by the optimization algorithms, it is verified that it is inside of the allowed range for that parameter. If it is outside, the potential receives a punishment in the form of an additional contribution to the error sum. The further the new parameter is away from the allowed range, the bigger the punishment. It is calculated from the formula

$$Z_{\text{punish}} = 10^6 x^2, \qquad \text{where} \qquad x = \begin{cases} \alpha_i - \alpha_i^{\max} & \text{if } \alpha_i > \alpha_i^{\max} \\ \alpha_i^{\min} - \alpha_i & \text{if } \alpha_i < \alpha_i^{\min} \end{cases}. \tag{6.26}$$

A parabolic form is chosen to have a small punishment for very small violations

and a steep increase for bigger violations of the predefined parameter range.

It is possible, that the optimal value for a parameter lies outside of the allowed value range. An indication can be if the parameter value after the optimization is equal or very close to one of the boundaries. A subsequent *potfit* run can be started with the respective boundary increased or decreased to get an optimal potential.

An analytic parameter may have special relationships with other parameters or posses special mathematical properties. In *potfit* there are special functions available for both cases. It is possible to evaluate a new set of parameters and adjust it according to predefined rules. An example is a potential, where parameter a always has to be smaller than parameter b. The optimization algorithms alone are not able to fulfill such conditions. The special function checks if all requested conditions are met and adds a similar punishment like Eq. (6.26) if not. The special mathematical properties may be discrete values or periodic parameters. In the later case, the mapping of the parameter to the original period is important to keep the optimization space as small as possible. Typical examples for a periodic parameter are phase factors, which usually have values between 0 and 2π.

In the same way as entire potentials can be excluded from the optimization, single parameters can be kept fixed. If the initial value as well as the lower and upper bound all have the same numeric value, the parameter is removed from the optimization table. This feature can be helpful for adapting already optimized potentials to a different set of reference data, where most of the parameters can be kept fixed and only few need to be adjusted.

Global parameters

For analytic potentials there is another feature available, which can be helpful in different cases. Many analytic potentials from the literature use a single parameter in different functions. In *potfit* these parameters are called "global parameters". If a global parameter is defined, it is assigned to a virtual potential and treated like a regular parameter. Each potential can then access any global parameter, which reduces the number of free parameters for a particular potential. An example for the usage of global potentials in *potfit* is given in Code Listing 6.4.

To define a global parameter a new section has to be inserted in the potential file. It has to be placed directly after the header, in front of the potentials. The keyword for the section is `global`, followed by the number of global parameters. Each parameter is specified like a regular parameter with value, lower and upper boundaries. To use a global parameter in a potential, the same name followed by an exclamation mark is required. The mapping of these parameters is done by name,

```
global   1
h        1.00 0.50 2.00

type     lj_sc
cutoff   7
epsilon  0.10 0.00 1.00
sigma    2.50 1.00 4.00
h!
```

Code Listing 6.4: Usage of a global parameter in *potfit*.

each global parameter name has to have a unique name.

A common application for global parameters feature is shown in Code Listing 6.4. The cutoff parameter h of the smooth cutoff can be defined as a global parameter. All potentials can then use the same cutoff function with a single parameter. The resulting reduction of the number of free parameters also leads to a reduced optimization space.

6.6.3 Available potential functions

The number of analytic potential functions is incredibly large. While many of them are very similar, there are always little differences which are supposed to make them more appropriate for one or another problem.

If a particular potential is missing in *potfit*, it can be added with very little effort. The program has to be altered only at two different places. First, the potential identifier as well as the number of parameters have to be defined. Second, the analytic function has to be implemented as a standalone C-function which takes the distance and the parameters as input and returns the potential value.

In *potfit* there are about 35 different functions implemented, they are all documented in detail on the homepage. The potentials that have been used for the CMAs are introduced in the following paragraphs.

Pair potentials

The functional forms of the pair potentials used in EAM and ADP potentials is called “empirical oscillating pair potential” (EOP). It has been successfully used

for different intermetallic and quasicrystal systems [81]. The potential is defined as

$$\phi(r) = \frac{C_1}{r^{\eta_1}} + \frac{C_2}{r^{\eta_2}} \cos(kr + \varphi) \tag{6.27}$$

with the six free parameters $C_{1,2}$, $\eta_{1,2}$, k and φ. The short range repulsion is covered by the first term, the first minimum as well as any oscillations can be attained with the second term. That makes the function very flexible. Depending on the choice of parameters, it can model very different potentials. It is possible the have a single minimum, a repulsive shoulder or minima for the second and third neighbors. EOP potentials with different parametrizations are plotted in Sec. 8.3.

For comparison, the very simple Morse potential has been used. It is used in the following parametrization:

$$\phi(r) = D_e \left[1 - \exp(-a(r - r_0))\right]^2 . \tag{6.28}$$

The three parameters D_e, a and r_0 determine the depth, the width and the position of the minimum of the potential. With this functional form it is not possible to model a purely repulsive potential or second and third neighbor minima.

Transfer functions

To model the transfer function in EAM and ADP potentials, a function proposed by Chantasiriwan and Milstein [25] has been used. They showed that oscillations in the transfer function are necessary for a potential to yield the correct higher-order elasticity. The function is defined as

$$\rho(r) = \frac{1 + a_1 \cos(\alpha r) + a_2 \sin(\alpha r)}{r^\beta}, \tag{6.29}$$

where α and β are positive parameters, responsible for the frequency of the oscillations and the strength of the decay, respectively. The expression is similar to the form representing Friedel oscillations, $\rho(r) = \lambda \cos(2kr + \delta)(r/r_1)^{-3}$. Equation (6.29) provides more flexibility by not fixing the decay at $\beta = 3$.

For computational reasons a second form of this potential has been implemented. It uses addition theorems to remove the second trigonometric function:

$$\rho(r) = \frac{1 + a \cos(\alpha r + \varphi)}{r^\beta}. \tag{6.30}$$

As a simple alternative for the transfer function, an analytic decay and an exponential decay can be used. This type of function was used by the first EAM models in the 1980s by Johnson [55].

Embedding functions

In 1984 Rose *et al.* [101] developed an universal equation of state for metals. Today it is used in many EAM potentials, with only slight modifications. The version which is implemented in *potfit* has been proposed by Banerjea and Smith [8]. It has the following form:

$$U(n) = -U_0 \left[1 - \gamma \ln n\right] n^{\gamma} + U_1 n. \tag{6.31}$$

ADP dipole and quadrupole potentials

For the dipole and quadrupole functions there is not much data available in the literature. Mishin *et al.* used simple exponential decays in the original publication. To be more flexible, the functions of Chantasiriwan and Milstein (6.30) have been used in this work.

6.7 Testing a potential

The most important step in fitting an effective potential is the testing of its properties. After *potfit* has finished the optimization process, the quality of the potential in general and for specific applications has to be determined. There are several ways of testing a potential which will be presented in this section. The order is from very general tests to very specific applications.

potfit error sum

A first indication for the quality of a potential is directly given by *potfit*. Before the program is terminated, an error report is created which contains information about the deviations of the final potential from the reference data. An example is shown in Code 6.5.

The objective of the optimization algorithm, the total error sum, is given at the beginning of line 2. Additionally, the individual contributions are presented in detail on lines 3 to 5. While these numbers can provide a rough estimate of the

```
1 ###### error report ######
2 total error sum 519.640133, count 11059 (10200 forces, 98 energies, 588 stresses)
3 sum of force-errors  = 4.937880e+02            ( 95.025% - av: 0.048411)
4 sum of energy-errors = 1.857213e+01            ( 3.574% )
5 sum of stress-errors = 7.103907e+00            ( 1.367% )
6 rms-errors:
7 force   1.316211e-01    (131.621123 meV/A)
8 energy  3.259047e-02    ( 32.590473 meV)
9 stress  1.427852e-02    (  0.089129 MPa)
```

Code Listing 6.5: *potfit* error report after the optimization, taken from a Al-Pd-Mn potential.

quality of the potential, they can also be misleading. A low error sum does not guarantee a reliable potential and a large error sum does not necessarily stand for a bad potential. This is related to the issue of transferability, described in Sec. 6.4.

A more meaningful quantity is the root mean square (RMS). It is given in the error report on lines 7 to 9. For convenience the numbers are converted to common units like meV or MPa. The RMS gives a statistical measure of the deviations from the reference data. These errors can be used to compare the performance of different potentials for the same reference data. Yet they do not provide any information on how the potential behaves in MD simulation or for structures that were not included in the reference data.

Scatter plots

A quick way of getting on overview of all datapoints used for the optimization is a scatter plot. There the values of the effective potential and the *ab initio* reference values are interpreted as points in two-dimensional space. If there is perfect agreement, all plotted points should fall on the identity line. For all other cases the points deviate from it. Fig. 6.9 shows scatter plots for forces, energies and stresses.

With scatter plots global trends in the optimization can be identified quickly. If there is a problem with the potential and the calculated values are all too small, the majority of the points deviates to the left. The distance of a datapoint to the identity line is a direct measure of its deviation, the further it is away, the larger the error is.

For an optimized potential most of the points should coincide with the identity line. In Fig. 6.9 this is the case for the forces and the energies. The stresses however show a global trend to the right, which indicates that the values are too big. For a potential which needs to yield precise stress values, the potential should be refitted

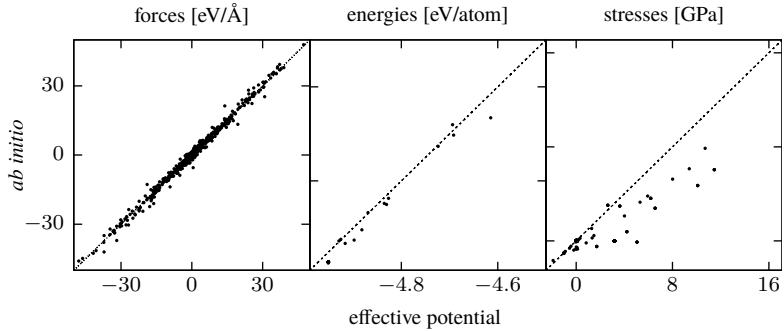

Figure 6.9: Scatter plots for forces, energies and stresses. The value computed with the effective potential is shown on the horizontal axis, the *ab initio* value on the vertical axis. The dashed line is the identity line.

with an increased stress weight.

Split reference data

Checking the fitted potential with other data than the reference data is important for the transferability. Splitting the initial reference dataset into two parts is an common approach. The first part is used for the optimization while the second part is used for the testing. Another source for testing data are *ab initio* MD runs. If some snapshots of the MD trajectory have been used for fitting, other snapshots can be used for testing. To make sure that these snapshots are mostly uncorrelated, they should be a few timesteps apart from each other.

If the errors for the reference and test set are similar, the potential can be regarded as suited for these kind of structures. As a first test for transferability, configurations from different structures can be included in the reference database. As long as the errors are reasonably small, the potential can be tested further in real MD simulations.

"Direct" properties

All previously described tests only use static evaluations of the potential. The next step is to run simple MD simulations. This is done in order to see if the potential can stabilize different structures and yield correct ground state energies.

To test for structural stability, relaxation runs can be performed. The atoms are moved until the residual forces on all atoms are below a predefined threshold. With a good potential, these new positions should only differ marginally from the *ab initio* reference positions.

The structural stability is also of interest at finite temperatures. A simple NVE run for a few thousand timesteps can reveal deficiencies in the potential very quickly. For all temperatures below the melting point the structure should remain stable and neither collapse nor explode.

"Advanced" properties

Depending on the requirements to the potential, some implicit properties can also be checked. The quantities that determine the structure, the forces and energies, can be fitted directly. Advanced properties like the melting temperature, phonon properties as well as the reaction to external perturbations are not a direct part of the fitting process.

These tests are more complex to set up and may require external analysis tools. Some of them are described in chapter 7 and part III.

Specific applications

The final and most important test is the application of the potential to the problem is was fitted to. If the potential is not able to perform a specific task or yields unphysical results, the fitting process has to be restarted with adjusted reference data.

Chapter 7:

Additional methods & computer codes

Modern algorithms for calculating dynamic properties of atomic systems can be very complex. A reasonable approach is to separate the simulation part from the analysis part. Each program can be specialized for the individual tasks without any tradeoffs. It has also the advantage that an analysis tool can be used by different simulation codes as long as there is a common data format.

For the present work different analysis tools have been used. In the following sections the programs for calculating phononic properties like the density of states, dispersion relation and the thermal conductivity will be discussed. Some of them are available on the internet, distributed under an open source license, while others were implemented by the author.

7.1 Phonon density of states

To calculate the phonon density of states (PDOS) there are different approaches. The direct calculation from the trajectories of the atoms requires a few ten thousand timesteps and a large simulation box. A task which can be easily handled with molecular dynamics, for *ab initio* simulations this method is not feasible. Using the harmonic approximation to calculate the dynamical matrix is another possibility. It only requires small samples and uses static configurations, which can be managed with DFT codes.

Direct calculation

Performing an MD simulation for the direct calculation of the phonon density of states (PDOS) is rather simple. First a supercell of the atomic structure has to be created. It should be big enough to eliminate finite size effects. For the clathrate systems a $5\times5\times5$ supercell has been used. After an initial thermalization stage of about $10\,000$ steps, the actual simulation is started. It is a regular NVE run with $200\,000$ steps, where the positions and velocities of the atoms are stored every 10 steps. To save disk space and for easy processing a binary format is used.

The calculation of the phonon density of states is done with the nMOLDYN[1] program, created by Róg *et al.* [100]. It is especially designed for the computation and decomposition of neutron scattering spectra, but it can be used for other quantities.

To be able to import simulation data into nMOLDYN, it has to be converted to the NetCDF[2] data format. There is a python script that comes with IMD, that can do the conversion from the binary data file created during the MD run to the NetCDF format.

The density of states is calculated in two steps. First the velocity autocorrelation function (VACF) is computed. It is defined as:

$$C_{vv} = \frac{1}{N}\sum_{\alpha=1}^{N} w_\alpha \frac{1}{3}\langle \boldsymbol{v}_\alpha(0)\cdot\boldsymbol{v}_\alpha(t)\rangle, \tag{7.1}$$

where w_α is a weighting factor, which is proportional to the mass. The phonon density of states $G(\omega)$ is the Fourier transform of the VACF,

$$G(\omega) = \int_0^\infty dt \exp(-i\omega t) C_{vv}(t). \tag{7.2}$$

There are several parameters that can be adjusted. It is possible to select a subset of the atoms or assign different weighting factors. An important parameter is the "Resolution". It determines the width of the Gaussian, which is used to mimic the finite resolution of experimental detectors. The velocity autocorrelation function is multiplied by the Gaussian and then the result is Fourier transformed to yield the

[1] http://dirac.cnrs-orleans.fr/plone/software/nmoldyn/nmoldyn-2/
[2] http://www.unidata.ucar.edu/software/netcdf/

phonon density of states. A comparison of a PDOS with and without this Gaussian is shown in Fig. 7.1.

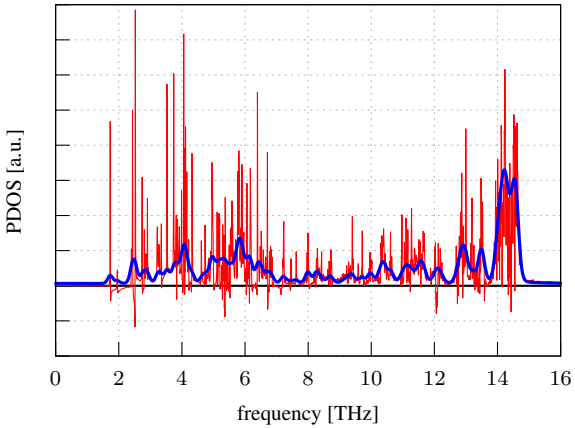

Figure 7.1: Two phonon density of states calculated from the same VACF. The blue curve is smoothed by multiplying a Gaussian before the Fourier transform.

The width of the Gaussian determines how smooth the function will be. For a small resolution value, single peaks can still be distinguished. This is not the case for larger values where several peaks are merged into a broad single peak. The parameter has to be given in a percentage of the total trajectory length. For an MD run with $200\,000$ steps and a timestep of 0.1 in IMD units a reasonable value is between 0.1 and 1.

Dynamical matrix calculation

A different approach, which requires significantly less force calculations, uses the dynamical matrix **D**. In harmonic approximation it can be obtained from the atomic force constant matrices Φ, which can be written as

$$\Phi_{\alpha\beta}\begin{pmatrix} jj' \\ ll' \end{pmatrix} = -\frac{F_\alpha(jl)}{u_\beta(j'l')}. \tag{7.3}$$

The subscripts α and β denote the Cartesian components, j and j' the atoms and l and l' the unit cells. F is the force acting on an atom and u the atomic displacement from the equilibrium position.

The dynamical matrix is then given by

$$\mathbf{D}_{\alpha\beta}(jj', \boldsymbol{k}) = \frac{1}{\sqrt{m_j m_{j'}}} \sum_{l'} \Phi_{\alpha\beta} \begin{pmatrix} jj' \\ ll' \end{pmatrix} \exp(i\boldsymbol{k}[\boldsymbol{r}(j'l') - \boldsymbol{r}(j0)]). \quad (7.4)$$

Here m_j is the mass of atom j, $\boldsymbol{r}(j'l')$ is the position of atom j' in unit cell l' and $\boldsymbol{k}$ is the wave vector. The phonon frequencies ω and eigenvectors $\boldsymbol{e}$ can be calculated from

$$\omega^2 \boldsymbol{e}(\boldsymbol{k}, \nu) = \mathbf{D}(\boldsymbol{k}) \boldsymbol{e}(\boldsymbol{k}, \nu), \quad (7.5)$$

where ν is the label of the solution.

The finite displacement method is implemented in the `phono.py` code from Togo *et al.* [116]. The algorithm is explained in detail in the manual on the homepage[1].

Before calculating a PDOS, the considered structure has to be relaxed. Subsequently `phono.py` can create the necessary displacements from the equilibrium positions of the atoms. For each symmetry inequivalent direction of each Wyckoff position a structure is generated. The forces in these configurations have to be calculated with *ab initio* methods. Afterwards the output is collected by `phono.py` and written into a single force file. From this file the dynamical matrix can be computed. Different phonon related properties like the PDOS can then be extracted.

The effort of this method depends on the number of atoms and the symmetry of the unit cell. For a clathrate system with an empty cage, e.g. Ge_{46}, there are 46 atoms in the unit cell. The space group $Pm\bar{3}n$ has 12 Wyckoff position, of which 3 are occupied. A total of 8 symmetry inequivalent displacements are necessary, resulting in 8 force calculations. For the $2\times2\times2$ supercell structure of Ba_8Ge_{43} with 408 atoms, 26 displacements are necessary.

7.2 Phonon dispersion curves

Closely related to the phonon density of states are the phonon dispersion curves. They give the wave vector dependence on the phonon frequencies for different directions in k-space. Experimentally these dispersions can be measured indirectly via

[1] http://phonopy.sourceforge.net/

the interaction of lattice waves with other waves. Often inelastic neutron scattering is used, another possibility is electron energy loss spectroscopy.

For theoretical analysis, the dispersion curves can be calculated from the dynamical matrix. The `phono.py` program, presented in Sec. 7.1, can be used to compute the phonon dispersion. The density functional perturbation theory (DFPT) provides another method to calculate the dynamical matrix. It uses the linear response theorem and yields accurate results. DFPT is not available in the version of the VASP code used for this work, hence the `phono.py` code is used.

Phonon dispersions from molecular dynamics simulations

For MD simulations it is possible to obtain the phonon dispersion from the VACF (Eq. (7.1)), yet such an approach is not as straightforward as for the PDOS. In 2011 Kong [63] presented a method to calculate the dynamical matrix from an ordinary MD run. It is implemented in the `fix_phonon`[1] package, which is available for LAMMPS.

Instead of determining the force constants Φ from finite displacements, the lattice Green's function coefficients G are used. They can be obtained from the second moments of the displacements:

$$G_{\alpha\beta}\begin{pmatrix} jj' \\ ll' \end{pmatrix} = \langle u_\alpha(jl) u_\beta(j'l') \rangle. \tag{7.6}$$

The force constants Φ are related via

$$\Phi_{\alpha\beta}\begin{pmatrix} jj' \\ ll' \end{pmatrix} = k_\mathrm{B} T G^{-1}_{\alpha\beta}\begin{pmatrix} jj' \\ ll' \end{pmatrix}. \tag{7.7}$$

Usually the analysis is done in reciprocal space, where the displacements are defined as the Fourier transform:

$$\tilde{\boldsymbol{u}}_j(\boldsymbol{k}) = \frac{1}{\sqrt{N}} \sum_l \boldsymbol{u}(jl) \exp(-i\boldsymbol{k}\boldsymbol{r}_l). \tag{7.8}$$

The Green's function in reciprocal space is

$$\tilde{G}_{\alpha\beta}(jj', \boldsymbol{k}) = \langle \tilde{u}_{j\alpha}(\boldsymbol{k}) \tilde{u}^*_{j'\beta}(\boldsymbol{k}) \rangle, \tag{7.9}$$

[1] http://code.google.com/p/fix-phonon/

where $*$ denotes the complex conjugate. With $\tilde{\mathbf{\Phi}} = k_\mathrm{B} T \tilde{\boldsymbol{G}}^{-1}$ the dynamical matrix can be written as

$$\mathbf{D}_{\alpha\beta}(jj', \boldsymbol{k}) = \frac{1}{\sqrt{m_j m_{j'}}} \tilde{\Phi}_{\alpha\beta}(jj', \boldsymbol{k}). \tag{7.10}$$

A regular MD simulation can be set up in LAMMPS to measure the atomic displacements. The external analysis tool requires an additional file, which provides the mapping of the atoms in the supercell back to the simple unit cell. It is necessary to evaluate Eq. (7.6), where the indices l and l' denote the different unit cells. While the simulation is running, a binary output file is created with the dynamical matrices. A postprocessing tool can subsequently calculate the phonon density of states, the phonon dispersion curves as well as several other dynamical properties.

7.3 Thermal conductivity

"The thermal conductivity has proven to be one of the most difficult transport coefficients to calculate" – Evans and Morriss [40]

In the literature there are mainly two different approaches to solve this problem. One is the use of nonequilibrium molecular dynamics (NEMD) simulations. These methods are also referred to as "direct methods". The other approach uses statistical mechanics to derive transport properties like the bulk viscosity or the thermal conductivity. It is named after its two original authors, Green-Kubo method. Both methods will be discussed in the following subsections.

7.3.1 Nonequilibrium molecular dynamics methods

The NEMD approach or direct method uses Fourier's law

$$\boldsymbol{J} = -\kappa \Delta T, \tag{7.11}$$

which relates the heat current $\boldsymbol{J}$ to the thermal conductivity κ and the temperature gradient ΔT. The heat current is defined as an amount of energy transferred in a given time through an area perpendicular to the flux direction. It is typically given in units of W/m^2. The thermal conductivity κ in general is a 3×3 tensor. For practical reasons usually only a single component of the tensor is calculated in an MD simulation.

To exploit Eq. (7.11), a nonequilibrium molecular dynamics simulation has to be performed. An external perturbation is introduced and the response of the system is measured. In some cases changes to the equations of motion or the integration scheme may be required.

There are three different methods to calculate the thermal conductivity with Fourier's law. TENENBAUM *et al.* [111] and MICHALSKI [80] impose a temperature gradient on the sample and measure the resulting heat current. The method of MÜLLER-PLATHE [85] does the opposite, it imposes a heat current and measures the resulting temperature gradient.

Some aspects, however, are common for all three methods. The simulation box is always chosen in such a way, that it is elongated in a particular direction. This is the direction in which the thermal conductivity is measured. An example is shown in Fig. 7.2. It is designed to resemble experimental measurements of the thermal conductivity. There a small rod is heated on one end and the temperature is measured at the other end.

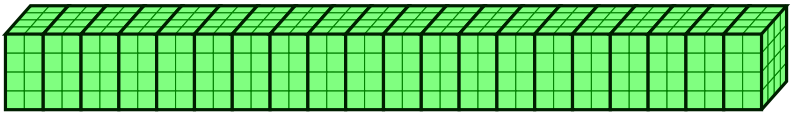

Figure 7.2: Setup of the simulation box for a typical thermal conductivity calculation. The box is divided in layers along the x-axis, indicated by bold lines. Each layer can consist of several unit cells, drawn with thin lines.

Another thing all methods have in common is the use of layers. The simulation box is divided in layers along the x-axis. A single layer can consist of several unit cells as shown in Fig. 7.2. The utilization of these layers is a little different for the different methods. They are explained in the following paragraphs.

Thermal walls

The method of TENENBAUM *et al.* [111] uses the previously described layers to define artificial walls inside the simulation box. They are shown as dashed lines in Fig. 7.3. Two temperatures T_c (cold) and T_h (hot) are defined such that $(T_c + T_h)/2 = T$, where T is the equilibrium temperature. Each wall inside the system is

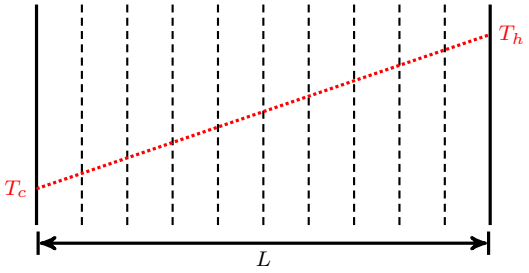

Figure 7.3: Simulation setup for the Tenenbaum method. The cold (left) wall and hot (right) wall define the temperatures for all internal walls of the system.

assigned a temperature, calculated from the interpolation of the previously defined temperatures T_c and T_h. A red dotted line is shown in Fig. 7.3.

An additional force $\boldsymbol{F}_w(\boldsymbol{r})$ is introduced in the equations of motion, which only acts on atoms hitting a wall. Their velocity in x-direction is rescaled according to a Maxwell distribution with the temperature of the corresponding wall. Afterwards the particle is put back into its original layer, with the sign of the velocity changed. The system is forced into a stationary nonequilibrium state, characterized by a thermal gradient.

For each layer k a local temperature T_k can be calculated as

$$T_k = \frac{1}{3n_k k_\mathrm{B}} \sum_{i=1}^{n_k} m_i \boldsymbol{v}_i^2, \tag{7.12}$$

with n_k being the number of atoms in layer k. From these temperatures, the gradient ΔT can be computed. In general it is smaller than the expected value of $\Delta T = (T_h - T_c)/L$.

The heat current $\boldsymbol{J}$ in a molecular dynamics simulation is defined as

$$\boldsymbol{J}(t) = \frac{\mathrm{d}}{\mathrm{d}t} \sum_i \boldsymbol{r}_i \tilde{E}_i, \tag{7.13}$$

where $\tilde{E}_i$ is the difference of the current energy of particle i from its average, $\tilde{E}_i = E_i(r) - \langle E_i \rangle$. There are different ways of computing $\boldsymbol{J}$, Eq. (7.13) can be

rephrased into the following form:

$$\boldsymbol{J}(t) = \sum_i \boldsymbol{v}_i \tilde{E}_i + \sum_{i \neq j} (\boldsymbol{F}_{ji} \cdot \boldsymbol{v}_j) \boldsymbol{r}_{ij}. \tag{7.14}$$

With the temperature gradient ΔT and the heat current $\boldsymbol{J}$ the thermal conductivity can be calculated from Eq. (7.11).

Using a heat bath

The method of MICHALSKI [80] is very similar to the previous one. Instead of active walls, the simulation is coupled to a heat bath. The outer most layers are placed in contact with heat reservoirs of temperatures $T_h = 1.5T$ and $T_c = 0.5T$. In practice simply the velocities of all atoms inside the outer layer is rescaled to the desired temperature. This approach is very easy to implement as it does not require additional terms in the equations of motion.

To maintain a steady temperature gradient, the rescaling has to be performed after each MD step. The heat current $\boldsymbol{J}$ can be calculated in the same way as before, using Eq. (7.14). Another possibility to determine the heat current is through the energy. The amount of energy entering and leaving is related to the heat current via

$$\boldsymbol{J}_x = \frac{\Delta E}{A \, \Delta t}, \tag{7.15}$$

where A is the cross section of the system.

The thermal conductivity can be determined from Eq. (7.11). The temperature gradient is calculated from the different layers using Eq. (7.12). With Fourier's law the conductivity along x-direction is given as

$$\boldsymbol{J}_x = -\kappa \frac{\mathrm{d}T}{\mathrm{d}x}. \tag{7.16}$$

Exchanging the velocities

The third method differs from the previous two in the fact that the heat current is imposed on the simulation and the resulting thermal gradient is measured. It was introduced by MÜLLER-PLATHE [85] and has a considerable advantage. The heat

current vector $\boldsymbol{J}$ is a quantity with large fluctuations. It converges very slowly and large temperature gradients are required to get a noise-free signal. By inducing the heat current it need not be calculated. The temperature gradient on the other hand is a quantity averaged over many particles which usually converges quickly.

The setup is equivalent to the other two NEMD methods. The simulation box is divided into N layers perpendicular to x-direction. For each layer the temperature is defined by Eq. (7.12). To generate the heat current in the simulation, a cool layer ($k = 0$) and a hot layer ($k = N/2$) are defined. In each timestep the velocities of the hottest atom of the cool layer and the coldest atom of the hot layer are exchanged. This mechanism creates an energy transfer from the cool to the hot layer, which induces a heat current from the hot to the cool layer. A schematic simulation box is shown in Fig. 7.4.

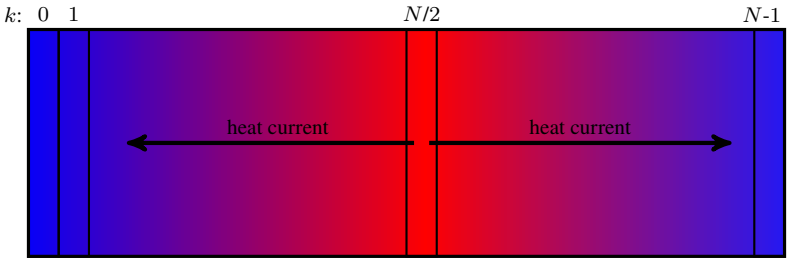

Figure 7.4: Setup of a thermal conductivity simulation according to Müller-Plathe. Energy is transferred from the layer 0 to $N/2$ by exchanging velocities of particles. A heat current from the hot to the cool layer is induced. The special arrangement is due to the periodic boundary conditions.

The spatial arrangement is needed to make this method work with periodic boundary conditions. The right end of the simulation box is connected to the left end. Putting the hot layer on the right end would directly connect it to the cool layer. By putting it in the middle, the energy can flow off in two directions, ending up in the same cool layer. Periodic boundary conditions have the advantage, that most conservation laws are fulfilled without additional effort. Changing the velocity of two atoms preserves the total linear momentum, the total kinetic energy and the total energy. Implementing the Müller-Plathe method into an existing MD code is straightforward.

For two reasons the implementation of this algorithm in IMD is slightly different than in the original publication. First, it is very expensive to find the atoms with the

lowest/highest kinetic energy inside a layer. For large systems with a few thousand atoms per layer this can slow down a simulation significantly. The other reason is also connected to the size of a single layer. By exchanging the velocities of two atoms, the energy exchange is very small. To reach a steady state, the system thus requires very long simulation times.

Both of these problems can be solved by rescaling the velocities of all atoms inside the hot and cool layers. The rescaling factor is calculated as

$$\Delta v_k = \sqrt{1 \pm \frac{\Delta E}{E_k}}, \qquad \text{where} \qquad \Delta E = 2A\,\Delta t\, j_x. \tag{7.17}$$

The plus and minus sign are used in the hot and cool layer, respectively. The surface area $A = L_y \cdot L_z$ has to be counted twice, the energy can flow off in two directions. The heat current in x-direction, j_x, is a fixed value, specified by the user.

The simulation output data yields a temperature gradient, which can be used to determine the thermal conductivity κ with Eq. (7.11). A typical progress of the temperature gradient is shown in Fig. 7.5.

In the beginning of the simulation the temperature is almost constant over all layers. Only for the cooled and heated layers there is a difference. After 125 ps the temperature in the outer layers has started to decrease noticeably. After 750 ps an almost steady temperature gradient is present over the entire sample. It only changes slightly until the end of the simulation. To calculate the value of the gradient, only the inner layers' temperatures are used. The outermost three layers are neglected, they are too much under the influence of the energy exchange. Which layers are used to calculate the gradient depends on the total number of layers, their thickness as well as the imposed heat current. From the average temperature gradient the thermal conductivity can be calculated with Eq. (7.11).

7.3.2 The Green-Kubo approach

A different method of measuring the thermal conductivity is with the Green-Kubo relations. In the 1950s Green and Kubo independently published a theory relating transport coefficients and autocorrelation functions [45, 46, 68]. For the thermal conductivity one can measure the fluctuating heat current and then calculate its autocorrelation function.

To determine the thermal conductivity in the Green-Kubo formalism the auto-

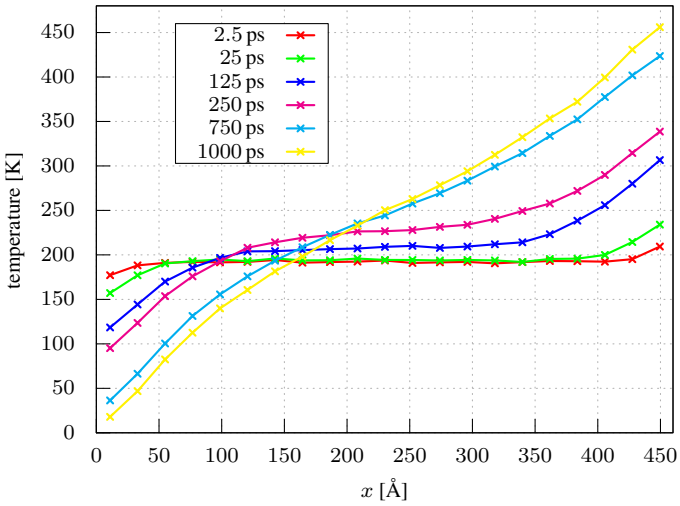

Figure 7.5: Temperature distribution along the x-direction in a Müller-Plathe simulation at different time steps. The simulation box with a length of 877 Å is divided into 40 layers. Each of the 21 unique layers from $k = 0$ to 20 is shown in the plot.

correlation of the fluctuating heat current is integrated:

$$\kappa = \frac{1}{3Vk_{\mathrm{B}}T^2} \int_0^\infty \langle \boldsymbol{J}(t) \cdot \boldsymbol{J}(0) \rangle \, dt, \tag{7.18}$$

where $\boldsymbol{J}$ is defined as in Eq. (7.13). The single particle energy E_i consists of the kinetic energy $\boldsymbol{p}_i^2/2m_i$ and the potential energy V_i. The partitioning of the total energy onto the single particles is only unique for pairwise interactions. It could be shown that for manybody interactions this partitioning does not affect the results [72].

Equation (7.18) averages over all three components of the heat current vector. To compute the thermal conductivity for a specific direction only on component of the heat current is needed. The factor $\frac{1}{3}$ in the coefficient can then be omitted. The other components of the tensor of thermal conductivity can be computed with a

simulation box with the corresponding principle axes.

For an efficient computation of the heat current $\boldsymbol{J}$, it can be expressed in quantities often used in MD simulations.

$$\boldsymbol{J}(t) = \frac{\mathrm{d}}{\mathrm{d}t} \sum_i \boldsymbol{r}_i \tilde{E}_i = \sum_i \boldsymbol{v}_i \tilde{E}_i + \sum_i \boldsymbol{r}_i \dot{E}_i, \tag{7.19}$$

where

$$\dot{E} = \boldsymbol{v}_i \cdot \boldsymbol{f}_i + \sum_j (\nabla_{\boldsymbol{r}_j} V_i) \cdot \boldsymbol{v}_j = -\sum_j (\nabla_{\boldsymbol{r}_i} V_j) \cdot \boldsymbol{v}_i + \sum_j (\nabla_{\boldsymbol{r}_j} V_i) \cdot \boldsymbol{v}_j. \tag{7.20}$$

Putting this into the second part of Eq. (7.19) yields

$$\sum_i \boldsymbol{r}_i \dot{E}_i = -\sum_{i,j} \boldsymbol{r} (\nabla_{\boldsymbol{r}_i} V_j) \cdot \boldsymbol{v}_i + \sum_{i,j} \boldsymbol{r}_i (\nabla_{\boldsymbol{r}_j} V_i) \cdot \boldsymbol{v}_j, \tag{7.21}$$

which can be expressed as

$$\sum_i \boldsymbol{r}_i \dot{E}_i = \sum_i \left[\sum_j (\boldsymbol{r}_j - \boldsymbol{r}_i) \otimes (\nabla_{\boldsymbol{r}_i} V_j) \right] \cdot \boldsymbol{v}_i = \sum_i \boldsymbol{W}_i \cdot \boldsymbol{v}_i. \tag{7.22}$$

$\boldsymbol{W}_j$ is the partitioning of the total virial tensor onto the individual particles. With this, Eq. (7.19) can be written as

$$\boldsymbol{J}(t) = \sum_i \left(\tilde{E}_i + \boldsymbol{W}_i \right) \cdot \boldsymbol{v}_i. \tag{7.23}$$

This is the formula that is used by IMD to compute the heat current. The single particle virial $\boldsymbol{W}_i$ is also needed for calculating the stress tensor and can be accessed without any additional effort.

Running a Green-Kubo simulation with IMD requires three parameters. The average energy $\langle E_i \rangle$ has to be determined before the calculation of the heat current. The parameter `hc_av_start` sets the timestep for the start of the averaging process. It should be big enough to thermalize the entire sample. The first phase is terminated when `hc_start` timesteps are reached. The evaluation of the heat current is then performed until the end of the simulation. It is written to an output file every `hc_int`

steps. For calculating the autocorrelation function and the thermal conductivity postprocessing tools have to be used.

Processing the output data

The output file of IMD contains the heat current $\boldsymbol{J}$ at the discrete timesteps, defined by the `hc_int` parameter. To obtain the thermal conductivity κ, the autocorrelation of the heat current has to be integrated, cf. Eq. (7.18). The heat current autocorrelation function (HCACF) can be calculated quickly using the fast Fourier transformation (FFT) method. The integral of the autocorrelation is subsequently calculated with another script, using the Simpson rule.

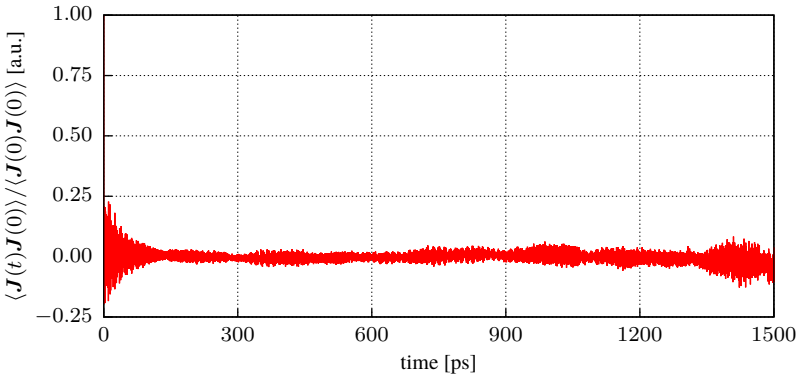

Figure 7.6: Normalized autocorrelation function of the heat current $\boldsymbol{J}(t)$ in a single Ge_{46} simulation.

The Green-Kubo method works well for liquids, where it yields reliable results. For solids, there is usually a problem with the convergence of the integral. A typical autocorrelation function for a solid system is shown in Fig. 7.6.

The function looks as expected in the first 200 ps. There is a large value at $t = 0$ which then decays at an exponential rate. From 300 ps on there are oscillations, which are getting bigger with increasing time. In numerical simulations the autocorrelation function is cut off at a certain time, when the correlation function is virtually zero. That is not possible for solid systems. The correlation function does not vanish as expected. The fact that the values are increasing for large times is caused by the numerical calculation of the autocorrelation function and can safely be ignored.

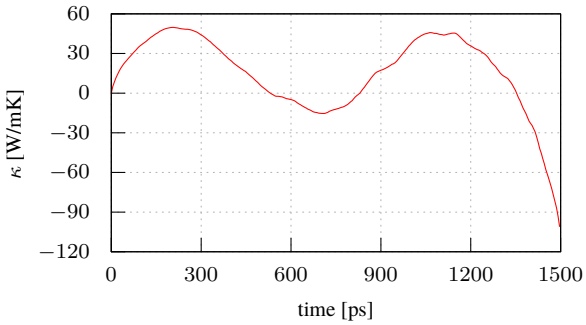

Figure 7.7: Integrated autocorrelation function of the heat current $\boldsymbol{J}(t)$ in a single Ge_{46} simulation.

The integral of the autocorrelation function of the heat current has to converge to yield a reasonable value for the thermal conductivity. When integrating the function shown in Fig. 7.6 this is not the case. The thermal conductivity does not converge, the integral diverges for large times (shown in Fig. 7.7).

To obtain reasonable values from the Green-Kubo method additional considerations are necessary. In contrast to the direct method, this is a statistical approach. Instead of looking at a single simulation, the average over several simulations should be considered. In Fig. 7.8 the average autocorrelation functions for 20 and 50 runs are shown. They look very similar to the single run function for small times. The oscillations at greater times, however, are almost completely averaged out.

But even for the averaged autocorrelation functions the integral does not converge. For both functions of Fig. 7.8 the integral is shown in Fig. 7.9. For times smaller than 50 ps the values almost match perfectly. Afterwards the average of the 50 runs is bigger until they are more or less identical again for $t > 400$ ps.

In the literature there are different approaches on how to get meaningful results with the Green-Kubo formalism. The most simple solution is to define some cutoff time t_c, after which the autocorrelation function is assumed to be zero. However there is no justification for this method. The cutoff would have to be chosen manually for each run, depending on the integrated autocorrelation function.

Another common solution is to approximate the autocorrelation with another function, which does decay to zero. Usually the function accounts for an exponential decay as well as oscillations. Dong *et al.* [32] use the following function to calculate

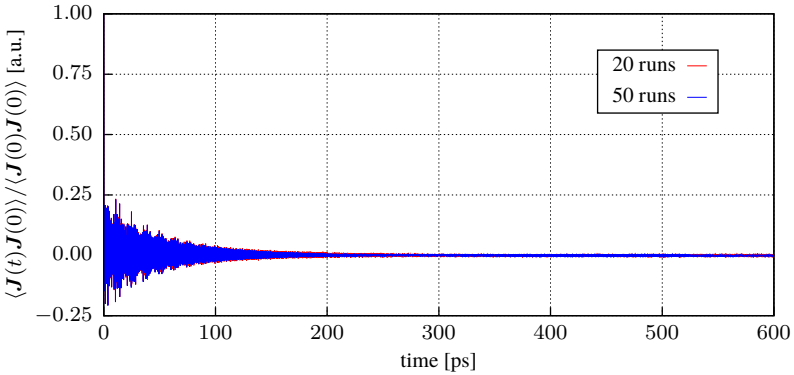

Figure 7.8: Averaged normalized autocorrelation function of the heat current $\boldsymbol{J}(t)$ of Ge_{46} for 20 and 50 runs.

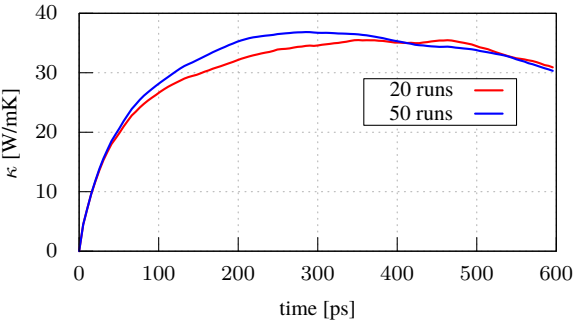

Figure 7.9: Integrals of the averaged HCACF shown in Fig. 7.8.

the thermal conductivity in different phases of Germanium:

$$g(t) = A_0 \exp(-t/\tau_0) + \sum_j B_j \exp(-t/\tau_j) \cos(\omega_j t). \tag{7.24}$$

A different function, that also takes the different wavelengths of the acoustic, short range, long range and optical modes into account is used in [78]. Very similar is the method of Bernstein *et al.* [15]. There the real integral of the autocorrelation is calculated up to a certain point in time. After that point the autocorrelation is replaced by an exponential decay. Both of these approaches lead to reasonable results, however they both require manual adjustments and may introduce considerable errors by replacing the autocorrelation functions with approximations.

Another way of calculating the thermal conductivity from the autocorrelation function of the heat current is used by Lee *et al.* [72]. Instead of taking the real-space operator $\boldsymbol{J}(t)$, its Fourier transform, defined by

$$\boldsymbol{S}(\omega) = \int_0^\infty dt\, \boldsymbol{J}(t) \exp(i\omega t) \tag{7.25}$$

is used. The temperature-dependent thermal conductivity is the zero-frequency limit of the frequency-dependent $\kappa(\omega, T)$,

$$\kappa(T) = \kappa(\omega, T)|_{\omega=0} = \frac{1}{3Vk_\mathrm{B}T^2} |\boldsymbol{S}(\omega)|^2_{\omega=0}. \tag{7.26}$$

The problem for this approach is the integral in Eq. (7.25), which has to be calculated up to infinity. MD simulations end after a finite amount of time, thus again an artificial cutoff time is introduced, which is determined by the length of a simulation.

For the calculations performed in the present work a different method has been used, which will be explained in the following paragraphs.

Integral averages The method chosen for the present work takes into account the statistical origin of the Green-Kubo relation. Several MD runs are carried out, which only differ in the seed for the random number generator. The initialization of the velocities according to a Maxwell distribution is different for each run, resulting in different trajectories for all particles. Instead of averaging over the autocorrelation of the heat current of every run, the integrals of the individual runs are averaged.

For each discrete time t, it is possible to indicate an error, calculated as the standard deviation of all individual integrals. An example for 20 runs is shown in Fig. 7.10.

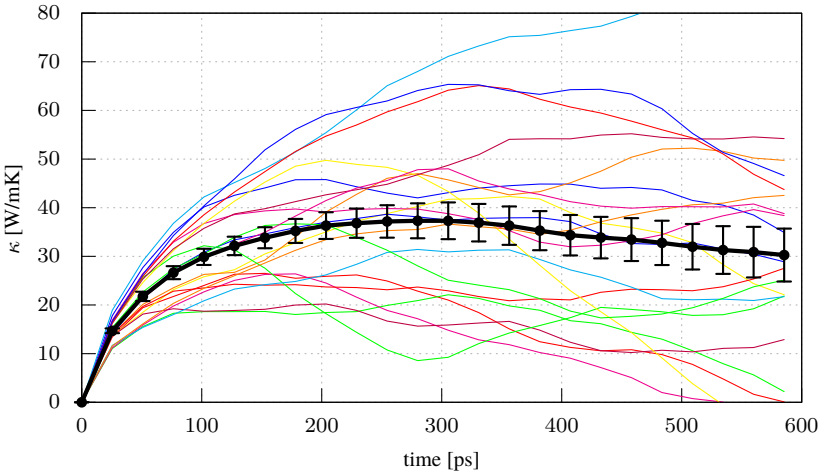

Figure 7.10: Averaging over multiple integrated autocorrelation functions. The individual runs are shown with thin lines. The average is drawn in black with error bars.

To determine the value of the thermal conductivity the first plateau of the integral has to be identified. One possibility is a script, which determines the gradient of the integral. If the gradient is smaller than a predefined threshold for a certain amount of timesteps, the plateau is found. Such routines usually yield poor results for non-well behaved functions. In the present work the plateau region is identified manually. The range of the plateau is passed to a script, which then determines the thermal conductivity. From the standard deviations of the individual runs an average over the plateau is calculated.

In Fig. 7.10 one possible choice for the plateau is between 200 and 300 ps, where the integral has an approximate value of about 37. Using the analysis script yields a range from 33.878 to 38.891, which results in a total value for the thermal conductivity of 36.4 ± 2.5 W/mK.

7.3.3 Comparison

Both methods presented here, the NEMD Müller-Plathe and the EMD Green-Kubo method, have some disadvantages. A short comparison is given in Tab. 7.1.

The first point is the way the thermal conductivity is calculated. In the direct methods, the actual temperature of the sample is used to calculate a thermal gradient. The Green-Kubo method uses a statistical approach and does not rely on a thermal gradient. Looking at the scales of Fig. 7.5, one can determine the problem of the direct approach. There is a temperature gradient of $100\,\mathrm{K}$ on a length of about $450\,\text{Å}$. This corresponds to $2.2 \times 10^9\,\mathrm{K/m}$, a value that can never be reached in experiment. Due to the huge gradient, the results of the direct method have to be regarded with caution. They depend strongly on the potential and can be off by several orders of magnitude. As this problem is inherent to the direct method, the effect can only be weakened by choosing a larger sample but not removed from the simulation.

	Müller-Plathe	Green-Kubo
Calculation	direct	statistical approach
Integrator	special (NVX)	NVE
Simulation type	NEMD	EMD
Sample size	big	small
# of simulations	1	> 10

Table 7.1: Comparison of different aspects of the direct method for calculating the thermal conductivity and the Green-Kubo method.

The second point concerns the implementation of the different methods into existing molecular dynamics simulation packages. Here both methods require about the same amount of work. For the direct method the integration scheme has to be changed while the output can be taken from existing functions. The Green-Kubo method does not require any changes to the integrator, here the atomic properties like energies and velocities have to be used to calculate the heat current for each time step.

An important difference is the simulation type. The direct method uses a nonequilibrium simulation while the Green-Kubo method can be performed in an equilibrium run. This is especially important when choosing the interatomic potentials. If they are not fitted explicitly for different temperatures the results of the direct method is unpredictable. In equilibrium simulations most potentials can be used

and are able to yield reliable results with the Green-Kubo method.

When performing thermal conductivity simulations, the size of the simulation box is very important. The direct method requires a large cell compared to the Green-Kubo method. It has to be big enough to allow a constant thermal gradient to develop between the heated and cooled layers. Usually it should be at least 100 Å long, depending on the size of a unit cell. The size of the directions perpendicular to the heat current should also be at least 2 unit cells, to allow for a meaningful temperature definition in each layer. For the Green-Kubo method, the size of the simulation cell should be big enough to provide enough statistical data. Usually a few thousand atoms are enough; the direct method requires a few hundred thousand. For a single simulation with the same amount of time steps the Green-Kubo method requires a lot less computational effort than the direct method.

Because of the statistical approach to the thermal conductivity, the number of simulations required to get a reliable result is on the order of 10 to 50. This fact, together with the large samples required for the direct method, makes the computational efforts required for both methods virtually equal. While the Green-Kubo methods requires many small simulations, the direct approach uses a single simulation with a much larger simulation box.

Experimental results

Although both methods of calculating the thermal conductivity yield reliable results the comparison with experimental values is very difficult. When using molecular dynamics simulations, different aspects have to be considered.

An important point is, that the simulated structure is a perfect crystal with no impurities or defects. In experimental measurements that is not the case. All real crystals have impurities or defects which influence the thermal conductivity. In computer simulations only a very small fraction of a (perfect) crystal can be simulated.

The thermal conductivity obtained from molecular dynamics simulations is not the total thermal conductivity. As described in Sec. 3.3.1, there are contributions from the lattice and from the electrons. In MD simulations the atoms are regarded as point masses which interact according to an effective potential. Electronic interactions are not accounted for. Yet it is possible that some electronic contributions are present in the effective potential through the fitting process. The “effective” thermal conductivity that can be calculated from molecular dynamics simulations is the lattice part with some electronic contributions. For small temperatures this effect should not play an important role, only at higher temperatures the electronic

contributions become considerable.

From experimental measurements the lattice thermal conductivity can be calculated with the Wiedemann-Franz law. The ratio of the electronic contributions to the thermal and electrical conductivity of a metal is proportional to the temperature,

$$\frac{\kappa_e}{\sigma} = LT. \tag{7.27}$$

The proportionality factor L is the Lorenz number, equal to $2.44 \times 10^{-8}\,\mathrm{W\,\Omega\,K^{-2}}$. Measuring the electrical conductivity, the electronic part of the thermal conductivity can be calculated. Subtracting it from the total thermal conductivity yields the lattice part of the thermal conductivity.

While a direct comparison with experiment values is not possible, the relative values can be compared. This can be done for different temperatures or different structures. The trend from the experimental values usually can be reproduced.

Part III.

Simulations and results

Chapter 8:

Potentials for the Al-Pd-Mn system

The ternary intermetallic system Al-Pd-Mn is interesting because of the high number of complex phases it forms. There are several binary Al-Pd and Al-Mn phases with small solubilities of the third element. An icosahedral quasicrystal as well as two decagonal quasicrystals with their approximants can also be found. The subject of this work are the approximants of one of the two decagonal quasicrystals. They differ in the lattice constant in the periodic direction, one has 1.2 nm, the other 1.6 nm. The 1.6 nm-phases, also called ε phases, and their approximants are being investigated because they show a novel type of dislocation, a metadislocation. It was first observed under plastic deformation by Klein *et al.* [60] in 1999. Due to the large unit cells and huge number of atoms involved, the atomic structure of the approximants as well as the core of the metadislocation could only be resolved poorly.

In the present work the lowest approximants, ξ and ξ', of the decagonal quasicrystal with 1.6 nm periodicity are used to calculate *ab initio* reference data. An analytic potential is fitted with the *potfit* code and tested thoroughly. Different analytic functions are used, allowing for oscillations on different length scales. These potentials stabilize new structure models of the ε phases and describe their energy with high accuracy.

Parts of this work is based on the author's diploma thesis [P1]. The results have appeared in a publication [P3]. The structure optimization was performed by Frigan and Santana with the help of the fitted potentials [P2].

8.1 Structure model

The first structure model for the ξ'-phases was established by Boudard *et al.* [19] in 1996. It is based on diffraction data gathered from large single crystals. An attempt to describe the structure with a 6-dimensional hyperlattice was made by Beraha [13]. For the use in computer simulations both descriptions have a drawback. There are split positions of aluminum and the transition metal atoms as well as many sites with an occupancy factor smaller than one. To refine the structure model and make it applicable for higher approximants effective potentials are required. The unit cells of the ξ and ξ' phase contain approximately 160 and 320 atoms, respectively, which can still be handled with *ab initio* methods. For larger approximants and the metadislocations more than thousand atoms have to be considered.

Fitting effective potentials and refining a structure model are iterative processes which progress in stages. From an initial structure model a preliminary potential can be created. With the data from this potential the structure model can be refined, which leads to an optimized potential. The cycle can be repeated several times, until there is no more improvement for both the potential and the structure model.

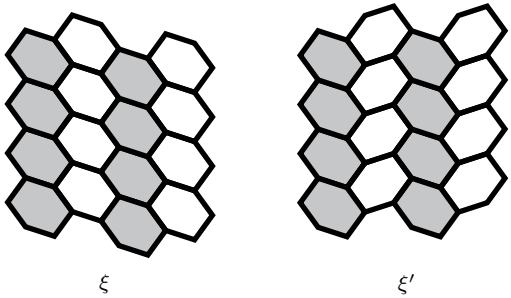

Figure 8.1: Tiling decoration of the ξ and ξ' phases. The gray and white hexagons are equal, they are highlighted for optical reasons. A pseudo-Mackay cluster is located at each vertex of the hexagons.

The basic building blocks of the ξ and ξ' phases, two types of clusters, are explained in the next subsection. Their structure model was refined while the potential fitting was still ongoing. Intermediate structures were used as reference data for the potentials. For a complete understanding of the structure and the optimization process of the potential the final structure will be presented in advance.

Basic building blocks

The structure of the ξ and ξ' phase can be decorated by a single flattened hexagon tile with an edge length of about 7.6 Å. In the ξ phase the hexagons are all aligned in the same direction, whereas in the ξ' phase the orientation alternates. Both decorations are shown in Fig. 8.1. For higher approximants of the decagonal quasicrystal additional tiles are required, e.g. pentagons and nonagons.

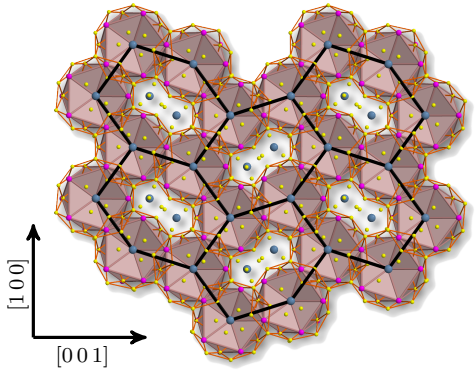

Figure 8.2: Decorated tiling of the ξ' phase. The manganese atoms are shown in blue, the palladium atoms are pink and the aluminum atoms are drawn as yellow spheres.

At each vertex of a hexagon there is a pseudo-Mackay icosahedral (PMI) cluster, as described in Sec. 2.1. The central atom, a manganese atom, is located directly on the vertex, while the surrounding aluminum and palladium atoms form the shells of the cluster. In between the clusters, at the center of the hexagons, there are atoms forming small clusters. A tiling model with the corresponding atomic decoration for the ξ' phase is shown in Fig. 8.2.

In the direction perpendicular to the plane containing the hexagons, the $[0\,1\,0]$-direction, the structure is periodic. The layers are stacked on top of each other with a lattice constant of about 1.6 nm. Columns of PMI clusters are formed, located at the vertices of the hexagons. A simple illustration is given in Fig. 8.3.

The clusters in the center of the hexagons, depicted with a green framework and gray faces in Fig. 8.3, form a so-called large bicapped pentagonal prism (LBPP). They are made up from two almost spherical shells, an inner $Al_{10}Mn_2$ shell and an outer $Pd_{10}Al_{32}$ shell. The LBPP are arranged in a zig-zag pattern along the

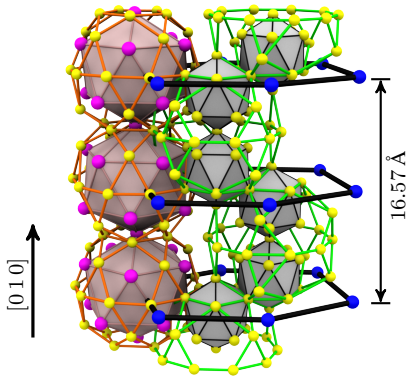

Figure 8.3: Stacking of the clusters is the ε phases. Three of the layers in the periodic direction are shown. For the ξ and ξ' phase there are two different layers with a spacing of about 8 Å. The Pd_{10} pentagonal prisms are omitted from the LBPP.

periodic stacking axis. Only nine atoms of the LBPP cluster are not shared with the neighboring PMI clusters.

After the structure optimization was complete, the original atomic decoration given by Boudard *et al.* [19] was changed slightly. The inner shell of the PMI cluster is occupied by only nine aluminum atoms, which do not form a simple geometric shape. For the LBPP the symmetry is broken by changing the central atoms from manganese to aluminum and palladium. The structure is most stable when the connecting atom between the two inner clusters is a manganese atom. By replacing one aluminum atom from the outer shell with a vacancy, the most stable structure is formed. The optimized inner and outer shells of both clusters are shown in Fig. 8.4.

8.2 Empirical potentials for Al-Pd-Mn

To study the structure of the ε phases with MD simulations reliable effective potentials are required. In a ternary system six potentials for the interaction of the three elements are necessary. For the Al-Al potential there are many parametrizations available for different temperature and pressure ranges. A Pd-Pd potential is also available. The Mn-Mn interaction is the only one missing of the pure potentials.

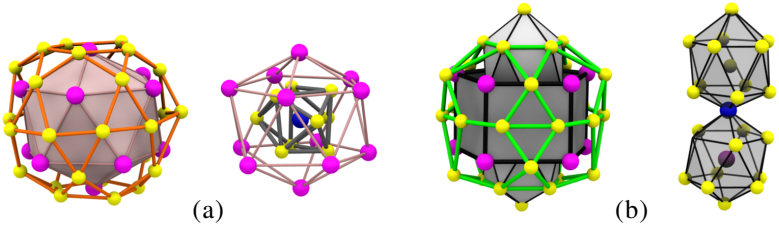

Figure 8.4: Atomic clusters in the ξ and ξ' phases after the structure optimization. (a) PMI cluster (b) LBPP.

For the mixing potentials, the most likely ones to be available are the Al-Pd and Al-Mn potentials, because in these systems there are stable alloys. The Pd-Mn interaction is unavailable, since manganese and palladium do not mix.

One possibility to generate a potential for a ternary system is to use the already available potentials and only fit the missing ones. This approach, however, only works for simple metals. With few atoms in a unit cell and a regular period arrangement, the local structure is almost identical for all atoms. A pure element potential, like Al-Al, can thus still be valid in simple binary compounds. Fitting only the mixing potential Al-X often leads to accurate results.

The atomic structure and the composition are the main reasons why the simple approach usually fails for complex metallic alloys. In the large unit cells with the cluster substructure there usually are several completely different local environments. This affects the pure as well as the mixing potentials and cannot be neglected. In CMAs often one of the elements is present as a minor constituent. The interactions of these elements might differ significantly from the bulk, depending on the neighboring atoms. An effective potential for a 50-50 composition might look completely different than for a 90-10 composition of the same elements.

To create an effective potential for the Al-Pd-Mn system no previously fitted potentials were used. All interactions were fitted from a generalized template potential without any restrictions. The following will give details on the reference data, their generation, as well as on the fitting procedure itself. The analytic functions used for the different potential models are also discussed.

Fitting procedure

The fitting process for the potentials was not performed in one pass. While the structure optimization was not completed, several intermediate potentials were

created. Every time an improved structure was found, the reference database was updated, depending on the performance of the potentials. During that stage only basic tests for the energy and structure stability were performed. For the final potentials a more detailed testing was carried out.

The settings for the parameters of *potfit* were also adjusted during the various optimization runs. The values which are given here are the final values used for all potential models. The energy weight was set to $w_E = 22\,500$, to obtain potentials that yield precise energies but also reasonable forces. For configurations with about 150 atoms, the effective weights of the energies are approximately 50. The stress weight w_S was set to 750. With the six components of the stress tensor, each component is weighted with a factor of 10 when compared to the forces. The weights on the individual configurations are given next to the structure data in the next paragraph.

The cutoff radius r_c was chosen as 7 Å. A PMI cluster has a radius of about 5 Å for the outer shell, this means that the influence of the central atom on the entire cluster is incorporated in the potentials. With the smooth cutoff function the effective cutoff is a little bit shorter, approximately at 6.5 Å.

Reference data

Choosing the appropriate reference data for the potential fitting is not a trivial task. Especially for potentials that shall stabilize structures which are unknown and not included in the reference database. To get reliable data when calculating the stability of the structures the pure phases of the three elements were included, Al.$cF4$, Pd.$cF4$ and Mn.$cI58$.

The binary structures used in the fitting process are given in Tab. 8.1. Most of them are also indicated in the ternary phase diagram in Fig. 8.5. All structures are ground states and are fully relaxed with *ab initio* methods. All residual forces in these configurations are very small and do not contribute much to the fitting process. The only information gained from these structures is their energy and the equilibrium lattice constant. The structure data is taken from the alloy database of Widom and Mihalkovič [121].

Over the course of the potential fitting and the structure optimization the number of available ternary structures steadily increased. In the beginning only few structures, generated with the canonical cell tiling (CCT) approach [51] were available. They have a different structure, yet the atomic composition is close to the ε phases. One configuration of the T phase was included, which has an increased manganese content. As the first results of the structure optimization were available,

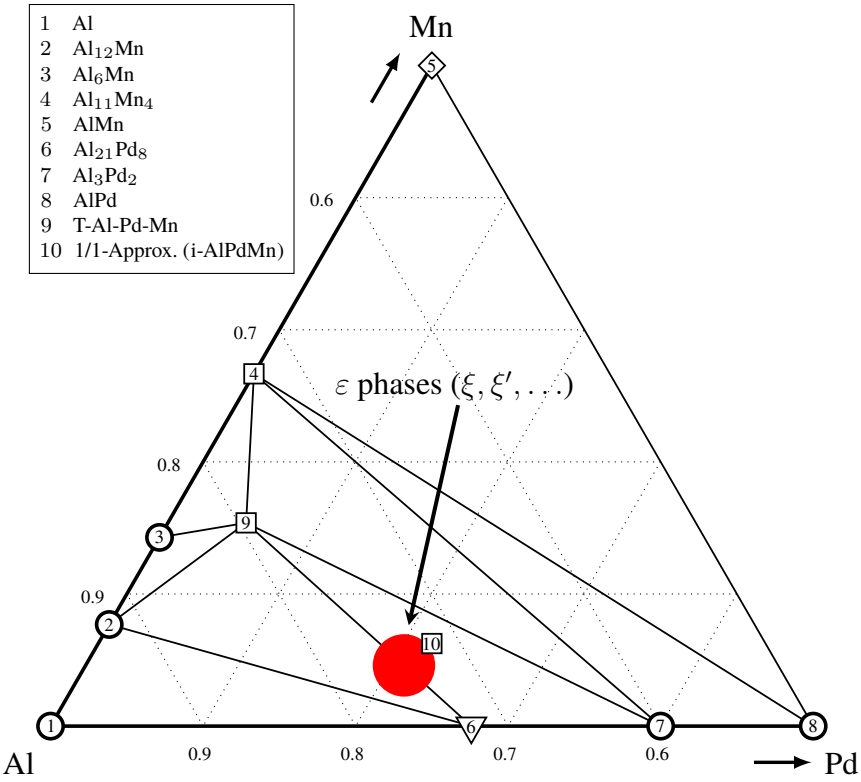

Figure 8.5: Ternary Al-Pd-Mn phase diagram in the Al-rich corner at $T = 0$. Circles label known stable structures, diamonds indicate metastable structures, squares are unknown or unreported structures and triangles correspond to high-pressure phases. The red spot outlines the approximate composition of the ε phases.

Al-Mn structures		Al-Pd structures	
$Al_{10}Mn_3.hP26$	1	$AlPd.cP8$	1
$Al_{11}Mn_4.aP15$	10	$Al_{21}Pd_4.tI116$	10
$Al_{12}Mn.cI26$	10	$Al_3Pd_2.hP5$	10
$Al_6Mn.oC28$	1		
$AlMn.tP4$	1		

Table 8.1: Binary structures used for the Al-Pd-Mn potential fitting. The numbers in the second and fourth column indicate the configuration weights for the preceding structure.

they were added to the reference database. All structures mentioned up to this point are ground states.

To get more data for the force-matching process, MD simulations with a CCT structure were performed. To compensate for the low manganese content and the problems in the fitting process resulting therefrom, five randomly picked aluminum atoms were replaced by manganese atoms in some of the simulations. Three series of MD runs were carried out, at 600, 1100 and 1800 K with small strains applied to the lattice. The melting point of Al-Pd-Mn is at 1116 K, the third dataset is thus from the liquid phase. From each of the three simulations several snapshots were extracted and added to the reference data. An overview of all ternary structures used in the reference database is given in Tab. 8.2.

8.2.1 Different potential models

In the diploma thesis of the author it was shown that for complex structures like Al-Pd and Mg-Zn oscillations are important to model the atomic interactions properly. To verify this for even more complex systems, different analytic models were tested for the Al-Pd-Mn potentials. EAM potentials were used, the functions for the different models are given in Sec. 6.6.3.

The main difference of the three models are the analytic functions. Model I permits oscillations in the pair potential but not in the transfer function. In contrast, model II can have oscillations only in the transfer function. Finally, the third model permits oscillations in both, pair and transfer function. The analytic forms are the EOP potential (Eq. (6.27)) for the oscillating and the Morse potential (Eq. (6.28)) for the simple pair function. As oscillating transfer function the CSW potential is used (Eq. (6.29)), the simple transfer function is represented by a simple exponential

	Configuration	Weight	Comment
$T = 0$	$Al_{92}Pd_{28}Mn_{10}$	1	from CCT
	$Al_{92}Pd_{28}Mn_{8}$	1	from CCT
	$Al_{112}Pd_{36}Mn_{6}$	1	from structure optimization[a]
	$Al_{114}Pd_{34}Mn_{6}$	1	from structure optimization[a]
	$Al_{112}Pd_{34}Mn_{6}$	1	from structure optimization[a]
	$Al_{110+x}Pd_{32}Mn_{8}$	1	from structure optimization[a,b]
	$Al_{124}Pd_{8}Mn_{24}$	10	T-phase
	$Al_{147}Pd_{43}Mn_{18}$	5	ξ-phase[a]
	$Al_{294}Pd_{88}Mn_{16}$	5	ξ'-phase[a]
$T > 0$	$Al_{92}Pd_{28}Mn_{8}$	1	QMD (600, 1100, 1800 K)
	$Al_{92}Pd_{28}Mn_{10}$	5	QMD[a] (1500 K)

Table 8.2: Ternary structures used for the Al-Pd-Mn potential fitting. Structures denoted by [a] were generated in the course of the structure optimization. [b] denotes structures, which have a variable number of atoms in the innermost shell (cf. Tab. 8.6).

decay

$$\rho(r) = \alpha \exp(-\beta r). \tag{8.1}$$

All models use the same embedding function of Rose *et al.* [101] (Eq. (6.31)). The total number of free parameters for all models is given in Tab. 8.3.

For all three potential models the smooth cutoff function, described in Sec. 6.6.1,

	model I	model II	model III	multiplicity
pair	$6+1$	$3+1$	$6+1$	6
transfer	$2+1$	$4+1$	$4+1$	3
embedding	3	3	3	3
total	60	48	66	

Table 8.3: Number of free parameters for the Al-Pd-Mn potential models. The multiplicity gives the potential count for a ternary system. For all pair and transfer functions the additional cutoff parameter is indicated by the $+1$.

is enabled. The number of free parameters for all pair and transfer functions is therefore increased by one.

8.3 Testing the potentials

After the structure optimization was completed, the final potentials were tested for various properties. Besides the basic test for structure stability and accuracy some dynamic properties were also calculated.

Error sums

After the optimization process the total error sums as well as the RMS errors are calculated by *potfit*. The values for all three potential models are given in Tab. 8.4.

RMS errors for	Model I	Model II	Model III
forces [meV/Å]	266.89	247.47	220.07
energies [meV/atom]	20.82	14.50	12.53
stresses [kPa]	100.91	76.04	98.30
total error sum	17 806.51	13 068.23	6550.34

Table 8.4: RMS errors and total error sums after the optimization for forces, energies and stresses, calculated from the reference data.

While the significance of the total error sum is negligible, the RMS errors can be used to judge the potentials. For forces and energies, model I has the largest errors and model III the smallest. For stresses, models I and III are almost identical, model II has the lowest error. Especially the energy error is important for the potentials, if they are to be used in structure optimization. Here the value of model III is almost 50 % smaller than the one of model I.

An optical representation of the force and energy errors is given by the scatter plots in Fig. 8.6. The upper row shows the energy errors, which look almost identical for all three models. In the magnified insets, differences can be seen. The deviations, in agreement with the RMS, decrease significantly from model I to model III. A similar behavior is found for the forces, shown in the bottom row. For model I, the overall shape of the datapoints appears wider with more far off values. The differences in the force RMS between the models II and III is not visible in the scatter plots.

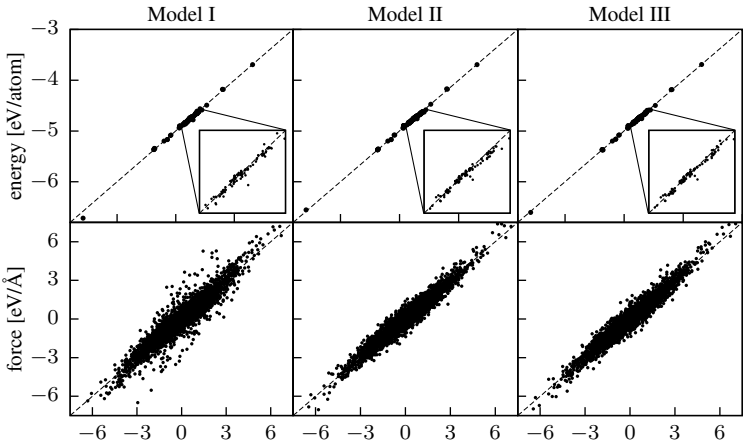

Figure 8.6: Scatter plots for forces and energies. The value computed with the effective potential is shown on the horizontal axis, the *ab initio* value on the vertical axis. The dashed line is the identity line. Insets are scaled by a factor 4.5.

To check the transferability of the potential models, the RMS errors have also been calculated for a different set of configurations. During the structure optimization many similar structures were created, which were not included in the reference database for the potential optimization. There are snapshots of the ξ_1' phase, which can be decorated with hexagons and nonagons, as well as artificial structures that have not been observed in experiment. The results are shown in Tab. 8.5.

RMS errors for	Model I	Model II	Model III
forces [meV/Å]	141.90	131.90	130.46
energies [meV/atom]	10.42	10.47	10.28
stresses [kPa]	32.39	23.76	36.89
total error sum	3007.66	2641.95	2592.26

Table 8.5: RMS errors and total error sums for the testing dataset. None of the structures therein was used in the fitting process of the potentials.

The errors for all three potential models are very similar for the testing dataset,

especially the energy errors. The total values are much smaller than before. In the reference database there are several high-temperature MD runs included, the forces therein can become very large. In the testing dataset only ground state structures are included, which have significantly smaller forces.

Based on the simple error calculations from the optimization process the models cannot be rated. Model I seems to perform a little worse than the other two models, but to make a decision about the quality of the models further test are required.

Structure refinement

During the structure refinement the two types of clusters were optimized with respect to the total energy difference to a convex hull. To judge the stability of different structures, their energy is compared to a mixture of competing phases, which is called the convex hull. It is defined over a ternary phase diagram and contains the cohesive energies of all stable compounds as vertices. If the energy of a structure is below this convex hull, it is considered thermodynamically stable, otherwise it could decompose into the neighboring structures, lowering its energy. The structures defining the convex hull for the ε phases are T-AlPdMn, $Al_{12}Mn$, $Al_{21}Pd_8$, and Al_3Pd_2. They are marked in the phase diagram in Fig. 8.5, where also the convex hull is indicated by black solid lines.

Another important quantity for structure optimization is the formation enthalpy ΔH. It is defined as the difference of the total energy of a system to the hypothetical pure element energy of the same composition. The formation enthalpy can be calculated rather quickly without the need for external tools. Calculating the convex hull on the other hand is done with the QHULL program [9].

The initial structure determination of Boudard *et al.* [19] could not resolve the occupancy of the first shell of the PMI cluster. The number of aluminum atoms is unknown as they are difficult to observe in diffraction experiments. Structures from eight to eleven aluminum atoms per PMI cluster were generated and tested. Since each unit cell of the ξ phase contains four PMI clusters, the average number of atoms is used to denote the different structures.

The energies for all 13 structures are given in Tab. 8.6. All of them are completely relaxed with the respective potentials. For the EAM potentials this leads to small displacements in the structures when compared to the *ab initio* reference data. For model I, the average displacements are 0.10 Å/atom, 0.08 Å/atom for model II and 0.11 Å/atom for model III. When considering the mobility of the first shell, the small displacements show that all models can stabilize these structures and provide accurate energy values.

Number of atoms per PMI	$E_{ab\ initio}$ [eV/atom]	ΔE [meV/atom] Model I	Model II	Model III
8.00	−4.753	−13	−12	−20
8.25	−4.755	−6	−7	−13
8.50	−4.756	−1	−3	−5
8.75	−4.757	+3	+2	+2
9.00	−4.755	+4	+4	+3
9.25	−4.747	+1	+1	+1
9.50	−4.741	+1	+0	+2
9.75	−4.731	−6	−5	−2
10.00	−4.731	+0	+2	+4
10.25	−4.714	−12	−12	−5
10.50	−4.704	−15	−17	−7
10.75	−4.692	−19	−21	−13
11.00	−4.683	−22	−24	−17

Table 8.6: Cohesive energies (in eV/atom) of different optimized configurations for the ξ phase. The energy differences ΔE between the *ab initio* calculations and the respective model are given in meV/atom.

From the energy differences it can be seen that the structures, containing nine or ten aluminum atoms in the first shell, are reproduced with very small errors. For the other structures the errors are considerably larger. In *ab initio* simulations, the structures with eight or eleven atoms in the first shell were mechanically unstable. The atoms drifted in- or outwards to achieve an inner shell with nine or ten atoms.

The *ab initio* formation enthalpy for these structures, shown in Fig. 8.7, also predicts the most stable structure for nine atoms, with another local minimum at ten atoms. The effective potentials show errors which are comparable to those in Tab. 8.6. For less than 8.5 and more than 10 atoms in the inner shell, the enthalpies differ more than 10 meV/atom.

To determine whether a structure is thermodynamically stable, the energy difference to the convex hull has to be calculated. If the difference is negative, the structure is considered stable, otherwise it is unstable. The energy difference to the convex hull has been calculated for all structures in Tab. 8.6. The results are shown in Fig. 8.8.

A difference between models I and II and model III can be seen. While the values

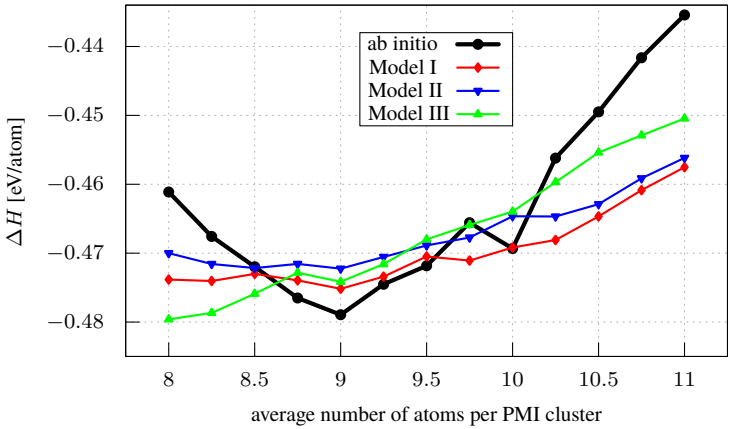

Figure 8.7: Comparison of the *ab initio* formation enthalpy ΔH with the three potential models.

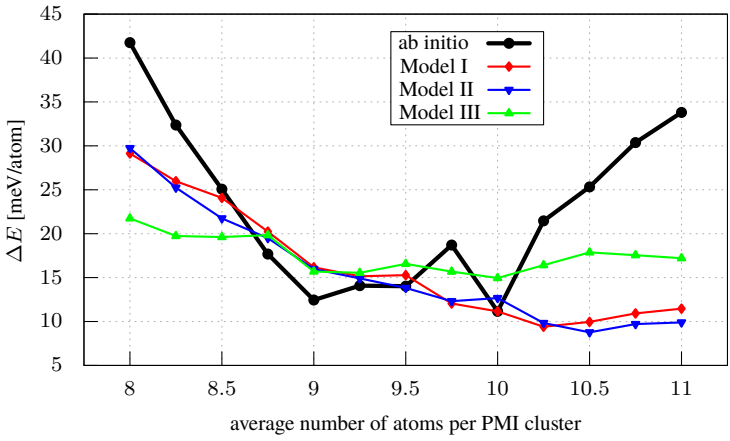

Figure 8.8: Difference of the cohesive energy to the convex hull for structures with different amount of aluminum atoms in the inner shell of the PMI cluster.

are decreasing almost monotonously for models I and II, a shallow minimum is present in the data of model III. The potential models I and II have the lowest distance to the convex hull for more than ten atoms in the first shell of the PMI cluster. As these structures are all mechanically unstable, the potential models are not suited for the structure optimization.

	$E_{ab\ initio}$	ΔE [meV/atom]		
composition	[eV/atom]	Model I	Model II	Model III
ξ–228-64-12	-4.702	-5	$+4$	0
ξ–224-68-12	-4.748	$+1$	$+7$	$+4$
ξ'–228-64-12	-4.703	-5	$+3$	$+1$
ξ'–224-68-12	-4.748	$+1$	$+5$	$+5$

Table 8.7: Energy differences of the almost stable ε phases to the *ab initio* reference values. The composition is given in numbers of aluminum, palladium and manganese atoms. All inner shells of the PMI clusters are occupied with nine atoms.

The result of the structure optimization are four structures, which are unstable by less then 1 meV/atom. In these structures not only the inner shell of the PMI clusters is changed, but also the atoms in the LBPP are rearranged. Details on the structure are given in [P2]. Two of these structures are ξ phases and two are ξ' phases. There is no special notation, the composition in numbers of aluminum, palladium and manganese atoms is used to denote the structures. The energy differences from the *ab initio* calculated reference value are given in Tab. 8.7.

All three potential models can reproduce the energies of the optimized structures with errors of few meV/atom. For effective potentials the values are very good, taking into account that none of the structures was included in the fitting process of the potentials. The formation enthalpies were also calculated (Tab. 8.8), with very similar results. The displacements after relaxation with the effective potentials are about 0.1 Å/atom for all three models.

Based on the static energy calculations all three potential models seem to be of equal quality. For further analysis of the potentials several dynamic properties were calculated.

composition	$\Delta H_{ab\ initio}$ [eV/atom]	$\Delta H_{\mathrm{EAM}} - \Delta H_{ab\ initio}$ Model I	Model II	Model III
ξ–228-64-12	-0.488	-6	$+1$	-1
ξ–224-68-12	-0.513	0	$+4$	$+3$
ξ'–228-64-12	-0.488	-6	0	0
ξ'–224-68-12	-0.514	0	$+2$	$+3$

Table 8.8: The *ab initio* formation enthalpies ΔH and the deviations of the three analytic potential models. The composition is given in numbers of aluminum, palladium and manganese atoms. All inner shells of the PMI clusters are occupied with nine atoms.

Dynamic properties of the potentials

Up to this point only energy calculations and relaxation simulations were performed. Before studying any dynamic properties of the potentials, the structural stability at finite temperatures has to be ensured. Equilibrium MD simulations were carried out at 300 K and the mean-square displacements of the atoms were calculated for all three potential models. They are defined as

$$\Delta_i^2(t) = \langle (\boldsymbol{R}_i(t) - \boldsymbol{R}_i(0))^2 \rangle, \tag{8.2}$$

where $\boldsymbol{R}_i(t)$ is the position of atom i at time t. To compare the value, the time average over the entire simulation is calculated. The results are very similar for all models, model I has a displacement of $0.13\,\text{Å}^2$, model II of $0.20\,\text{Å}^2$ and model III of $0.15\,\text{Å}^2$. These values show that the potentials can stabilize the structure at room temperature. At higher temperatures the mean-squared displacements are no longer constant, the structure shows some type of self-diffusion.

To study the diffusion, a long *ab initio* MD simulation at 1200 K of 50 ps was performed during the structure optimization. In a time-averaged picture of the density, the atoms in the first shell of the PMI cluster showed a rotational degree of freedom. The density plots are shown in Fig. 8.9.

The results for all three potential models are comparable to the *ab initio* simulation. The atoms on the innermost shell of the PMI clusters are not fixed, they can orient in different directions. The threefold axis of this inner shell always points along a fivefold axis of the outer PMI shell.

All EAM potentials can stabilize the structure even at this elevated temperature.

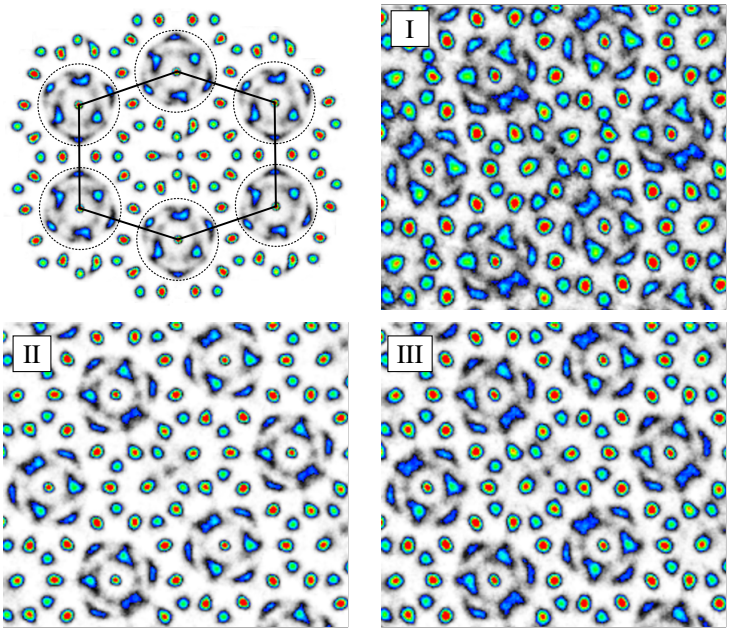

Figure 8.9: Time-averaged density plots for the ξ phase. Only the atoms in a 7 Å thick layer perpendicular to the $[0\,1\,0]$-direction are shown. Red and yellow mark a high value while blue and gray represents low values of the density. The *ab initio* simulation is shown in the top left image. The MD simulations of the three models are indicated with the corresponding number.

The density plots show the same orientational degree of freedom as the *ab initio* simulation. For model I the image looks darker, the densities are smeared out, indicating a greater thermal motion of the atoms than expected. Model II and III do not have this problem to this extent. While model II looks almost identical than the reference image, model III has some faint gray areas.

The melting point for the ξ phase has been determined for all three potential models. In a simple approach the atomic volume has been calculated while the sample was slowly heated from 950 to $1400\,\mathrm{K}$. At the melting point there is a distinct jump in the atomic volume which corresponds to the melting transition. For model I the melting was determined as $1130\,\mathrm{K}$, for model II as $1370\,\mathrm{K}$ and for model III as $1300\,\mathrm{K}$. With this method the melting point is generally overestimated, due to the high heating rates. The heating rate of the simulation of $5 \times 10^{-5}\,\mathrm{K}$ per timestep is equal to $5 \times 10^{9}\,\mathrm{K/s}$. The sample is overheated before the melting process can occur, leading to an increased melting temperature. When compared to the experimental value of $1118\,\mathrm{K}$[1], the value of potential model I is definitely too low, while the other models are in the expected temperature range.

To test a property that was not included in the reference dataset, the elastic constants for the ξ phase were calculated. The orthorhombic unit cell has nine independent elastic constants, which were determined by examining the cohesive energy during homogeneous deformations of the sample.

	ab initio	Model I	Model II	Model III
C_{11}	175.79	255.25	244.66	200.98
C_{22}	192.75	269.79	246.74	193.61
C_{33}	227.46	243.53	246.64	160.57
C_{12}	58.76	158.83	145.57	102.76
C_{13}	67.85	146.75	146.78	92.95
C_{23}	56.34	151.19	146.51	107.04
C_{44}	72.54	42.57	42.42	42.77
C_{55}	67.77	41.46	47.19	46.66
C_{66}	71.25	48.51	48.21	43.76

Table 8.9: Elastic constants of ξ-Al-Pd-Mn in GPa.

The results for all three models are shown in Tab. 8.9. The errors for all models are rather big, especially for the values of C_{12}, C_{13} and C_{23}. The elastic constants

[1] private communication with M. Feuerbacher

differ by up to a factor of three. The potentials are not able to correctly describe the shear stresses. However, the results are not surprising because of the reference data used in the fitting process. The only samples that included mechanical deformations were the high-temperature MD snapshots. They were strained along either of the Cartesian axes perpendicular to the periodic stacking axis of the approximant. The corresponding elastic constants C_{11} and C_{22} are reproduced by model III with a certain accuracy.

This shows clearly that the potentials fitted for the structure optimization are limited in their application range. For the energy and enthalpy calculations the results agree with the *ab initio* simulations up to a few meV/atom. For physical quantities that were not present in the reference database, like elastic constants, the potentials are not applicable.

When comparing the three different potential models, all of them provide reasonable results for the tests performed. While the error sums after the fitting process are very similar, the potentials show different behaviors when used in MD simulations. The trends from the RMS errors can be noticed in all tests. Models I is usually the one with the largest errors or deviations from the *ab initio* simulation. Models II and III are often very close with only slight advantages for model III.

The potential functions of model III are plotted in Fig. A.1. The individual parameters for all functions are given in Tab. A.1.

8.4 Outlook

The lowest approximants of the decagonal Al-Pd-Mn quasicrystal can be accurately described with the potential. In an ongoing work, which involves the decoration of the higher approximants as well as the core of the metadislocation, they also yield reasonable results. This is because the decoration of the new tiles does not contain new structural elements. The PMI clusters and LBPPs are present with only marginal deviations from the versions of the lower approximants.

The exact decoration of the metadislocation core, however, is still a challenge. New methods using a Monte-Carlo approach can be used to find the optimal structure. It uses randomly arranged cluster configurations to locate the lowest energy arrangement of the atoms. The effective potentials generated in the present work can be used for that purpose.

To study the movement of the metadislocation the potentials are probably not suited. It is assumed that a metadislocation core can move through the bulk when an

external stress is applied to the material. The elastic constants for all three potential models do vastly differ from the *ab initio* reference values, thus the results may be wrong.

To generate potentials for the accurate simulation of the motion of metadislocations, new potentials are required. The reference data should be revised and more stressed and strained samples should be included.

Chapter 9:

Intermetallic clathrate systems

In this chapter the physical properties of two clathrate systems are investigated. Effective potentials which include angular dependent terms have been generated for both germanium- and silicon-based structures. Clathrates are promising candidates for thermoelectric devices, in which the thermal conductivity plays a key role. Phonons are the carriers of the heat current, they have to be modeled accurately. The phononic properties of the potentials are tested in different MD simulations.

The thermal conductivity is measured with the Green-Kubo formalism for different structures of both types of systems. The influence of complexity can be measured directly by introducing vacancies in the clathrate framework. Therefore new structures, that have not yet been observed in experiment, are created.

9.1 *Ab initio* calculations

Prior to setting up the *ab initio* reference database, the pseudopotentials available in the VASP package have been tested in detail. The lattice dynamics and the phonon properties depend inherently on the lattice parameter. To ensure the simulations are in agreement with experiment, two modifications of germanium were relaxed with five different DFT schemes. The α-Ge as well as the clathrate structure Ge_{46} both have a cubic unit cell, containing 8 and 46 atoms, respectively. The results are shown in Tab. 9.1, the lattice parameter of the relaxed structure is denoted by a_0, the energy by E_0.

The different types of pseudopotential (US-PP and PAW) and the density approximation (LDA, GGA and PBE) are all explained in Sec. 4.3.2 and 4.3.3. It can be

pseudopotential and density approximation	α-Ge		Ge_{46}	
	a_0	E_0	a_0	E_0
US-PP + LDA	5.6247	−5.1997	10.4885	−5.1490
US-PP + GGA	5.7586	−4.5356	10.7340	−4.5017
PAW + LDA	5.6460	−5.1751	10.5264	−5.1252
PAW + GGA	5.7779	−4.5206	10.7685	−4.4872
PAW + PBE	5.7826	−4.4931	10.7756	−4.4615
experiment	5.658[1]	–	10.552[2]	–

[1] from [7]
[2] private communication with Y. Grin

Table 9.1: Lattice constants (in Å) and cohesive energies (in eV/atom) for two modifications of germanium. The experimental data is measured at 300 K.

seen that for both structures the LDA approach matches the experimental data better than the GGA version. The values for the ultrasoft potentials are always below the PAW values, for all available densities. The absolute energies also differ for the LDA and GGA simulations. This, however, can be neglected, because only energy differences can be deduced from DFT calculations without further considerations. For all *ab initio* calculations the LDA together with PAW potentials were used.

9.2 Reference database and fitting procedure

The potential fitting for the clathrate systems was performed as a multi-stage process. First the potentials for the framework atoms were generated and tested. In a second run the additional potentials for the binary systems were determined, while keeping the framework potential fixed. To improve the results, a third run was performed, where all potentials were optimized simultaneously. The chosen approach has the advantage, that the parameter space in the first two stages is significantly reduced when compared to a single-stage fitting process of all potentials.

Framework potentials

The reference database for both the Ge- and Si-potentials contained the equivalent structures of the respective systems. An overview is given in Tab. 9.2.

	Structure	Weight	Amount	Comment
$T = 0$	X_{46}	50	1	ground state
	X_{46}	1	8	from `phono.py`
	α-X	50	1	ground state
	X_3	100	1	artificial structure
$T > 0$	X_{46}	1	13	QMD (300 K)
	X_{46}	1	10	QMD (300 – 1800 K)
	α-X	1	39	QMD (300 K)

Table 9.2: Reference database for the clathrate framework potentials. X represents the element, either Ge or Si. The configuration weights and the number of configurations for each structure are given.

The ground states for the clathrate and the diamond structure are included with a configuration weight of 50. From the calculation of the dynamical matrix with `phono.py` there are eight configurations where single atoms are displaced. An artificial structure, containing three atoms at distinct distances is also included. It was created to close the gap in the radial distribution function at about 3 Å. The three atoms are arranged in a triangle with the edge lengths of 2.8 Å, 3.0 Å and 3.2 Å.

Most of the configurations are taken from MD runs at finite temperature. For the clathrate structure one run at a constant temperature of 300 K and one run with an increasing temperature from 300 to 1800 K was performed. Snapshots of the structure were extracted, each about 100 fs apart. The forces on the atoms were recalculated with higher accuracy. The number of snapshots from the MD run with the diamond structure is increased, to compensate for the small number of atoms in the unit cell.

The total amount of reference data for the framework potentials is 74 configurations containing 2104 atoms. Together with the energy and stress values, there are 6937 contributions to the error sum.

For the total energy and stress weight very low values of 20 and 30 were chosen, respectively. The potentials are supposed to yield accurate descriptions of the dynamics of a system, which are determined by the interatomic forces. Putting a low weight on the other quantities leads to a high accuracy for the forces.

Potential functions

In the Ge-system the necessity of angular dependent terms in the clathrate potentials was investigated. A regular EAM potential and an ADP potential were fitted. The reference data and the optimization settings were identical for both potentials. As the ADP model is an extension to the EAM model, the exact same analytic functions can be used in both potentials (cf. Tab. 9.3).

potential	EAM	ADP	reference
pair	EOP	EOP	Eq. (6.27)
transfer	CSW	CSW	Eq. (6.30)
embedding	BJS	BJS	Eq. (6.31)
dipole	–	CSW	Eq. (6.30)
quadrupole	–	CSW	Eq. (6.30)

Table 9.3: Potential functions used for the EAM and ADP clathrate potentials for the framework.

For all functions but the embedding term the smooth cutoff was enabled. Different values for the cutoff radius were tested, a value of 6 Å lead to the best results and was used for all potentials from that point on.

The ADP potential for the Si-system uses the same analytic functions as the germanium potential. An EAM potential for this system was not created.

Binary systems

For the fitting of the binary potentials the reference database was extended. It is, however, no longer equivalent for both types of host atoms. Even though both clathrates have barium as a guest atom inside the cages, the frameworks are different. In the Si-system there is no problem, the structure Ba_8Si_{46} is stable. For the larger germanium atoms a fully occupied cage structure is unstable, three of the atoms have to be replaced by vacancies to stabilize the system. The symmetry of the $Ba_8Ge_{43}\square_3$ unit cell is broken, it can be restored by using a $2\times2\times2$ supercell containing 408 atoms. The additional structures used in the fitting process of the binary potentials are given in Tab. 9.4.

The reduced symmetry of the Ge-system can also be seen in the number of configurations from the `phono.py` program. There are 26 symmetry inequivalent displacements needed, while for the Si-system only 11 are required.

Si	Structure	Weight	Amount	Comment
$T = 0$	Ba_8Si_{46}	1	1	ground state
	Ba_8Si_{46}	1	11	from `phono.py`
$T > 0$	Ba_8Si_{46}	1	9	QMD (300 K)

Ge	Structure	Weight	Amount	Comment
$T = 0$	$Ba_8Ge_{43}\square_3$	1	1	ground state
	$Ba_8Ge_{43}\square_3$	1	26	from `phono.py`
$T > 0$	$Ba_8Ge_{43}\square_3$	1	9	QMD (300 K)

Table 9.4: Additional reference data used to fit the binary structures. The upper table shows the data for the silicon system, the lower table for the germanium system.

To keep the potential model for the binary system as simple as possible, the analytic functions were adjusted to the atomic environments in the structures. The interactions of the framework were adopted from the simple systems. For the Ba-Ba and Ba-X interaction, the structure was examined in detail. The barium atoms are located at the centers of the cages with a pair separation distance of about 6.3 Å in the germanium cages and 5.7 Å in the silicon cages. For the most simple model, the Ba-Ba interaction was neglected, the potential was set to zero. Only the Ba-X interaction was accounted for with a simple pair potential and the angular-dependent terms of the ADP model.

Potentials for both systems were fitted with the simple model and tested subsequently. In static simulations the potentials performed well but they failed at temperatures above 150 K. All systems did collapse after a few thousand timesteps.

A first attempt to solve the problem was by changing the reference database of the fitting process. Several structures of the almost collapsed configuration were extracted from an MD run. The forces in these configurations were calculated with VASP and added to the reference database. Even with an increased weighting factor on these new configurations the resulting potentials were not able to stabilize the systems.

The second attempt was to introduce the Ba-Ba interactions as simple repulsive functions. The new potentials did stabilize the system without the previously described problems. In order to reduce the number of free parameters in the optimization process, the pair function of the Ba-Si interaction was changed to the

potential	Ba-Ba	Ba-Si	Si-Si
pair	SOFT	CSW	EOPP
transfer	CSW	–	CSW
embedding	BJS	–	BJS
dipole	SOFT	CSW	CSW
quadrupole	SOFT	CSW	CSW

Table 9.5: Potential functions used for the binary Ba-Si ADP potentials. The SOFT function is an analytic decay to model a repulsive potential.

CSW-type. The analytic functions used for the final potentials in the clathrate system are shown in Tab. 9.5. The SOFT potential is a "softshell" model, defined as

$$\phi(r) = \left(\frac{\alpha}{r}\right)^{\beta}. \tag{9.1}$$

The energy and stress weights are set to 50 and 30 for both systems, respectively. The increased energy weight is to account for the increased number of atoms in the structures.

All potentials fitted for the clathrate systems are given in appendix A. The parameters for all potentials are listed and the individual functions are plotted.

9.3 Potentials for Si-based clathrate systems

After the fitting process of the potentials was complete, their properties were determined in different MD simulations. Besides the structural stability and the lattice constants, the phonons play an important role for the thermal conductivity.

To simulate the simple clathrate structures, containing only one element, the potentials from the first stage of the optimization process were used. For the binary systems the final potentials were used.

The RMS errors from the final *potfit* run are given in Tab. 9.6. For a comparison with the Ge-system, two datasets were tested. In dataset a) all structures used in the fitting process are included. For dataset b), which is used for comparison, the three almost collapsed structures are removed. While the errors for both sets are very similar for the energy and stress, the total error sum and the force error differ

significantly. In the three additional structures the atomic distances are very small and the potentials have problems reproducing the resulting big forces.

Dataset	error sum	forces	energies	stresses
a)	526.93	131.35	37.31	0.11
b)	293.04	93.52	35.02	0.11

Table 9.6: Total error sum and RMS errors for the Ba-Si clathrate potential. Dataset a) includes all structures from the fitting process. In dataset b) the three almost collapsed structures are removed. The errors for the forces are given in meV/Å, for the energies in meV/atom and for the stresses in MPa.

The lattice parameters for three different clathrate structures were determined with the LAMMPS package. It allows relaxation runs which also isotropically relax the simulation box vectors. The results, together with experimental values are given in Tab. 9.7.

Structure	*ab initio*	ADP	experiment
Si_{46}	10.11	10.10	10.19[1]
Ba_8Si_{46}	10.24	10.18	10.33[2]
$Ba_8Si_{43}\square_3$	20.27	19.88	–

[1] from [69]
[2] from [110]

Table 9.7: Lattice constants for three Si-based clathrate systems in Å. The $Ba_8Si_{43}\square_3$ structure has not yet been observed in experiment.

The values of the ADP potentials agree well with the *ab initio* calculations for the experimentally observed Si_{46} and Ba_8Si_{46} structures. For $Ba_8Si_{43}\square_3$ the deviation is 2 %, which is still acceptable.

To test the structural stability, several MD simulations have been performed at different temperatures and with different structures. For 300 and 600 K all structures were stable. Higher temperatures have not been tested because there the electronic contribution to the thermal conductivity increases significantly.

9.3.1 Phonon dynamics

To determine the phononic properties of an effective potential usually the density of states and the dispersion relation are calculated. The required methods are described for *ab initio* and MD simulations in Sec. 7.1 and 7.2.

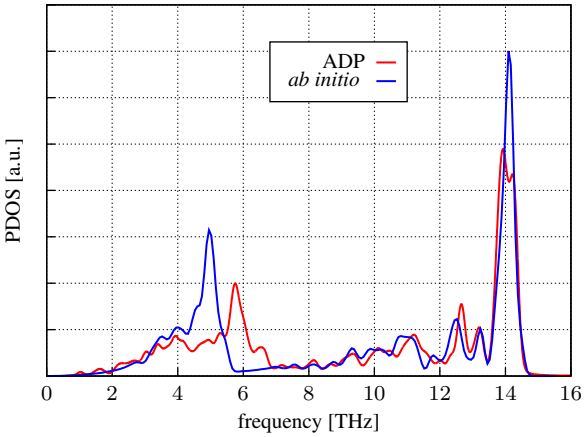

Figure 9.1: Phonon density of states for the empty clathrate structure Si_{46}. The ADP frequencies are scaled by a factor 0.98.

The density of states from *ab initio* and MD simulations for the Si_{46} structure is shown in Fig. 9.1. For an effective potential the agreement with the DFT results is very good. The peak at 14 THz as well as the minor peaks from 8 to 13 THz are well reproduced. For lower frequencies there are minor discrepancies. The single peak expected at 5 THz is shifted to 5.8 THz. Below 4 THz both calculations agree well. The oscillations of the ADP data for small frequencies might be attributed to anharmonicities in the potential, which are not present in the *ab initio* calculation.

The phonon dispersion curves for the Si_{46} system in the $(6, \xi, \xi)$-direction are shown in Fig. 9.2. Like in the density of states, the high frequency behavior is very similar, the gap from 6 to 8 THz is clearly visible. A difference is noticeable in the low-lying optical modes. In the MD calculation the frequencies are too high, as the peak in the density of states already indicated. There are also small oscillations present, which are especially prominent for the highest phonon modes. They are

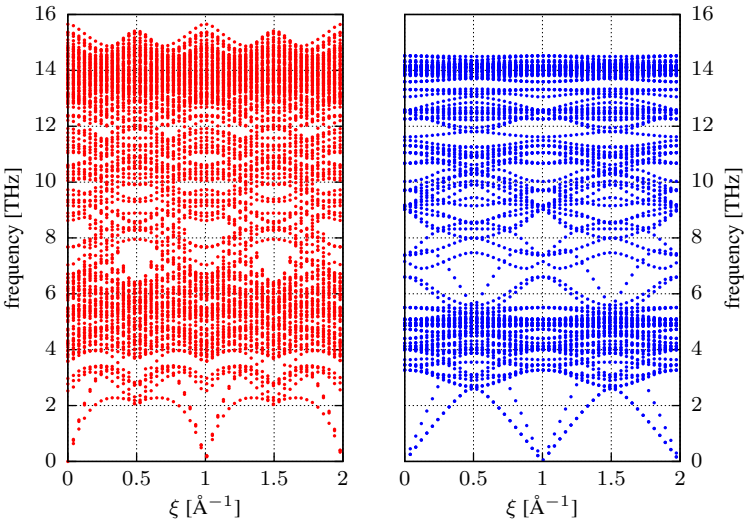

Figure 9.2: Phonon dispersion curves for Si_{46} along the $(6, \xi, \xi)$-direction. Left: MD simulation with the ADP potential. Right: DFT calculation.

most likely an artifact of the effective potentials.

For the density of states of the filled clathrate system Ba_8Si_{46}, shown in Fig. 9.3, the agreement for low frequencies is better than for high frequencies. The three peaks at 2, 4 and 5 THz agree with only small deviations. For frequencies above 6 THz the values of the ADP potential are constantly shifted about 2 THz to the right. The reason for this is unclear. High frequencies correspond to the vibrations of the framework, they are also present in the empty cage structure Si_{46}. Adding guest atoms creates phonon modes at low frequencies.

The phonon dispersion curves agree well for DFT and MD simulations. In Fig. 9.4 the $(\xi, 0, 0)$-direction is plotted. There the same issues for frequencies above 8 THz are present as in the density of states. The low frequencies do show an almost perfect agreement. However, the slope of the acoustic modes is too steep when compared to the *ab initio* data.

When compared to the dispersion curves of the empty cages, the optical modes are shifted to a lower frequency, due to the so-called rattling modes of the guest atoms. The thermal conductivity for the filled systems should be lower than for the

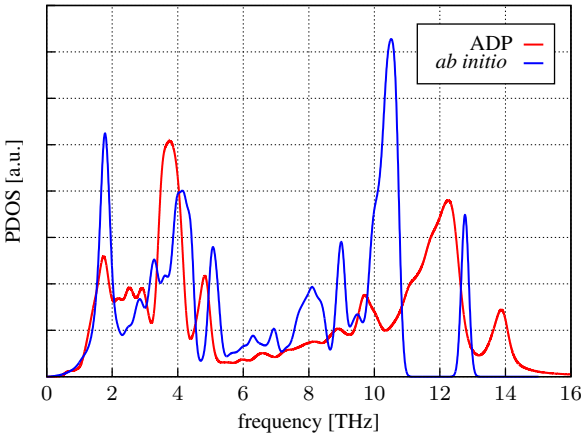

Figure 9.3: Phonon density of states for the Ba_8Si_{46} clathrate structure. The ADP frequencies are not scaled.

empty structure.

9.4 Potentials for Ge-based clathrate systems

Fitting the potentials for the Ge-based clathrate systems was done in the same way as for the Si-systems. Only the number of atoms in the reference data was increased. For the Si clathrates the stable binary structure is Ba_8Si_{46} containing 54 atoms, for Ge clathrates it is $Ba_8Ge_{43}\square_3$ with 408 atoms per unit cell. The number of datapoints in the Ge-system is almost four times larger than in the Si-system, $42\,939$ to $11\,059$. As a consequence, the total error sum after the optimization is much larger than for the Si potentials.

The RMS errors are given in Tab. 9.8. In dataset a) all structures used in the fitting process are included. For dataset b), which is used for comparison, the three almost collapsed structures are removed. When compared to the RMS errors of the Si potential, the values are very similar. The force and stress residuals are almost the same, only the energy errors are about $70\,\%$ larger.

An important difference in the fitting process can be seen in the radial distribution

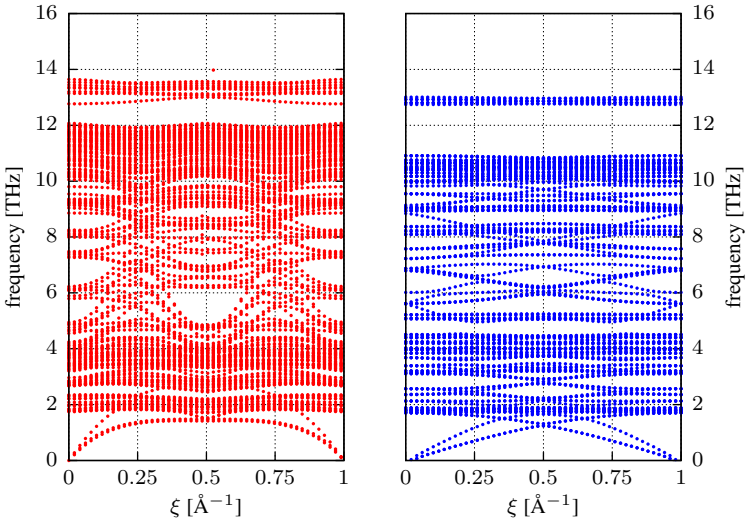

Figure 9.4: Phonon dispersion curves for Ba_8Si_{46} along the $(\xi, 0, 0)$-direction. Left: MD simulation with the ADP potential. Right: DFT results.

Dataset	error sum	forces	energies	stresses
a)	5091.90	140.10	59.96	0.14
b)	1905.71	94.90	59.27	0.13

Table 9.8: Total error sum and RMS errors for the Ba-Ge clathrate potential. Dataset a) includes all structures from the fitting process. In dataset b) the three almost collapsed structures are removed. The errors for the forces are given in meV/Å, for the energies in meV/atom and for the stresses in MPa.

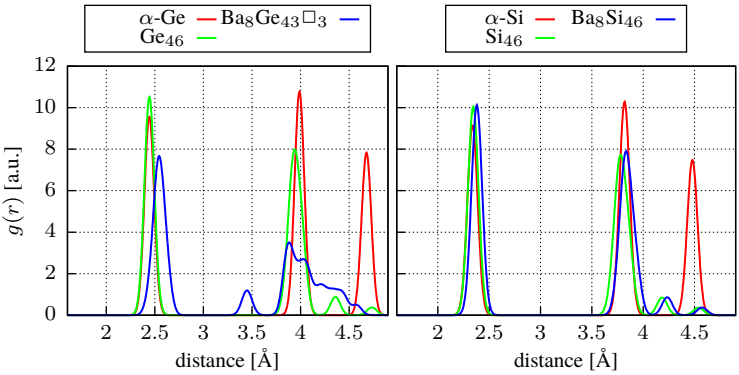

Figure 9.5: Radial distribution functions $g(r)$ for germanium and silicon clathrate systems. Only the distances of the framework atoms are taken into account.

functions in Fig. 9.5. For all silicon-based systems the first and second neighbor distances are the same in all structures used in the reference data. As a result the total error sum as well as the individual contributions are only increased slightly when changing from the Si to the Ba-Si system.

In the binary germanium system a new neighbor distance emerges, which is due to the introduction of the vacancies. A schematic drawing is shown in Fig. 9.6. All atoms close to the vacancy positions can move towards the empty space. The first neighbor distance is slightly increased and a new peak below 3.5 Å appears. The previously sharp second and third neighbor peaks are merged into a single broad peak. For the fitting process of the binary Ba-Ge system the potentials from the simple Ge system need to be adjusted to these features. The optimization was restarted several times to guarantee an optimal potential.

The lattice parameters for the different Ge-based clathrate systems are given in Tab. 9.9. For the empty cages and the filled structure the agreement is very good. The experimentally found structure, $Ba_8Ge_{43}\square_3$, which forms a $2\times2\times2$ supercell with 408 atoms, is overestimated by 4 %.

Stabilizing MD simulations in the temperature range of 150 to 600 K was not possible with all generated potentials. Only after several optimization runs with adjusted configuration weights the potentials were able to provide the required stability.

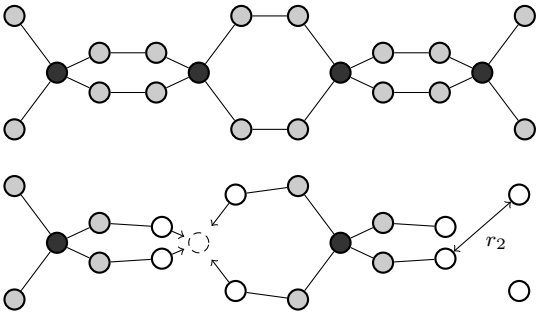

Figure 9.6: Influence of the vacancies to the structure of $Ba_8Ge_{43}\square_3$. The dark atoms are located on the $6c$ positions and can be replaced by a vacancy. Top: Ideal structure without vacancies. Bottom: Two atoms have been replaced by vacancies. As a result all white atoms are moved. The arrow in the bottom right corner indicates the new pair distance r_2.

Structure	*ab initio*	ADP	experiment
Ge_{46}	10.53	10.53	10.55[1]
Ba_8Ge_{46}	11.19	11.22	–
$Ba_8Ge_{43}\square_3$	21.08	21.93	21.31[2]

[1] private communication with Y. Grin
[2] from [6]

Table 9.9: Lattice constants for three Ge-based clathrate systems in Å. The Ba_8Ge_{46} structure has not yet been observed in experiment and is unstable in *ab initio* simulations.

9.4.1 Phonon dynamics

The phonon properties were calculated for the empty clathrate structure as well as the experimentally found binary $Ba_8Ge_{43}\square_3$ compound.

To address the question of the necessity of angular-dependent potentials, an EAM potential was fitted to the same reference data as the ADP potentials. For the Ge_{46} structure, the phonon density of states was calculated for both effective potentials as well as with DFT methods.The results for all simulations are shown in Fig. 9.7.

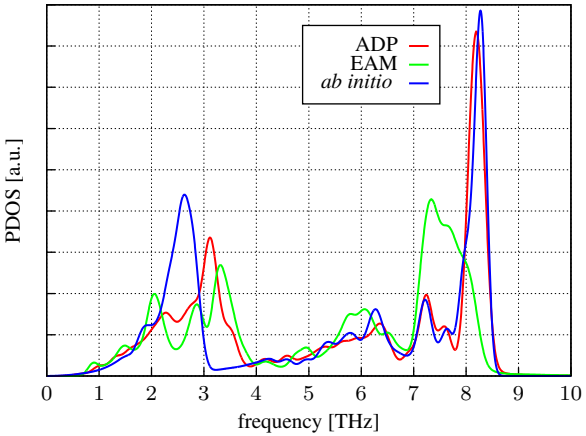

Figure 9.7: Phonon density of states for the empty clathrate structure Ge_{46}. The ADP frequencies are scale by a factor 1.02 to match the *ab initio* data. The EAM frequencies are unscaled.

While the agreement of the ADP and *ab initio* data is very good, the EAM potential is less accurate. The lower peak is split into two peaks and the upper peak is too wide and at too low frequency. For the ADP potential the only difference is the shift of the lower peak. The oscillations at very low frequencies, which are more pronounced for the EAM potential, can be caused by two different sources. One possibility are artifacts caused by the potential. The other possibility are anharmonic contributions, which are not accounted for in the *ab initio* calculation.

The additional effort required to calculate angular-dependent potentials, when compared to EAM, is justified by these results. For the Si-based clathrate system a preliminary EAM potential showed a comparable performance. Without any direc-

tional dependence in the interaction the clathrate structures cannot be described accurately enough to perform meaningful MD simulations.

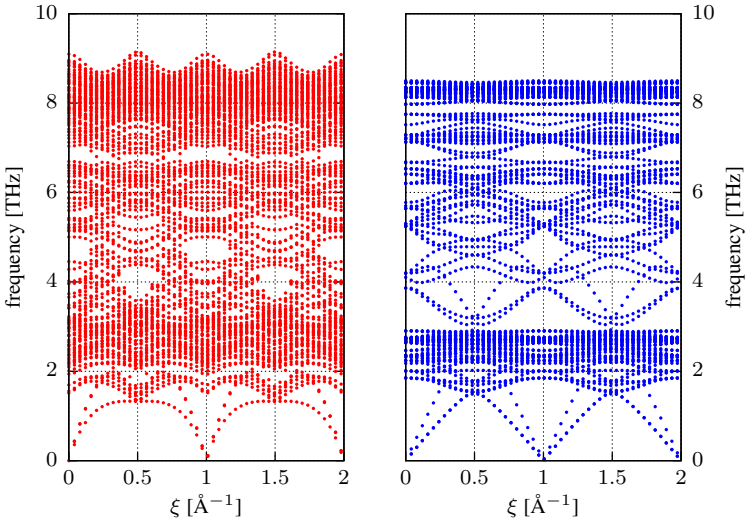

Figure 9.8: Phonon dispersion curve of Ge_{46} along $(6, \xi, \xi)$. Left: MD simulation with ADP potentials. Right: DFT calculation. The ADP frequencies are unscaled.

The results of the calculation of the phonon dispersion curves for the Ge_{46} are shown in Fig. 9.8. The overall agreement is good, only in the frequency range from 3 to 5 THz the results differ. The low-lying optical modes are reproduced well. As in Si_{46}, the slope of the acoustic branches is too steep.

For the binary Ba-Ge clathrate systems the accuracy of the effective potentials, when compared to *ab initio* calculations, is no longer as high as for the previous systems. The reason is the considerable increase in complexity of the structure. Up to this point the unit cell with an edge length of about 10 Å contained about 50 atoms. The equivalent binary Ba_8Ge_{46} structure is not stable according to *ab initio* calculations and has not been observed in experiments. By replacing three framework atoms with vacancies, the structure can be stabilized. The distribution of the three vacancies on six possible sites leads to a symmetry breaking in the single unit cell. To restore the symmetry, a $2\times2\times2$ supercell with 408 atoms is required. Even with fast DFT codes the simulation of these structures is very tedious.

The phonon density of states, calculated with the ADP potential, can only match the shape of the *ab initio* curve when the frequencies are scaled. In Fig. 9.9 the ADP frequencies are scaled by a factor of 0.9. The overall shape can be matched, only the details are missing.

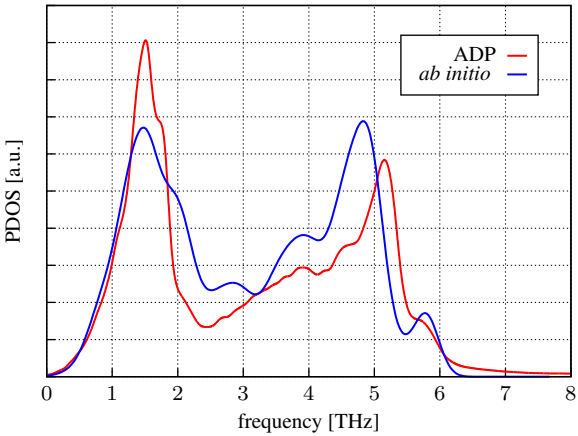

Figure 9.9: Phonon density of states for $Ba_8Ge_{43}\square_3$. The ADP frequencies are scaled by a factor 0.9.

A calculation of the phonon dispersion curves for the $Ba_8Ge_{43}\square_3$ structure was very difficult, both with *ab initio* methods and with MD simulations. For the *ab initio* simulation the required 26 displacements can be calculated with medium precision, setting up the dynamical matrix and calculating the eigenvalues is a tedious problem. The 408 atoms in the unit cell yield 1224 phonon branches, which take several hours to calculate. For the visualization only every 10th branch is shown. The MD simulations of $Ba_8Ge_{43}\square_3$ did not show any peculiarities, the calculation of the dispersion curves from the atomic displacements, however, did not work well. One reason might be the method itself, which was designed for small unit cells. The large number of atoms might require a different approach, like the velocity autocorrelation method mentioned in Sec. 7.2. Another possible reason for the problems are the algorithms used in the post-processing tool, which seem to have conversion problems for such large datasets.

Both dispersion curves are shown in Fig. 9.10. The *ab initio* calculation shows phonons at very low negative frequencies, which can be neglected for such a large

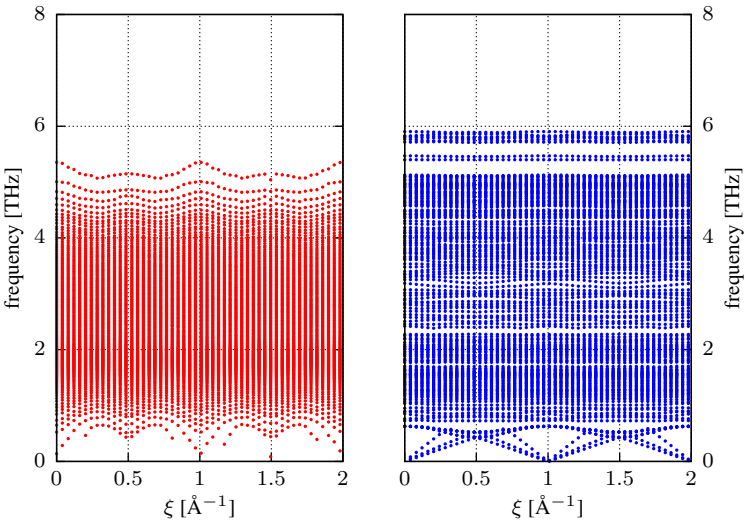

Figure 9.10: Phonon dispersion relations for the $Ba_8Ge_{43}\square_3$ system along the $(6, \xi, \xi)$-direction. Left: MD simulation of with ADP potentials. Right: *ab initio* calculation.

system. For the MD result the negative frequencies make up a large fraction of the spectrum, in the plot they are removed. Usually meta- or unstable structures exhibit negative frequencies, both in the density of states and phonon dispersion relation. As this is not the case, the negative frequencies might be related to the calculation method.

The MD simulation, shown on the left, yields frequencies only up to 5 THz and optical modes at 1 THz. For the frequencies in between, the data is too dense to distinguish any phonon modes. When compared to the density of states, the higher frequencies are missing, which might be related to the large negative phonon modes.

In the *ab initio* calculations, shown on the right hand side of Fig. 9.10, the optical modes also start at the very low frequency of 1 THz. The individual modes at higher frequencies are no longer distinguishable due to the number of atoms in the unit cell. The thermal conductivity of this structure should be lower than for all previously examined structures.

9.5 Thermal conductivity

The effective potentials generated for the intermetallic clathrate systems were used to study the thermal conductivity of different structures. First several tests were performed to establish a common calculation method and to investigate the influence of the system size. The thermal conductivity of clathrate structures with increasing complexity was measured at room temperature. For the most complex structure the results were not conclusive, another calculation method was used as comparison. Finally the influence of vacancy ordering on the thermal conductivity was investigated.

9.5.1 Diamond structure

The first test of the Green-Kubo method was performed for germanium in the diamond structure. Results of different methods with various potentials are available in the literature and can be used for comparison.

All simulations for the diamond structure were performed using the LAMMPS code. The output was written in an IMD compliant format, so the already existing postprocessing tools could be used. A Stillinger-Weber type potential from Ding and Andersen [31] and a Tersoff potential [114] were used as comparison. All results are averaged over 20 MD runs with 1.5 million timesteps at 300 K. The experimental value for the thermal conductivity of germanium at 300 K is about 60 W/mK [43]. In Fig. 9.11 the normalized HCACF is shown in the top row for all three potentials. The corresponding integrals with error bars are shown directly below.

The simulations with the three different potentials yield very different results. For the ADP potentials the HCACF decays very quickly, the integral yields a value of about 20. The Stillinger-Weber potential produces an autocorrelation function, which does decay very slowly. Its integral also converges slowly, requiring long simulation times. The numerical value for the thermal conductivity is 165. With the Tersoff potential an intermediate result is obtained. The integrated autocorrelation function converges after about 150 ps with a value of 87.

The large discrepancies between the individual potentials show that the Green-Kubo method is very sensitive concerning the employed interactions. While all models can stabilize the crystal structure at the correct lattice constant, the results differ by almost one order of magnitude. An explanation for the low value of the ADP potentials is the lack of transferability in the potential. Although it was fitted

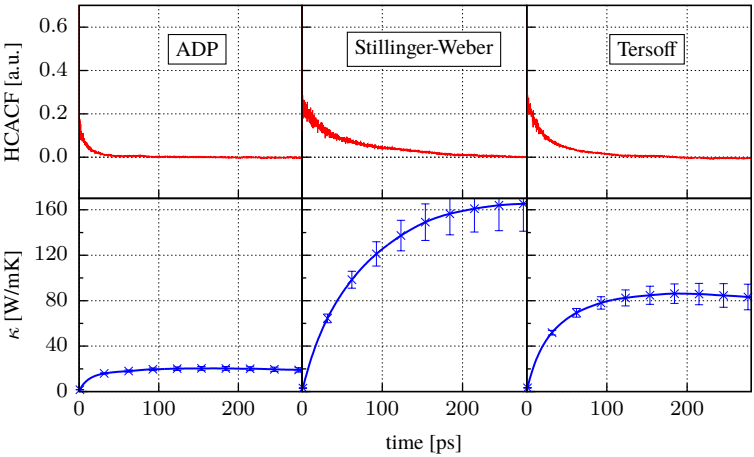

Figure 9.11: Thermal conductivity of α-Ge calculated with an ADP, Stillinger-Weber and Tersoff potential. The autocorrelation functions are shown in the upper row, the corresponding integrals below. All simulations were performed at 300 K with a $6\times6\times6$ supercell containing 1728 atoms.

with α-Ge reference data, the phonon properties are not reproduced correctly. The value for the Tersoff potential is comparable to a previous calculation of Dong *et al.* [32]. They reported a thermal conductivity of 114 W/mK using the Tersoff potential and the Green-Kubo method with a slightly different integration technique. The reason why the Stillinger-Weber potential yields such a high value is not clear.

9.5.2 Empty clathrate structures

Before calculating the thermal conductivity of the clathrate systems, the required system size was determined. In computer simulations of solids there is the possibility of finite-size effects. Particularly periodic boundary conditions, which are used for all simulations in the present work, can change the outcome of simulations dramatically. To exclude any finite-size effects in the thermal conductivity calculations, the system size was increased until a steady value was achieved.

The simulations were performed with the IMD code and 1.8 million timesteps at the respective temperature. The first 300 000 steps are used to equilibrate the

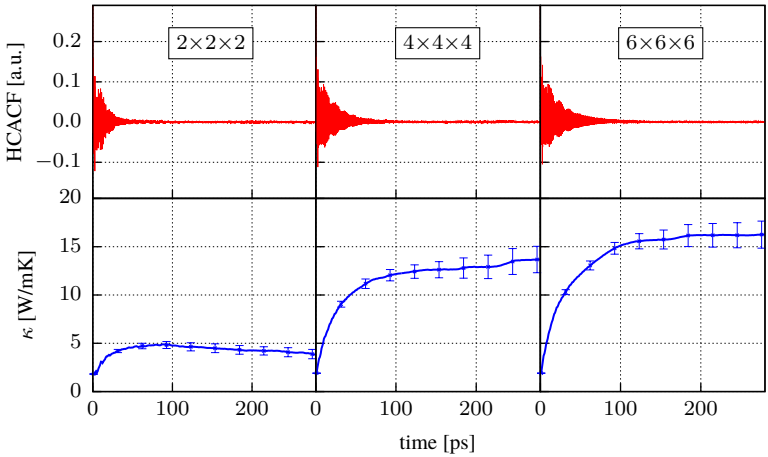

Figure 9.12: Comparison of the HCACF and the corresponding integrals for different supercells. The simulations are performed with the Ge_{46} structure at 300 K.

sample and measure the reference energy of the single atoms. The heat current $\boldsymbol{J}$ is subsequently measured for 1.5 million steps. In Fig. 9.12 the result of 20 averaged simulations are shown for cubic systems with an edge length of 2, 4 and 6 unit cells. The number of atoms in the simulations was 368, 2944 and 9936, respectively.

The influence of the finite-size effects can be seen clearly in the HCACF and the integrated thermal conductivity. For the $2\times2\times2$ supercell the autocorrelation function decays the fastest, the integral converges at a very low value. When the system size is increased, the autocorrelation decays slower, which yields a higher thermal conductivity.

The measurements were done for all system sizes up to a $7\times7\times7$ supercell at two different temperatures to determine the minimum system size for meaningful simulations. For the Ge_{46} structure the results are shown in Fig. 9.13, for Si_{46} in Fig. 9.14.

Apart from the absolute values, both figures look very similar. The $2\times2\times2$ supercells are not able to provide reasonable results. The number of atoms is too small to provide meaningful statistical averages. All other structures with larger simulation boxes can provide the necessary amount of data for statistical analysis.

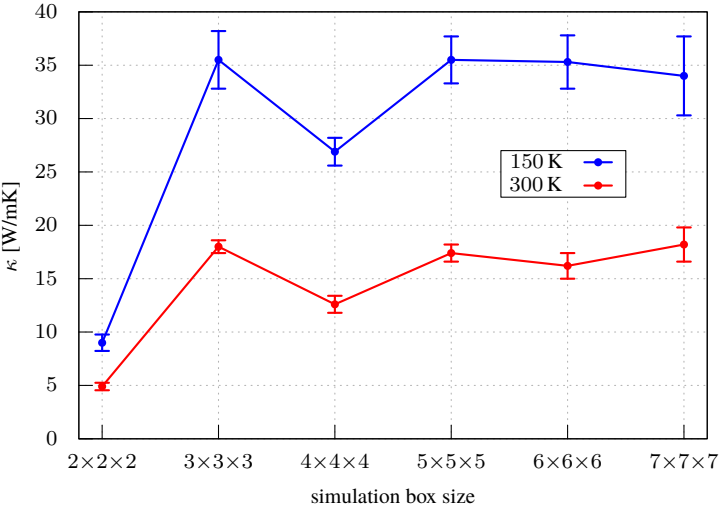

Figure 9.13: Dependence of the thermal conductivity of Ge_{46} on the simulation box size for two different temperatures.

Apart from the dip for all $4\times4\times4$ supercells, the simulations converge already for the $3\times3\times3$ supercell, within an error limit. The dip is present in all four test series, it is more pronounced for lower temperatures and almost not visible for the Si_{46} structure at 300 K. The reason is not completely clear. A possible explanation can be found looking at the density of states for the different box sizes. In the $4\times4\times4$ results there is a small extra peak visible at about 1 THz, which is missing for all other sizes. To calculate the wavelength of these phonons, the velocity of sound is required. For α-Ge the value is about 5000 m/s, for the clathrate structure it should be a little bit lower. Assuming a velocity of sound of 4000 m/s, the wavelength would be 40 Å, almost exactly the size of the simulation box of the $4\times4\times4$ supercell. The phonon mode is a shortcoming of the ADP potential, which can be circumvented by using a bigger or smaller simulation box.

For the present work, all values for the thermal conductivities were extracted from the simulations of a $6\times6\times6$ supercell. To get reliable and comparable data, all calculations should be performed under similar conditions.

In the literature there is another theoretical study of the thermal conductivity of the

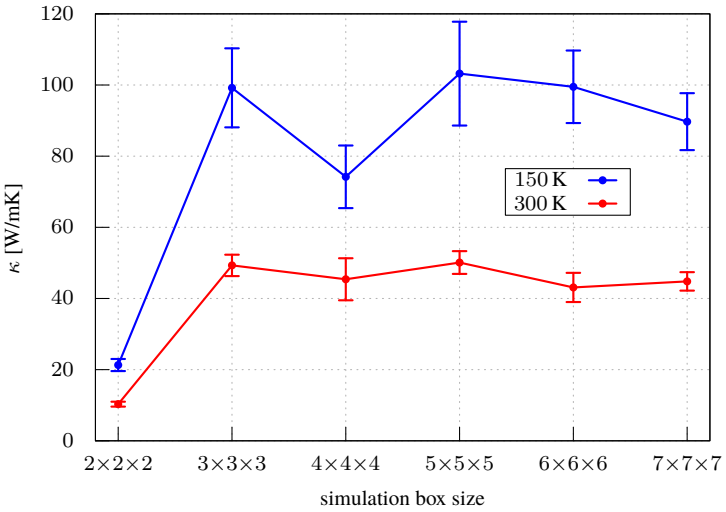

Figure 9.14: Thermal conductivity of Si_{46} at 150 and 300 K for different simulation box sizes.

Ge_{46} clathrate system. Dong *et al.* [32] used a Tersoff potential and reported a κ of 12.2 W/mK, which is comparable to the value of the ADP potentials, 16.2 W/mK.

9.5.3 Filled clathrates

The complexity of the clathrate systems can be increased by introducing guest atoms in the host framework. For type I structures there are eight cages, which can host such atoms. A common element used is barium, a heavy alkaline-earth metal. It can be placed into the silicon cages, forming the Ba_8Si_{46} structure. When placed into the germanium cages, the structure becomes unstable, until some of the framework atoms are removed. To restore the symmetry broken by the introduction of vacancies, a $2\times2\times2$ supercell of $Ba_8Ge_{43}\square_3$ can be used in computer simulations. The experimentally observed superstructure has either a partially- or fully-ordered distribution of the vacancies, depending on the preparation method of the crystal [6].

The HCACF and the integrated thermal conductivity for the Ba_8Si_{46} structure are shown in detail in Fig. 9.15. With the addition of the barium guest atoms, the

thermal conductivity is reduced, as predicted from the phonon dispersion curves. The autocorrelation function decays much quicker than for the empty clathrate, which leads to a lower value of the integral.

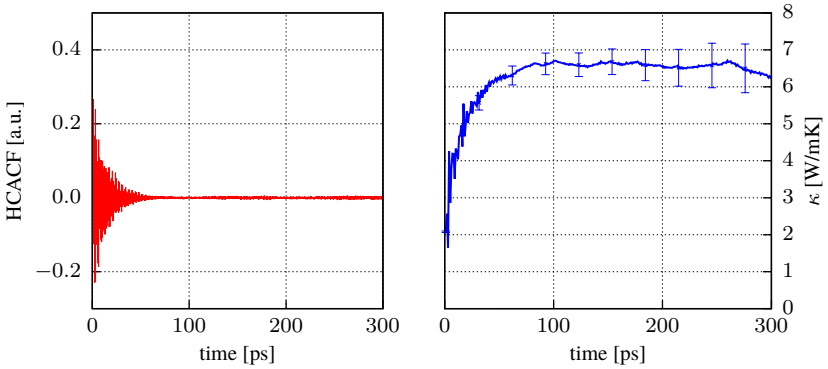

Figure 9.15: Left: Normalized HCACF for the Ba_8Si_{46} structure. Right: Integrated thermal conductivity at $T = 300\,\mathrm{K}$.

As for the empty structures, the thermal conductivity has also been calculated for different box sizes. The result is shown in Fig. 9.16. The $2\times2\times2$ simulation box is too small to provide reasonable statistics and the dip at $4\times4\times4$ is also visible. When compared to the empty structure, the thermal conductivity is reduced to one third.

The filled clathrate structure for the Ge-system is $Ba_8Ge_{43}\square_3$, which introduces guest atoms as well as vacancies. The detailed results from the Green-Kubo method are shown in Fig. 9.17. It is particularly noticeable that the correlations of the heat current decay almost instantly. For times larger than $10\,\mathrm{ps}$ only noise is left. Despite the short correlations, the Green-Kubo method provides reasonable results .

The thermal conductivity of $Ba_8Ge_{43}\square_3$ has been determined for three different box sizes. The results, shown in Fig. 9.18, predict a very low conductivity of about $0.95\,\mathrm{W/mK}$. As the supercells with 3 and 5 unit cells per edge are not available, the conversion of the value cannot be checked. Regarding the small absolute differences of the thermal conductivity for this system, a value in the range between 0.8 to $1\,\mathrm{W/mK}$ can safely be assumed.

An experimental value for the thermal conductivity of $Ba_8Ge_{43}\square_3$ was measured by Aydemir *et al.* [6]. The Wiedemann-Franz law was used to extract the lattice

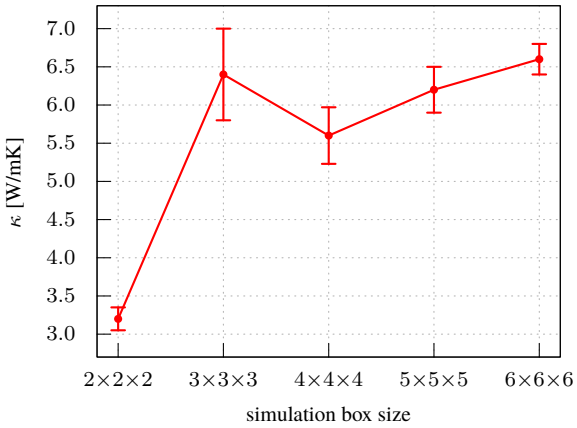

Figure 9.16: Thermal conductivity of the Ba_8Si_{46} system for different box sizes at 300 K.

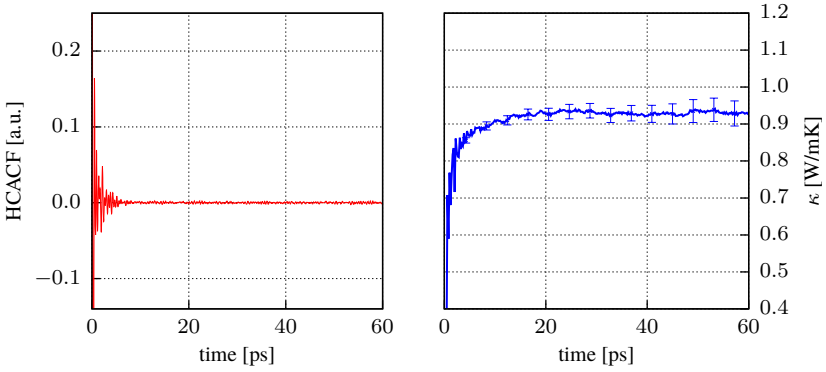

Figure 9.17: Left: Normalized HCACF for the $Ba_8Ge_{43}\square_3$ structure. Right: Thermal conductivity at 300 K.

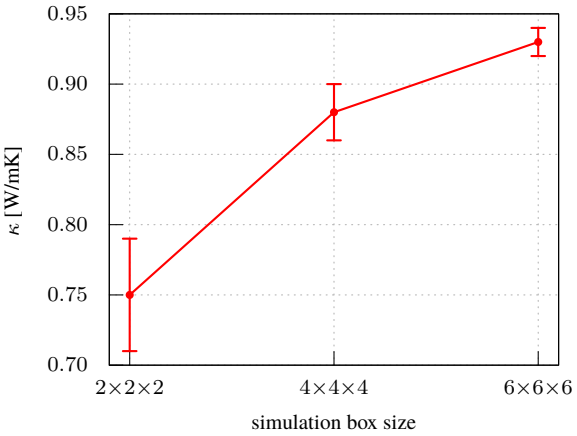

Figure 9.18: Thermal conductivity for the $Ba_8Ge_{43}\square_3$ structure at 300 K.

contributions of the thermal conductivity. For a temperature of 300 K the total value is 3.2 W/mK, the lattice part 2.7 W/mK and the electronic part 0.5 W/mK. The result from the MD calculation is too small by a factor of 3.

Unfortunately there are no measurements available for the other Ge-based clathrate systems. The empty cage structure has been synthesized, the crystal size, however, was too small to perform any macroscopic measurements.

9.5.4 Artificial structures

To further investigate the influence of the structural complexity on the thermal conductivity, additional structures were created. The frameworks of both stable binary systems were exchanged, yielding two new structures, Ba_8Ge_{46} and $Ba_8Si_{43}\square_3$. Both have not been observed in experiment – DFT calculations predict them as unstable. With the effective potentials it is possible to stabilize these systems by adjusting the lattice parameter. Doing so, both structures can be used in MD simulations to calculate the thermal conductivity. The results then allow for a comparison between three degrees of complexity of the same system.

The values obtained for the $Ba_8Si_{43}\square_3$ system are in the expected range. They are lower than for the Ba_8Si_{46} structure, yet higher than for the germanium counterpart. Details for the HCACF are given in Fig. 9.19. The decay is short, the corresponding

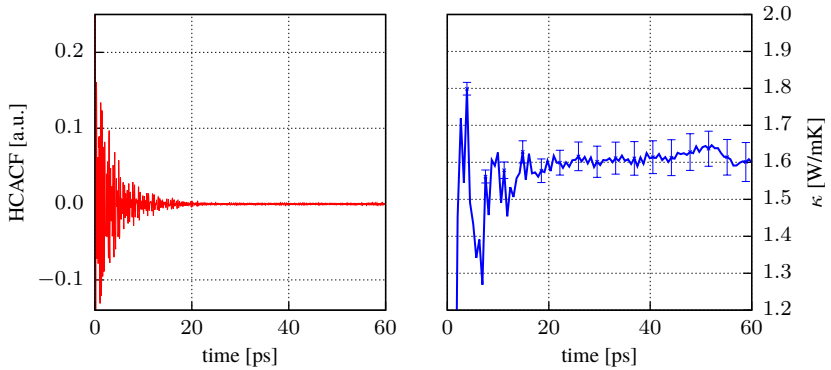

Figure 9.19: Left: Normalized HCACF for the artificial $Ba_8Si_{43}\square_3$ system. Right: Thermal conductivity calculated at 300 K.

integral, however, converges quickly to a value of 1.61 W/mK. The dependence on the box size is shown in Fig. 9.20. The $2\times2\times2$ supercell is again too small, the values for both larger boxes are almost identical.

For the filled germanium clathrate without vacancies the HCACF and the thermal conductivity are given in Fig. 9.21. The results are comparable to Ba_8Si_{46}, the absolute values are lower.

The dependence of the thermal conductivity on the simulation box is shown in Fig. 9.22. For the $4\times4\times4$ supercell a dip is visible as for the empty clathrate structure. In the phonon density of states there are some very low contributions at 1 THz, whose wavelength is about the same as the box length. The $6\times6\times6$ supercell yields a lower value than the boxes with 3 and 5 unit cells per edge. The reason for this are probably low frequency phonons, which occur as artifacts of the potentials.

The artificial structures have provided valuable data. From the empty structure and one filled clathrate for each element, the question of the low thermal conductivity cannot be solved completely. With the artificial structures both systems can be compared for all degrees of complexity. For an increasing complexity both systems show the same behavior. The low thermal conductivity of the clathrate systems is thus a combination of the rattling modes of the guest atoms and the low phonon modes, created by the vacancies.

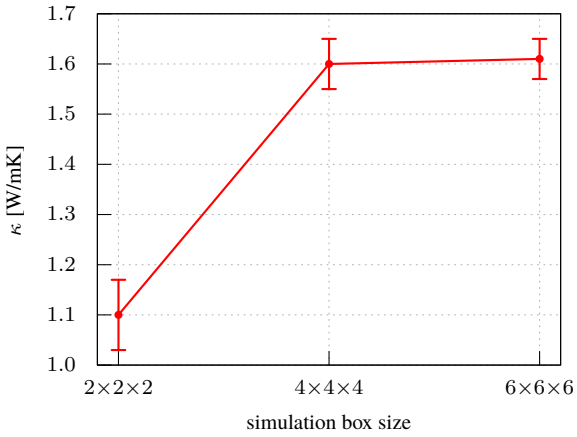

Figure 9.20: Thermal conductivity of the artificial $Ba_8Si_{43}\square_3$ structure for three different box sizes. The simulations are performed at a temperature of 300 K.

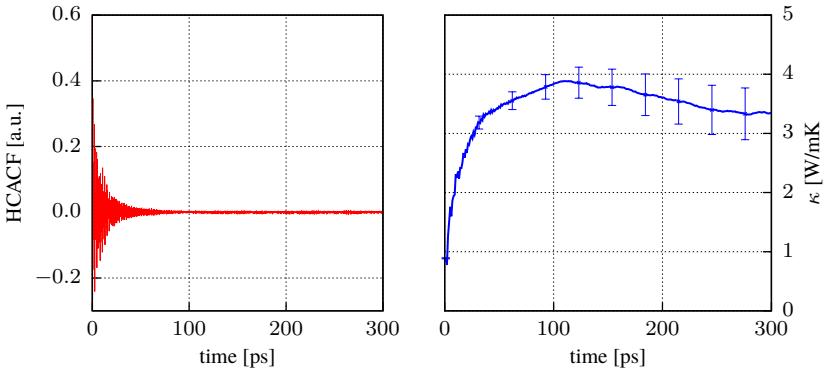

Figure 9.21: Left: Normalized HCACF for the artificial Ba_8Ge_{46} system. Right: Thermal conductivity calculated at 300 K.

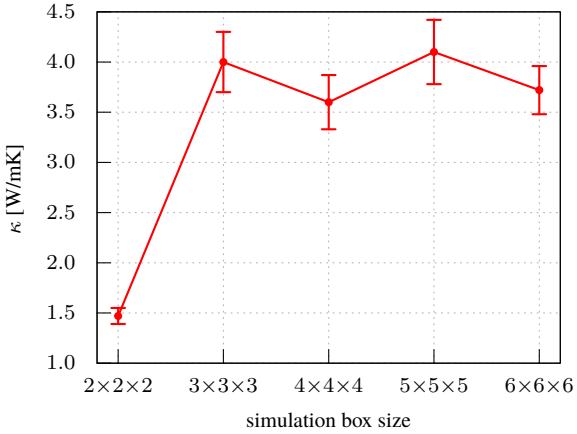

Figure 9.22: Thermal conductivity of the artificial Ba_8Ge_{46} structure for three different box sizes. The simulations are performed at a temperature of 300 K.

9.5.5 Comparison with the direct method

A verification of the calculated thermal conductivities is difficult. The experimental values cannot be used as reference values, they often include electronic contributions and are measured on real crystals, containing defects and impurities. The values obtained from MD simulations inherently depend on the employed potentials. To verifying the results, the same potential can be used with a different calculation method. Apart from the influence of the method itself, for a reliable potential the results should not differ significantly.

For the calculation of the thermal conductivity from MD simulations, the Green-Kubo method and the direct method are available. Two Müller-Plathe runs with different system sizes were performed for the $Ba_8Ge_{43}\square_3$ system. Both simulations used 4 unit cells per edge in the directions perpendicular to the heat current. The number of unit cells in the direction of the heat current was chosen as 20 and 40.

The temperature distribution after 100 ps is shown in Fig. 9.23. The number of layers was kept fixed at 40. Thus the number of atoms per layer is increased for the larger box, which provides a better statistical average for the individual layers.

With the heat current imposed on the sample, the thermal conductivity can be

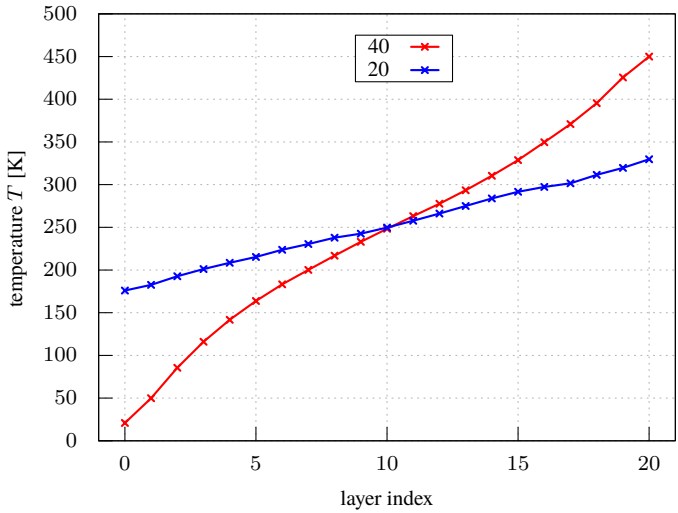

Figure 9.23: Temperature distribution at the end of two Müller-Plathe simulations for the thermal conductivity of $Ba_8Ge_{43}\square_3$. The numbers 20 and 40 indicate the size of the box in the direction of the heat current, in multiples of the unit cell.

calculated. The large system used a heat current of $0.000\,005$ in IMD units, which is about 3.2×10^9 W/m^2 in SI units. For the small sample half the heat current was applied. The calculated thermal conductivities are 0.59 W/mK for the short sample and 1.04 W/mK for the long sample.

When compared to the value obtained with the Green-Kubo method, 0.93 W/mK, the long sample yields a similar value. The value of the short sample is too small. With only 20 unit cells in the direction of the heat current, the heat flux is restricted by finite size effects. For the same sample and twice the heat current, the value for the thermal conductivity did not change.

The quality of the potentials is sufficient to achieve an agreement for two different methods, which use equilibrium and non-equilibrium MD simulations. A qualitative comparison between the two methods for the different clathrate structures was not attempted.

9.5.6 Ordered vacancies

An open question for the $Ba_8Ge_{43}\square_3$ structure is the influence of the vacancy arrangement on the thermal conductivity. In the experimentally refined structure model the vacancies are almost fully ordered. The possible positions for the replacement of a framework atom with a vacancy are the $6c$ positions. They are shown in detail in Fig. 9.24.

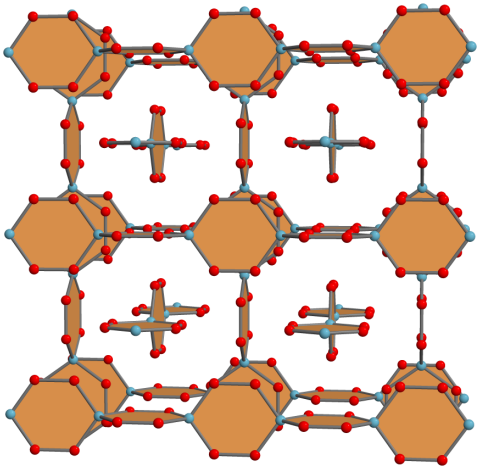

Figure 9.24: Arrangement of the spiro-hexagon chains in the $Ba_8Ge_{43}\square_3$ structure. The atoms sitting on the $6c$ position, connecting the hexagon faces of the clusters, are drawn as teal spheres. Adapted from [6].

The structure determination showed, that out of the two positions belonging to one hexagon, the occupation factor of one site is 91 %, for the other it is only 9 %. The perfectly ordered structure would have all atoms sitting on one site. A schematic drawing is shown in the left hand side of Fig. 9.25.

By shifting one chain to either side, the order can be broken, resulting in an alignment of the vacancies along one direction. Doing so creates layers with alternating high and low concentrations of framework atoms along that direction. On the right hand side of Fig. 9.25 the shifted chains are highlighted in red. The layers are perpendicular to the red lines. Experimentally it is extremely difficult to produce these structures and measure their thermal conductivity. In computer simulations the vacancies can be ordered easily.

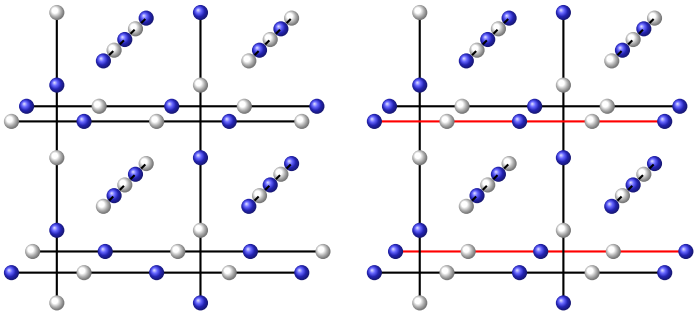

Figure 9.25: Distribution of atoms and vacancies on the $6c$ position in the $Ba_8Ge_{43}\square_3$ structure. Vacancies are draw as white spheres, germanium atoms as blue spheres. The unit cell is only shown partially. Left: Complete ordering. Right: Partial ordering. Adapted from [6].

A $Ba_8Ge_{43}\square_3$ structure was created, where the vacancies in the x-direction are arranged as shown in the right hand side of Fig. 9.25. The ordering along the other two directions was not altered.

The results with the Green-Kubo method are shown in Fig. 9.26. In the averaged integral of the HCACF as well as the individual components for all Cartesian directions there is no significant effect visible. The decay in the autocorrelation function does not change, compared to the fully-ordered $Ba_8Ge_{43}\square_3$s structure. For an in depth analysis the individual components of the heat current $\boldsymbol{J}$ were examined. The thermal conductivity has been calculated for all three directions, the results are shown on the right hand side of Fig. 9.26. While there is a slightly smaller value for the x-direction until 100 ps, the fluctuations are too large to quantify the effect. Taking the error bars into account, a prediction of the effect is not possible. The overall very low thermal conductivity as well as the expected small changes may be below the precision the Green-Kubo method and the effective potentials can provide.

9.6 Conclusion

With the *potfit* program and *ab initio* calculated reference data, effective potentials for intermetallic clathrate systems were generated. Their phononic properties were tested and compared to DFT reference data. The angular-dependent potentials show

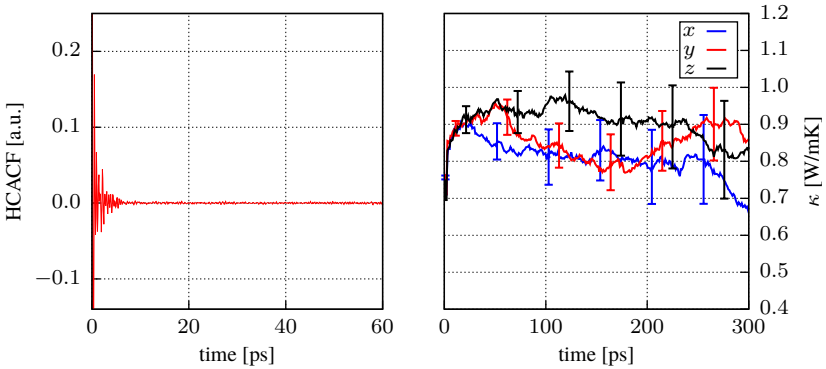

Figure 9.26: Thermal conductivity for the vacancy-ordered $Ba_8Ge_{43}\square_3$ structure at 300 K. Left: Normalized HCACF. Right: Individual components of the integrated HCACF for the three Cartesian directions.

good agreement for the phonon density of states as well as the phonon dispersion curves of simple and more complex structures.

Using the Green-Kubo method, the thermal conductivity of six clathrate structures was determined. An overview of the results is given in Tab. 9.10. The general trends are the same for both types of systems. For the empty cages, the X_{46} structure, the largest values for the thermal conductivity were found. When guest atoms are placed inside the cages of the framework, the thermal conductivity is reduced. The rattling modes of the guest atoms act as scattering centers for the heat carrying phonons. The lowest value for the thermal conductivity was found in the most complex systems, the $Ba_8X_{43}\square_3$ clathrates. The vacancies, which replace several framework atoms, reduce the lattice thermal conductivity even further.

System	X_{46}	Ba_8X_{46}	$Ba_8X_{43}\square_3$
Ge	16.2 ± 1.2	3.7 ± 0.2	0.93 ± 0.01
Si	43.1 ± 4.1	6.6 ± 0.2	1.61 ± 0.04

Table 9.10: Thermal conductivity for different clathrate systems at 300 K in units of W/mK.

To test the reliability of the potentials and the Green-Kubo method, the thermal conductivity has also been calculated with the direct method. The results for both

methods are very similar. Regarding the different approaches and the small effects measured, the potentials can be considered well suited for these simulations.

The question of the influence of vacancy ordering could not be resolved clearly. For the ordered structure the values were almost identical to the regular structure of $Ba_8Ge_{43}\square_3$. Either the thermal conductivity does not change, the effect is very small or it cannot be captured with the effective potentials.

Chapter 10:

Summary and Outlook

In the present work different complex metallic alloys have been studied with molecular dynamics simulations. The required interatomic potentials were generated using the force-matching method, implemented in the *potfit* code. A large database of *ab initio* calculated quantities, like forces and energies, was used to fit an effective potential. To verify the physical relevance of the potentials, different tests were performed to determine their static and dynamic properties. Besides lattice constants, the melting temperature or the phonon dispersion curves were calculated and compared to *ab initio* results. With the force-matching method it was possible to generate accurate potentials for complex metallic alloys, which were previously inaccesible in MD simulations.

A major part of the thesis concerns the improvement of the already existing force-matching code *potfit*. An new optimization algorithm, differential evolution, was implemented. It uses a self-adapting scheme for the control parameters and is well suited for analytic potentials. New features like global parameters, the smooth cutoff function and configuration weights were introduced to facilitate the fitting of analytic potentials for complex metallic alloys. Angular-dependent potentials were ported from the IMD code to *potfit*, allowing the generation of directionally dependent interactions. The sucess of this work can be seen in the ever increasing number of *potfit* downloads from the homepage as well as the feedback from its users.

The ternary Al-Pd-Mn system was used to determine the suitability of different analytic potential functions for CMAs. Three models, which allowed for oscillations in different parts of the EAM formalism, were created. The reference data was taken from the simulaneously performed structure optimization of the ε phases. While all

models showed similar results for basic tests, the advanced properties could only be reproduced by two of the three models. Especially the formation enthalpy and the distance to the convex hull was difficult to reproduce for all models. Additional tests like the calculation of the melting point, elastic constants and cluster dynamics showed, that the potential model with oscillations in the pair and transfer functions can most accurately describe the ε phases.

The second class of systems investigated are intermetallic clathrates. They are promising candidates for thermoelectric applications. To model the strongly directional dependent interactions in their framework, ADP potentials were fitted. Usually the host atoms of clathrate structures are germanium or silicon, containing heavy guest atoms like barium. The potentials for Ge- and Si-based clathrates were generated in a multi-stage fitting process. First the interaction of the framework was optimized. In the second step the framework potential was kept fixed while the interactions required for the barium guests were fitted. The resulting potentials can accurately reproduce the *ab initio* calculations of the phononic properties, which are important for realistic thermal transport simulations.

The thermal conductivity has been determined for different clathrate systems, using the Green-Kubo formalism. For germanium- and silicon-based frameworks, three structures with increasing complexity were investigated in detail. The results were very similar for both elements. The value for the thermal conductivity was largest for the empty clathrate. When guest atoms are placed inside the cages, the thermal conductivity is reduced significantly. The lowest values for the thermal conductivity were found for the most complex structures. By replacing some of the framework atoms with vacancies, the disorder in the system can be increased. The thermal conductivity decreases when going from the simple structures to the complex ones. However, not only the rattling modes of the guest atoms are responsible, the vacancies also contribute to the reduction of the thermal conductivity.

Measuring the influence of vacancy-ordering in the most complex structure was not possible with the Green-Kubo method and the effective potentials. The effect on the already low value of the thermal conductivity of $Ba_8Ge_{43}\square_3$ is either below the error margin or cannot be reproduced by the potentials. A possible scenario where the effect should be more pronounced is the $Ge_{43}\square_3$ system. Without the guest atoms, the overall value for the thermal conductivity is higher. Small changes can thus be detected more easily.

Another interesting application of the clathrate potentials are the ternary systems. There are many structures, where some of the framework atoms are replace by a third element, e.g. gold or nickel. The mechanisms responsible for the reduction of

the thermal conductivity in these systems are the topic of current research projects. Using the already established potentials as a starting point, the interactions for ternary systems can be generated very efficiently.

In the present work it could be shown that analytic potentials generated with the force-matching method can be used to study complex metallic alloys with molecular dynamics simulations. With the appropriate reference data even intricate properties like formation enthalpies or the thermal conductivity can be accurately described by the potentials.

Appendix A:

Analytic parameters for the potentials

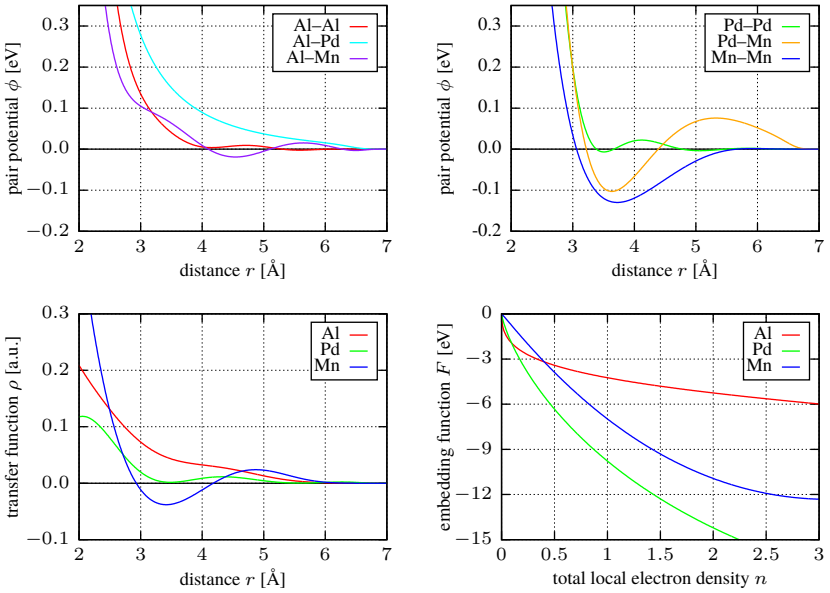

Figure A.1: Plots of the individual functions for the model III Al-Pd-Mn potential. The pair potentials are shown in the top row, transfer and embedding function in the bottom row.

EOP pair function							
pair	C_1	η_1	C_2	η_2	k	φ	h
Al-Al	586.4805	7.6769	−0.0333	1.0012	3.7658	3.8484	1.3897
Al-Mn	338.7250	7.5484	−0.4212	1.9271	2.7530	0.0033	0.5000
Al-Pd	981.8107	9.1908	−89.9193	4.7322	0.2491	1.3235	0.6211
Mn-Mn	3.8460	19.9995	−44.5953	4.1469	1.2084	1.0115	1.5938
Mn-Pd	12.8931	3.4348	−90.3824	4.4851	1.6212	0.0005	0.5007
Pd-Pd	6625.3081	9.5962	99.8792	6.1164	3.8088	2.5086	0.5235
transfer function							
element	a_1	a_2	α	β	h		
Al	0.1317	0.0399	2.7507	2.3142	1.9995		
Mn	−1.5432	1.0321	1.6018	2.4154	1.9996		
Pd	0.4962	0.7317	2.9972	3.4308	0.5001		
embedding function							
element	F_0	F_1	q				
Al	−2.9403	0.5639	−1.3026				
Mn	−1.5862	1.3917	−5.3935				
Pd	−4.0016	0.9432	−5.7749				
cutoff radius $r_c = 7$ Å							

Table A.1: Potential parameters for the model III Al-Pd-Mn potential. Distances are given in Å, energies in eV. The cutoff radius applies to pair and transfer functions.

parameter	pair	transfer	embedding	dipole	quadrupole
1	49.9999	−0.2263	−4.9277	−0.4159	−0.5434
2	26.2375	4.6098	0.6031	3.7864	2.5759
3	30.8244	3.5936	−0.0006	6.3000	3.4353
4	4.2577	2.6775		2.5022	2.5721
5	3.6016				
6	0.5623				
h	3.1270	0.5000		1.4476	2.8413

Table A.2: Potential parameters for the pure Si clathrate potential. The analytic functions are given in Tab. 9.3. The order of the parameters is according to the definition on the *potfit* homepage. The cutoff radius is 6 Å.

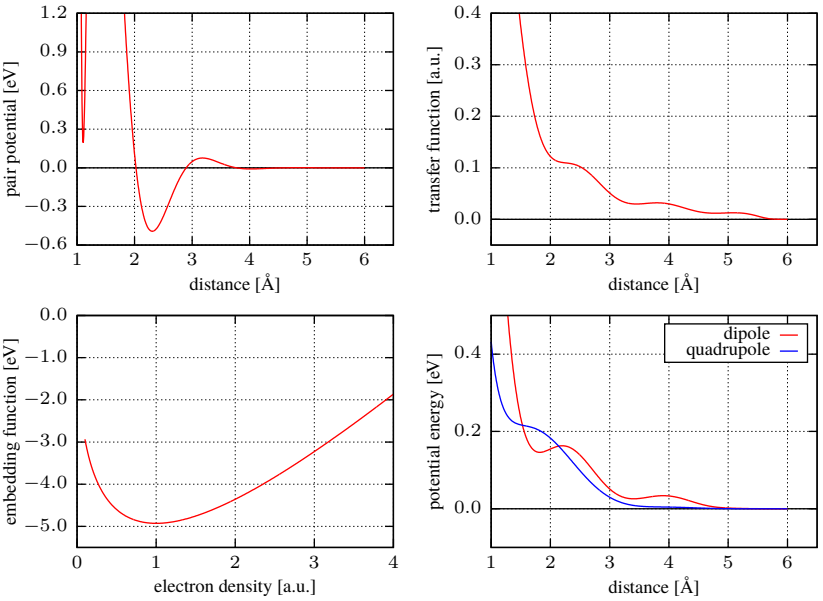

Figure A.2: Plots of the ADP potentials for the Si system.

parameter	1	2	3	4	5	6	h
			pair functions				
Si-Si (EOP)	237.4866	6.1670	−42.1463	3.3222	2.6923	0.0004	4.9656
Si-Ba (CSW)	0.5317	1.7338	3.2798	0.5059			1.8873
Ba-Ba (SOFT)	3.3030	5.9964					3.6363
			transfer functions				
Si (CSW)	−0.2598	1.8347	0.0029	2.1880			1.8773
Ba (CSW)	2.9958	2.2918	0.0121	3.0816			3.9903
			embedding functions				
Si (BJS)	−5.4478	0.8185	−0.0013				
Ba (BJS)	−8.3435	1.1280	−0.0002				
			dipole functions				
Si-Si (CSW)	0.2285	5.1987	1.6460	1.3649			3.8667
Si-Ba (CSW)	0.6366	2.1208	2.0742	0.5273			3.7506
Ba-Ba (SOFT)	0.1135	1.0687					0.5802
			quadrupole functions				
Si-Si (CSW)	−1.9853	1.1683	0.5146	2.0738			4.6129
Si-Ba (CSW)	2.9954	1.5176	0.8316	2.3552			4.1490
Ba-Ba (SOFT)	0.1114	1.1075					1.9262

Table A.3: Potential parameters for the Ba-Si clathrate potential. The analytic functions are given in Tab. 9.5. The order of the parameters is according to the definition on the *potfit* homepage. The cutoff radius is 6 Å.

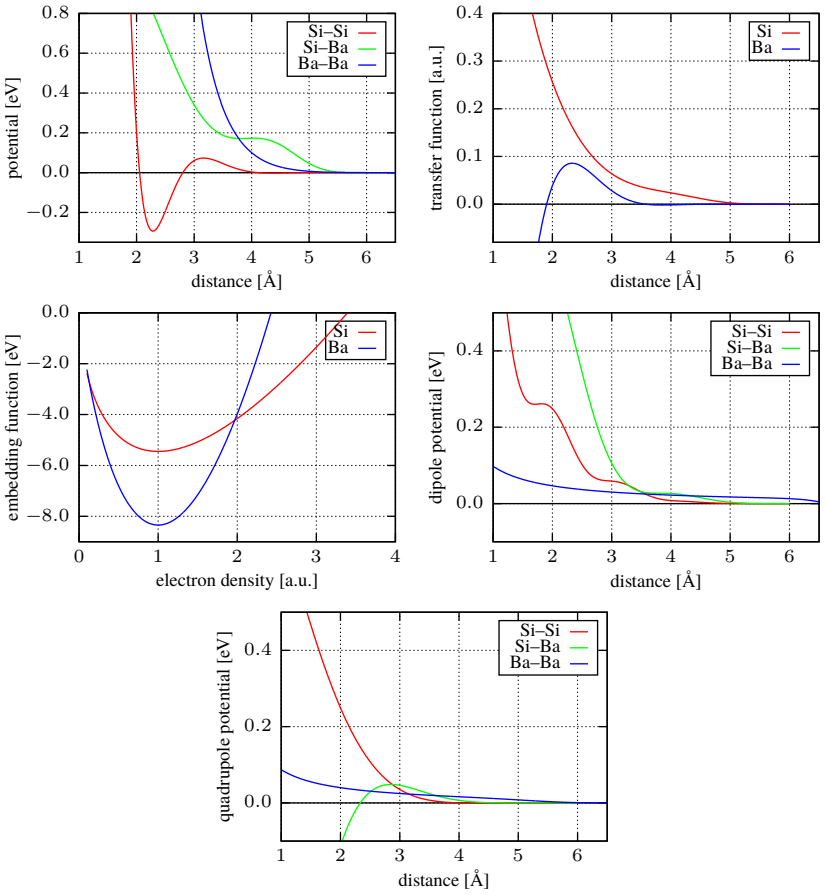

Figure A.3: Plots of the ADP potentials for the Ba-Si system.

parameter	pair	transfer	embedding	dipole	quadrupole
1	7002.5065	−0.1856	−4.3789	0.1600	0.6291
2	19.3280	3.7814	0.6291	7.7149	2.8188
3	−83.0881	−0.0000	−0.0009	6.2996	5.8143
4	5.9236	2.5475		2.4459	1.8578
5	3.7778				
6	2.9061				
h	1.5770	0.5475		1.1369	4.0082

Table A.4: Potential parameters for the pure Ge clathrate potential. The analytic functions are given in Tab. 9.3. The order of the parameters is according to the definition on the *potfit* homepage. The cutoff radius is 6 Å.

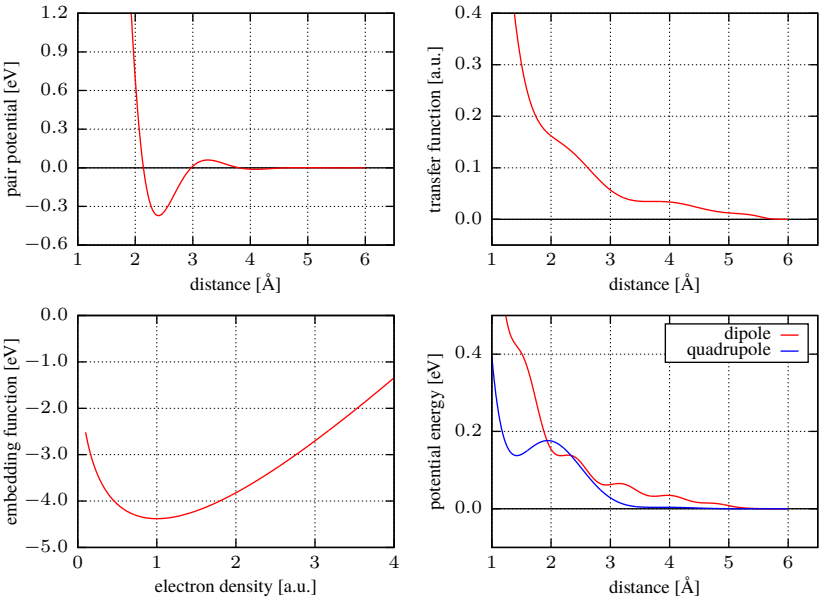

Figure A.4: Plots of the ADP potentials for the Ge system.

parameter	1	2	3	4	5	6	h
			pair functions				
Ge-Ge (EOP)	683.6298	35.6489	−247.0402	5.5586	2.1288	0.0004	4.3517
Ge-Ba (CSW)	2.9987	1.0028	4.6893	2.0759			0.2005
Ba-Ba (SOFT)	2.8566	1.0043					1.7825
			transfer functions				
Ge (CSW)	0.4024	2.2466	0.0946	2.3170			1.0673
Ba (CSW)	0.8254	1.6253	3.7465	0.5000			2.4624
			embedding functions				
Ge (BJS)	−4.7371	0.9999	0.0371				
Ba (BJS)	−3.5339	0.1077	−0.0052				
			dipole functions				
Ge-Ge (CSW)	2.7094	1.6312	2.7363	3.8997			1.2411
Ge-Ba (CSW)	2.9999	1.2136	4.5200	1.9481			2.4998
Ba-Ba (SOFT)	0.1456	1.0003					0.8608
			quadrupole functions				
Ge-Ge (CSW)	−0.5414	1.6707	0.0100	2.7157			1.9455
Ge-Ba (CSW)	1.9999	0.6149	2.3938	2.1111			3.7727
Ba-Ba (SOFT)	2.1458	4.9999					1.9986

Table A.5: Potential parameters for the Ba-Ge clathrate potential. The analytic functions are given in Tab. 9.5. The order of the parameters is according to the definition on the *potfit* homepage. The cutoff radius is 6 Å.

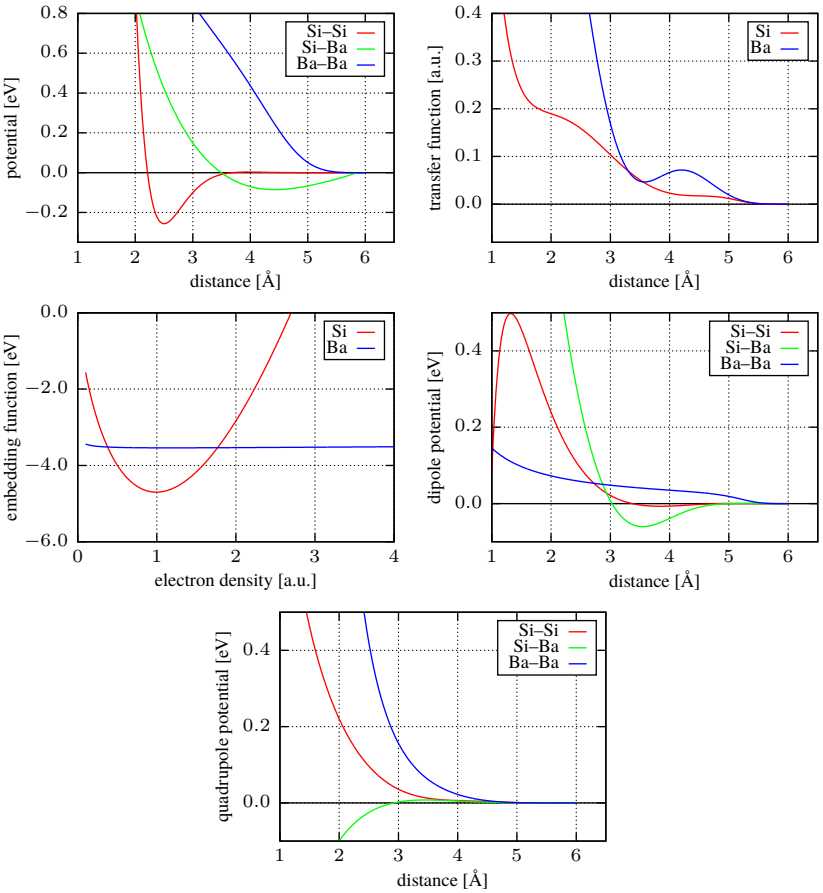

Figure A.5: Plots of the ADP potentials for the Ba-Ge system.

Bibliography

[1] Adams, G. B., O'Keeffe, M., Demkov, A. A., Sankey, O. F., and Huang, Y.-M.: Wide-band-gap Si in open fourfold-coordinated clathrate structures. *Physical Review B*, **49** (12), 8048 – 8053, 1994.

[2] Ali, M. and Gabere, M.: A simulated annealing driven multi-start algorithm for bound constrained global optimization. *Journal of Computational and Applied Mathematics*, **233**, 2661 – 2674, 2010.

[3] Allen, M. P. and Tildesley, D. J.: *Computer Simulation of Liquids*. Oxford University Press, 1989.

[4] Alleno, E., Maillet, G., Rouleau, O., Leroy, E., Godart, C., Carrillo-Cabrera, W., Simon, P., and Grin, Y.: Germanium Vacancies and Charge Transport Properties in $Ba_8Zn_xGe_{46-x-y}\square_y$. *Chemistry of Materials*, **21**, 1485 – 1493, 2009.

[5] Andersen, H. C.: Molecular dynamics simulations at constant pressure and/or temperature. *The Journal of Chemical Physics*, **72**, 2384 – 2393, 1980.

[6] Aydemir, U., Candolfi, C., Borrmann, H., Baitinger, M., Ormeci, A., Carrillo-Cabrera, W., Chubilleau, C., Lenoir, B., Dauscher, A., Oeschler, N., Steglich, F., and Grin, Y.: Crystal structure and transport properties of $Ba_8Ge_{43}\square_3$. *Dalton Transactions*, **39** (4), 1078 – 1088, 2010.

[7] Baker, J. F. C. and Hart, M.: An absolute measurement of the lattice parameter of germanium using multiple-beam X-ray diffractometry. *Acta Crystallographica Section A*, **31**, 364 – 367, 1975.

[8] Banerjea, A. and Smith, J. R.: Origins of the universal binding-energy relation. *Physical Review B*, **37**, 6632 – 6645, 1988.

[9] Barber, C. B., Dobkin, D. P., and Huhdanpaa, H.: The quickhull algorithm for convex hulls. *ACM Transactions on Mathematical Software*, **22**, 469–483, 1996.

[10] Baskes, M. I.: Application of the Embedded-Atom Method to Covalent Materials: A Semiempirical Potential for Silicon. *Physical Review Letters*, **59**, 2666–2669, 1987.

[11] Becke, A. D.: Density-functional exchange-energy approximation with correct asymptotic behavior. *Physical Review A*, **38** (6), 3098–3100, 1988.

[12] Beekman, M., Schnelle, W., Borrmann, H., Baitinger, M., Grin, Y., and Nolas, G. S.: Intrinsic Electrical and Thermal Properties from Single Crystals of $Na_{24}Si_{136}$. *Physical Review Letters*, **104** (1), 18301, 2010.

[13] Beraha, L.: *Modélisation des approximants de la phase icosahédrique Al-Pd-Mn et étude de leurs transformation structurales*. Ph.D. thesis, École Polytechnique, Paris, 1997.

[14] Bergman, G., Waugh, J. L. T., and Pauling, L.: The Crystal Structure of the Metallic Phase $Mg_{32}(Al,Zn)_{49}$. *Acta Crystallographica*, **10**, 254–259, 1957.

[15] Bernstein, N., Feldman, J. L., and Singh, D. J.: Calculations of dynamical properties of skutterudites: Thermal conductivity, thermal expansivity, and atomic mean-square displacement. *Physical Review B*, **81** (13), 134301, 2010.

[16] Bindi, L., Steinhardt, P. J., Yao, N., and Lu, P. J.: Natural Quasicrystals. *Science*, **324**, 1306–1309, 2009.

[17] Biswas, K., He, J., Blum, I. D., Wu, C.-I., Hogan, T. P., Seidman, D. N., Dravid, V. P., and Kanatzidis, M. G.: High-performance bulk thermoelectrics with all-scale hierarchical architectures. *Nature*, **489**, 414–418, 2012.

[18] Böhme, B., Aydemir, U., Ormeci, A., Schnelle, W., Baitinger, M., and Grin, Y.: Synthesis of the intermetallic clathrate $Na_2Ba_6Si_{46}$ by oxidation of Na_2BaSi_4 with HCl. *Science and Technology of Advanced Materials*, **8**, 410–415, 2007.

[19] Boudard, M., Klein, H., Boissieu, M. D., Audier, M., and Vincent, H.: Structure of quasicrystalline approximant phase in the Al-Pd-Mn system. *Philosophical Magazine A*, **74**, 939–956, 1996.

[20] Brest, J., Greiner, S., Boskovic, B., Mernik, M., and Zumer, V.: Self-Adapting Control Parameters in Differential Evolution: A Comparative Study on Numerical Benchmark Problems. *IEEE Transactions on Evolutionary Computation*, **10**, 646–657, 2006.

[21] Brommer, P.: *Entwicklung und Test von Wechselwirkungspotenzialen in Quasikristallen*. Master's thesis, Universität Stuttgart, 2003.
URL: http://elib.uni-stuttgart.de/opus/volltexte/2003/1570/

[22] Brommer, P.: *Development and test of interaction potentials for complex metallic alloys*. Ph.D. thesis, Universität Stuttgart, 2008.
URL: http://elib.uni-stuttgart.de/opus/volltexte/2008/3410/

[23] Car, R. and Parrinello, M.: Unified Approach for Molecular Dynamics and Density-Functional Theory. *Physical Review Letters*, **55** (22), 2471 – 2474, 1985.

[24] Chakraborty, U. (ed.): *Advances in Differential Evolution*. Springer, 2008.

[25] Chantasiriwan, S. and Milstein, F.: Higher-order elasticity of cubic metals in the embedded-atom method. *Physical Review B*, **53**, 14080 – 14088, 1996.

[26] Corana, A., Marchesi, M., Martini, C., and Ridella, S.: Minimizing Multimodal Functions of Continuous Variables with the "Simulated Annealing" Algorithm. *ACM Transactions on Mathematical Software*, **13**, 262 – 280, 1987.

[27] Cros, C., Pouchard, M., and Hagenmuller, P.: Sur une nouvelle famille de clathrates minéraux isotypes des hydrates de gaz et de liquides. Interprétation des résultats obtenus. *Journal of Solid State Chemistry*, **2**, 570 – 581, 1970.

[28] Davy, H.: On a Combination of Oxymuriatic Gas and Oxygene Gas. *Philosophical Transactions of the Royal Society of London*, **101**, 155 – 162, 1811.

[29] Daw, M. S.: Model of metallic cohesion: The embedded-atom method. *Physical Review B*, **39** (11), 7441 – 7452, 1989.

[30] Daw, M. S. and Baskes, M. I.: Semiempirical, Quantum Mechanical Calculation of Hydrogen Embrittlement in Metals. *Physical Review Letters*, **50**, 1285 – 1288, 1983.

[31] Ding, K. and Andersen, H. C.: Molecular-dynamics simulation of amorphous germanium. *Physical Review B*, **34** (10), 6987 – 6991, 1986.

[32] Dong, J., Sankey, O. F., and Myles, C. W.: Theoretical Study of the Lattice Thermal Conductivity in Ge Framework Semiconductors. *Physical Review Letters*, **86** (11), 2361 – 2364, 2001.

[33] Dove, M. T.: *Structure and Dynamics: An Atomic View of Materials*. Oxford University Press, 2003.

[34] Eiben, A., Hinterding, R., and Michalewicz, Z.: Parameter control in evolutionary algorithms. *IEEE Transactions on Evolutionary Computation*, **3**, 124 – 141, 1999.

[35] Engel, M. and Trebin, H.-R.: A unified projection formalism for the Al-Pd-Mn quasi-crystal Ξ-approximants and their metadislocations. *Philosophical Magazine*, **85**, 2227 – 2247, 2005.

[36] Engel, M.: *Dynamics and Defects of Complex Cystals and Quasicrystals: Perspectives from Simple Model Systems*. Ph.D. thesis, Universität Stuttgart, 2008.
URL: http://elib.uni-stuttgart.de/opus/volltexte/2008/3469/

[37] Ercolessi, F. and Adams, J. B.: Interatomic Potentials from First-Principles Calculations: The Force-Matching Method. *Europhysics Letters*, **26**, 583 – 588, 1994.

[38] Ercolessi, F., Parrinello, M., and Tosatti, E.: Simulation of gold in the glue model. *Philosophical Magazine A*, **58**, 213 – 226, 1988.

[39] Erkoç, S.: Empirical many-body potential energy functions used in computer simulations of condensed matter properties. *Physics Reports*, **278**, 79 – 105, 1997.

[40] Evans, D. and Morriss, G.: *Statistical Mechanics of Nonequilibrium Liquids*. Academic Press, 1990.

[41] Feynman, R. P.: Forces in Molecules. *Physical Review*, **56** (4), 340 – 343, 1939.

[42] Finnis, M. W. and Sinclair, J. E.: A simple empirical N-body potential for transition metals. *Philosophical Magazine A*, **50**, 45 – 55, 1984.

[43] Glassbrenner, C. J. and Slack, G. A.: Thermal Conductivity of Silicon and Germanium from 3°K to the Melting Point. *Physical Review*, **134** (4A), A1058 – A1069, 1964.

[44] Goldman, A. I. and Kelton, R. F.: Quasicrystals and crystalline approximants. *Reviews of Modern Physics*, **65** (1), 213 – 230, 1993.

[45] Green, M. S.: Markoff Random Processes and the Statistical Mechanics of Time-Dependent Phenomena. *The Journal of Chemical Physics*, **20**, 1281 – 1295, 1952.

[46] Green, M. S.: Markoff Random Processes and the Statistical Mechanics of Time-Dependent Phenomena. II. Irreversible Processes in Fluids. *The Journal of Chemical Physics*, **22**, 398 – 413, 1954.

[47] Guloy, A. M., Ramlau, R., Tang, Z., Schnelle, W., Baitinger, M., and Grin, Y.: A guest-free germanium clathrate. *Nature*, **443**, 320 – 323, 2006.

[48] Hafner, J.: Ab-initio simulations of materials using VASP: Density-functional theory and beyond. *Journal of Computational Chemistry*, **29**, 2044 – 2078, 2008.

[49] Hamann, D. R., Schlüter, M., and Chiang, C.: Norm-Conserving Pseudopotentials. *Physical Review Letters*, **43** (20), 1494 – 1497, 1979.

[50] Hellmann, H.: A New Approximation Method in the Problem of Many Electrons. *The Journal of Chemical Physics*, **3**, 61 – 61, 1935.

[51] Henley, C. L.: Cell geometry for cluster-based quasicrystal models. *Physical Review B*, **43**, 993, 1991.

[52] Herman, F., Van Dyke, J. P., and Ortenburger, I. B.: Improved Statistical Exchange Approximation for Inhomogeneous Many-Electron Systems. *Physical Review Letters*, **22** (16), 807 – 811, 1969.

[53] Herrmann, R. F., Tanigaki, K., Kuroshima, S., and Suematsu, H.: Superconductivity in silicon based barium-inclusion clathrates. *Chemical Physics Letters*, **283**, 29 – 32, 1998.

[54] Hohenberg, P. and Kohn, W.: Inhomogeneous Electron Gas. *Physical Review*, **136** (3B), B864 – B871, 1964.

[55] Johnson, R. A.: Analytic nearest-neighbor model for fcc metals. *Physical Review B*, **37**, 3924 – 3931, 1988.

[56] Johnson, R. A. and Oh, D. J.: Analytic embedded atom method model for bcc metals. *Journal of Materials Research*, **4**, 1195 – 1201, 1989.

[57] Karttunen, A. J., Fässler, T. F., Linnolahti, M., and Pakkanen, T. A.: Structural Principles of Semiconducting Group 14 Clathrate Frameworks. *Inorganic Chemistry*, **50**, 1733 – 1742, 2011.

[58] Kasper, J. S., Hagenmuller, P., Pouchard, M., and Cros, C.: Clathrate Structure of Silicon Na_8Si_{46} and Na_xSi_{136} $(x < 11)$. *Science*, **150**, 1713 – 1714, 1965.

[59] Kirkpatrick, S., Gelatt, C. D., and Vecci, M. P.: Optimization by Simulated Annealing. *Science*, **220**, 671 – 680, 1983.

[60] Klein, H., Feuerbacher, M., Schall, P., and Urban, K.: Novel Type of Dislocation in an Al-Pd-Mn Quasicrystal Approximant. *Physical Review Letters*, **82**, 3468 – 3471, 1999.

[61] Kleinke, H.: New bulk Materials for Thermoelectric Power Generation: Clathrates and Complex Antimonides. *Chemistry of Materials*, **22**, 604 – 611, 2010.

[62] Kohn, W. and Sham, L. J.: Self-Consistent Equations Including Exchange and Correlation Effects. *Physical Review*, **140**, A1133 – A1138, 1965.

[63] Kong, L. T.: Phonon dispersion measured directly from molecular dynamics simulations. *Computer Physics Communications*, **182**, 2201 – 2207, 2011.

[64] Kresse, G.: *Ab initio Molekulardynamik für flüssige Metalle*. Ph.D. thesis, Technische Universität Wien, 1993.

[65] Kresse, G. and Furthmüller, J.: Efficiency of ab-initio total energy calculations for metals and semiconductors using a plane-wave basis set. *Computational Materials Science*, **6**, 15 – 50, 1996.

[66] Kresse, G. and Furthmüller, J.: Efficient iterative schemes for *ab initio* total-energy calculations using a plane wave basis set. *Physical Review B*, **54**, 11169 – 11186, 1996.

[67] Kresse, G. and Hafner, J.: *Ab initio* molecular dynamics for liquid metals. *Physical Review B*, **47**, 558 – 561, 1993.

[68] Kubo, R.: Statistical-Mechanical Theory of Irreversible Processes. I. General Theory and Simple Applications to Magnetic and Conduction Problems. *Journal of the Physical Society of Japan*, **12**, 570 – 586, 1957.

[69] Kurganskii, S., Borshch, N., and Pereslavtseva, N.: Electronic structure and spectral properties of Si_{46} and Na_8Si_{46} clathrates. *Semiconductors*, **39** (10), 1176 – 1181, 2005.

[70] Lange, P.: Ein Vergleich zwischen Bi_2Te_3 und Bi_2Te_2S. *Naturwissenschaften*, **27** (8), 133 – 134, 1939.

[71] Lee, C., Yang, W., and Parr, R. G.: Development of the Colle-Salvetti correlation-energy formula into a functional of the electron density. *Physical Review B*, **37** (2), 785 – 789, 1988.

[72] Lee, Y. H., Biswas, R., Soukoulis, C. M., Wang, C. Z., Chan, C. T., and Ho, K. M.: Molecular-dynamics simulation of thermal conductivity in amorphous silicon. *Physical Review B*, **43** (8), 6573 – 6580, 1991.

[73] Lennard-Jones, J. E.: On the Determination of Molecular Fields. II. From the Equation of State of a Gas. *Proceedings of the Royal Society A*, **106**, 463 – 477, 1924.

[74] Lenosky, T. J., Sadigh, B., Alonso, E., Bulatov, V. V., Rubia, T. D. de la, Kim, J., Voter, A. F., and Kress, J. D.: Highly optimized empirical potential model of silicon. *Modelling and Simulation in Materials Science and Engineering*, **8**, 825, 2000.

[75] Levine, D. and Steinhardt, P. J.: Quasicrystals: A New Class of Ordered Structures. *Physical Review Letters*, **53** (26), 2477 – 2480, 1984.

[76] Mackay, A. L.: A dense non-crystallographic packing of equal spheres. *Acta Crystallographica*, **15**, 916 – 918, 1962.

[77] Martin, R. M.: *Electronic Structure: Basic Theory and Practical Methods*. Cambridge University Press, 2008.

[78] McGaughey, A. and Kaviany, M.: Thermal conductivity decomposition and analysis using molecular dynamics simulations: Part II. Complex silica structures. *International Journal of Heat and Mass Transfer*, **47**, 1799 – 1816, 2004.

[79] Mermin, N. D.: Thermal Properties of the Inhomogeneous Electron Gas. *Physical Review*, **137** (5A), A1441 – A1443, 1965.

[80] Michalski, J.: Thermal conductivity of amorphous solids above the plateau: Molecular-dynamics study. *Physical Review B*, **45** (13), 7054 – 7065, 1992.

[81] Mihalkovič, M., Henley, C. L., Widom, M., and Ganesh, P.: Empirical oscillating potentials for alloys from ab-initio fits, Feb. 2008. URL: arXiv:0802.2926v2 [cond-mat.mtrl-sci]

[82] Mishin, Y., Mehl, M., and Papaconstantopoulos, D.: Phase stability in the Fe – Ni system: Investigation by first-principles calculations and atomistic simulations. *Acta Materialia*, **53**, 4029 – 4041, 2005.

[83] Monkhorst, H. J. and Pack, J. D.: Special points for Brillouin-zone integrations. *Physical Review B*, **13**, 5188 – 5192, 1976.

[84] Morse, P. M.: Diatomic Molecules According to the Wave Mechanics. 2. Vibrational Levels. *Physical Review*, **34**, 57, 1929.

[85] Müller-Plathe, F.: A simple nonequilibrium molecular dynamics method for calculating the thermal conductivity. *The Journal of Chemical Physics*, **106**, 6082 – 6085, 1997.

[86] Nguyen, L. T. K., Aydemir, U., Baitinger, M., Bauer, E., Borrmann, H., Burkhardt, U., Custers, J., Haghighirad, A., Hofler, R., Luther, K. D., Ritter, F., Assmus, W., Grin, Y., and Paschen, S.: Atomic ordering and thermoelectric properties of the n-type clathrate $Ba_8Ni_{3.5}Ge_{42.1}\square_{0.4}$. *Dalton Transactions*, **39** (4), 1071 – 1077, 2010.

[87] Nolas, G. S., Cohn, J. L., Slack, G. A., and Schujman, S. B.: Semiconducting Ge clathrates: Promising candidates for thermoelectric applications. *Applied Physics Letters*, **73**, 178 – 180, 1998.

[88] Nolas, G. S., Sharp, J., and Goldsmid, H. J.: *Thermoelectrics: basic principles and new materials developments*. Springer, 2001.

[89] Nosé, S.: A unified formulation of the constant temperature molecular dynamics methods. *The Journal of Chemical Physics*, **81**, 511 – 519, 1984.

[90] Oh, D. J. and Johnson, R. A.: Simple embedded atom method model for fec and hcp metals. *Journal of Materials Research*, **3**, 471 – 478, 1988.

[91] Pauling, L.: The crystal structure of magnesium stannide. *Journal of the American Chemical Society*, **45**, 2777 – 2780, 1923.

[92] Pauling, L.: The Structure and Entropy of Ice and of Other Crystals with Some Randomness of Atomic Arrangement. *Journal of the American Chemical Society*, **57**, 2680 – 2684, 1935.

[93] Penrose, R.: The Rôle of Aesthetics in Pure and Applied Mathematical Research. *The Institute of Mathematics and its Applications Bulletin*, **10**, 266 – 271, 1974.

[94] Perdew, J. P., Burke, K., and Ernzerhof, M.: Generalized Gradient Approximation Made Simple. *Physical Review Letters*, **77** (18), 3865 – 3868, 1996.

[95] Perdew, J. P. and Wang, Y.: Accurate and simple analytic representation of the electron-gas correlation energy. *Physical Review B*, **45** (23), 13244 – 13249, 1992.

[96] Powell, M. J. D.: A method for minimizing a sum of squares of non-linear functions without calculating derivatives. *Computer Journal*, **7**, 303 – 307, 1965.

[97] Press, W. H., Teukolsky, S. A., Vetterling, W. T., and Flannery, B. P.: *Numerical Recipes in C: The Art of Scientific Computing*. Academic Press, Cambridge, 1992.

[98] Rahnamayan, S., Tizhoosh, H. R., and Salama, M. M. A.: Opposition-Based Differential Evolution. *In*: Chakraborty, U. (ed.): *Advances in Differential Evolution*. Springer, 2008.

[99] Robertson, I. J. and Payne, M. C.: k-point sampling and the k.p method in pseudopotential total energy calculations. *Journal of Physics: Condensed Matter*, **2**, 9837, 1990.

[100] Róg, T., Murzyn, K., Hinsen, K., and Kneller, G. R.: nMoldyn: A program package for a neutron scattering oriented analysis of molecular dynamics simulations. *Journal of Computational Chemistry*, **24**, 657 – 667, 2003.

[101] Rose, J. H., Smith, J. R., Guinea, F., and Ferrante, J.: Universal features of the equation of state of metals. *Physical Review B*, **29**, 2963 – 2969, 1984.

[102] Saito, M. and Matsumoto, M.: SIMD-Oriented Fast Mersenne Twister: a 128-bit Pseudorandom Number Generator. *In*: Keller, A., Heinrich, S., and Niederreiter, H. (eds.): *Monte Carlo and Quasi-Monte Carlo Methods 2006*. Springer Berlin Heidelberg, 2008.

[103] Sharma, H. R., Shimoda, M., and Tsai, A. P.: Quasicrystal surfaces: structure and growth of atomic overlayers. *Advances in Physics*, **56**, 403 – 464, 2007.

[104] Shechtman, D., Blech, I., Gratias, D., and Cahn, J. W.: Metallic Phase with Long-Range Orientational Order and No Translational Symmetry. *Physical Review Letters*, **53**, 1951 – 1953, 1984.

[105] Slack, G. A. and Rowe, D. M.: *CRC Handbook fo Thermoelectrics*. CRC Press, 1995.

[106] Stadler, J., Mikulla, R., and Trebin, H.-R.: IMD: a Software Package for Molecular Dynamics Studies on Parallel Computers. *International Journal of Modern Physics C*, **8**, 1131 – 1140, 1997.

[107] Stillinger, F. H. and Weber, T. A.: Computer simulation of local order in condensed phases of silicon. *Physical Review B*, **31**, 5262 – 5271, 1985.

[108] Storn, R. and Price, K.: Differential Evolution – A Simple and Efficient Heuristic for global Optimization over Continuous Spaces. *Journal of Global Optimization*, **11** (4), 341 – 359, 1997.

[109] Stott, M. J. and Zaremba, E.: Quasiatoms: An approach to atoms in nonuniform electronic systems. *Physical Review B*, **22**, 1564 – 1583, 1980.

[110] Tanigaki K., Shimizu T., Itoh K. M., Teraoka J., Moritomo Y., and Yamanaka S.: Mechanism of superconductivity in the polyhedral-network compound Ba_8Si_{46}. *Nature Materials*, **2**, 653 – 655, 2003.

[111] Tenenbaum, A., Ciccotti, G., and Gallico, R.: Stationary nonequilibrium states by molecular dynamics. Fourier's law. *Physical Review A*, **25** (5), 2778 – 2787, 1982.

[112] Tersoff, J.: New empirical model for the structural properties of silicon. *Physical Review Letters*, **56** (6), 632 – 635, 1986.

[113] Tersoff, J.: New empirical approach for the structure and energy of covalent systems. *Physical Review B*, **37** (12), 6991 – 7000, 1988.

[114] Tersoff, J.: Modeling solid-state chemistry: Interatomic potentials for multicomponent systems. *Physical Review B*, **39** (8), 5566 – 5568, 1989.

[115] Thijssen, J.: *Computational Physics*. Cambridge University Press, 2007.

[116] Togo, A., Oba, F., and Tanaka, I.: First-principles calculations of the ferroelastic transition between rutile-type and $CaCl_2$-type SiO_2 at high pressures. *Physical Review B*, **78** (13), 134106, 2008.

[117] Urban, K. and Feuerbacher, M.: Structurally complex alloy phases. *Journal of Non-Crystalline Solids*, **334 & 335**, 143 – 150, 2004.

[118] Venkatasubramanian, R., Siivola, E., Colpitts, T., and O'Quinn, B.: Thin-film thermoelectric devices with high room-temperature figures of merit. *Nature*, **413**, 597 – 602, 2001.

[119] Vitek, V.: Pair Potentials in Atomistic Computer Simulations. *MRS Bulletin*, **21**, 20 – 23, 1996.

[120] Weber, T., Dshemuchadse, J., Kobas, M., Conrad, M., Harbrecht, B., and Steurer, W.: Large, larger, largest – a family of cluster-based tantalum copper aluminides with giant unit cells. I. Structure solution and refinement. *Acta Crystallographica Section B*, **65**, 308 – 317, 2009.

[121] Widom, M. and Mihalkovič, M.: *Alloy database*.
URL: http://alloy.phys.cmu.edu

[122] Zhang, H., Borrmann, H., Oeschler, N., Candolfi, C., Schnelle, W., Schmidt, M., Burkhardt, U., Baitinger, M., Zhao, J.-T., and Grin, Y.: Atomic Interactions in the p-Type Clathrate I $Ba_8Au_{5.3}Ge_{40.7}$. *Inorganic Chemistry*, **50**, 1250 – 1257, 2011.

List of publications

[P1] Schopf, D.: *Effektive Potenziale für komplexe metallische Phasen*. Master's thesis, Universität Stuttgart, 2009.
URL: http://elib.uni-stuttgart.de/opus/volltexte/2009/4864/

[P2] Frigan, B., Santana, A., Engel, M., Schopf, D., Trebin, H.-R., and Mihalkovič, M.: Low-temperature structure of ξ'-Al-Pd-Mn optimized by ab initio methods. *Physical Review B*, **84** (18), 184203, 2011.

[P3] Schopf, D., Brommer, P., Frigan, B., and Trebin, H.-R.: Embedded atom method potentials for Al-Pd-Mn phases. *Physical Review B*, **85** (5), 54201, 2012.

[P4] Schopf, D., Brommer, P., Beck, P., and Trebin, H.-R.: Potfit technical paper. In preparation. 2013

Danksagung

An erster Stelle möchte ich mich ganz herzlich bei Herrn Prof. Dr. Hans-Rainer Trebin bedanken. Er hat mir während der vergangenen Jahre viel Freiheit bei der Durchführung dieser Arbeit gewährt und konnte mir bei Problemen immer mögliche Lösungswege aufzeigen. Durch seine menschliche und zuvorkommende Art war die Arbeitsatmosphäre am ITAP immer freundlich und sehr entspannt. Für die Möglichkeit, an verschiedenen Tagungen und Workshops teilzunehmen, bin ich ihm außerordentlich dankbar.

Herrn Prof. Dr. Christian Holm danke ich für die rasche Übernahme des Mitberichts.

Bei Dr. Johannes Roth bedanke ich mich für das mir entgegengebrachte Vertrauen bei der Rechnerverwaltung. Er war außerdem für jegliche Art von Fragen ein kompetenter und verlässlicher Ansprechpartner.

Ohne meinen langjährigen Zimmernachbarn Dr. Holger Euchner wäre ein Großteil dieser Arbeit nicht möglich gewesen. Er hatte stets ein offenes Ohr für sowohl berufliche als auch private Probleme jeglicher Art.

Dr. Philipp Beck hat mir in gemeinsamen Diskussionen viele kleine oder manchmal auch größere Denkanstöße geben können.

Benjamin Frigan hat mir vor allem bei den ε Phasen viele Fragen beantworten können. Für die dazugehörigen Bilder (Kapitel 8) bin ich ihm sehr dankbar.

Allen anderen Mitarbeitern des Instituts möchte ich ebenfalls für die freundliche Zusammenarbeit bei verschiedenen Projekten danken.

Das Sekretariat des ITAP möchte ich an dieser Stelle ebenfalls erwähnen. Ulrike Mergenthaler, Marietta Köstler und auch Simone Blümlein waren stets freundlich,

zuvorkommend und immer gut gelaunt. Bei allen organisatorischen und administrativen Tätigkeiten konnten sie mir unverzüglich weiterhelfen.

Bei meinen Freunden und Studienkollegen möchte ich mich für die vielfältige Unterstützung in guten wie in schlechten Zeiten bedanken. Auch meine Mitspieler im Handball, die für die oftmals nötige Ablenkung gesorgt haben, sollen nicht unerwähnt bleiben.

Abschließend möchte ich meiner Familie und ganz speziell meinen Eltern und Großeltern danken. Sie haben mir das Studium und die Promotion ermöglicht und mich dabei stets unterstützt. Für diese, nicht nur finanzielle, Unterstützung bin ich ihnen unendlich dankbar.

Hiermit versichere ich, die vorliegende Arbeit selbstständig verfasst und keine anderen als die angegebenen Quellen und Hilfsmittel benutzt sowie die Zitate deutlich kenntlich gemacht zu haben.

Stuttgart, im Februar 2013 *Daniel Schopf*